Metal-Substituted ZrB_2 and HfB_2 as Low-Cost and High-Performance Bifunctional Electrocatalysts for Water Splitting

by

Büşra Mete

A Dissertation Submitted to the
Graduate School of Sciences and Engineering
in Partial Fulfillment of the Requirements for
the Degree of

Master of Science

in

Materials Science and Engineering

August 5, 2021

Metal-Substituted ZrB_2 and HfB_2 as Low-Cost and High-Performance Bifunctional Electrocatalysts for Water Splitting

Koç University

Graduate School of Sciences and Engineering

This is to certify that I have examined this copy of a master's thesis by

Büşra Mete

and have found that it is complete and satisfactory in all respects,
and that any and all revisions required by the final
examining committee have been made.

Committee Members:

_____

Asst.Prof. Umut Aydemir (Advisor)

_____

Assoc. Prof. Uğur Önal

_____

Asst. Prof. Ferdi Karadaş

Date: 05.08.2021

To my beloved family…

ABSTRACT

Metal-Substituted ZrB_2 and HfB_2 as Low-Cost and High-Performance Bifunctional Electrocatalysts for Water Splitting

Büşra Mete

Master of Science in Materials Science and Engineering

August 5, 2021

Growing global energy demand, descending amount of fossil fuels, and severe climate changes have encouraged researchers to develop clean, sustainable, and efficient energy sources. Currently, hydrogen energy is one of the most promising solutions as the ideal energy carrier by virtue of the highest gravimetric energy density of any known fuel, zero carbon footprint, and earth abundance. In high purity hydrogen gas production, electrocatalytic water splitting has come to the fore; in this regard, earth-abundant, cost-efficient, corrosion-resistant, and bifunctional materials with remarkable electrocatalytic performances are needed. In this thesis, transition metal substituted ZrB_2 and HfB_2 families were investigated as promising electrocatalysts. They were synthesized by the carbothermal reduction method and employed as bifunctional catalyst in 1 M KOH alkaline medium for both hydrogen and oxygen evolution reactions (HER and OER, respectively). The family of ZrB_2-based catalysts was studied with a general formula of $Zr_{(1-x)}TM_xB_2$ (x = 0.05, 0.1, 0.2 and 0.3) (*TM* = Fe, Co, and Ni). In the case of OER, $Zr_{0.8}Ni_{0.2}B_2$ sample led to an onset potential of 1.58 V at 10 mA cm^{-2} current density, indicating a remarkable performance with a very low overpotential of 350 mV. Besides, $Zr_{0.8}Ni_{0.2}B_2$ displayed a value of 56.6 mV dec^{-1} regarding the Tafel slope, which was smaller than the commercial RuO_2 (66.2 mV dec^{-1}). In the case of HER, $Zr_{0.8}Co_{0.2}B_2$ with 420 mV overpotential and 101.6mV dec^{-1} showed the best performance. The family of HfB_2-based catalysts with a general formula of $Hf_{(1-x)}TM_xB_2$ (x = 0.1, 0.2 and 0.3) (*TM* = Co, and Ni) was also investigated. In parallel with the ZrB_2 case, Ni substitution enhanced the OER performance and $Hf_{0.8}Ni_{0.2}B_2$ sample leading to an onset potential of 1.55 V at 10 mA cm^{-2} current density with a very low overpotential of 320 mV and infinitesimal value of 39.5 mV dec^{-1} as Tafel slope. For HER, $Hf_{0.8}Co_{0.2}B_2$ with 430 mV overpotential and 105.4mV dec^{-1} showed the best performance. Both catalysts were examined for their long-term stability, resulting in excellent durability after 12 -20 h. As-prepared transition metal substituted diborides have great potential to be implemented in green energy applications.

ÖZETÇE

Genel Su Ayrıştırma Fonksiyonlu, Ucuz ve Yüksek Performanslı Metal Katkılanmış ZrB_2 ve HfB_2 Elektrokatalizörler

Büşra Mete

Malzeme Bilimleri ve Mühendisliği, Yüksek Lisans

5 Ağustos 2021

Artan küresel enerji talebi, azalan fosil yakıt miktarı ve şiddetli iklim değişiklikleri, araştırmacıları temiz, sürdürülebilir ve verimli enerji kaynakları geliştirmeye teşvik etmiştir. Günümüzde hidrojen enerjisi, bilinen herhangi bir yakıtın en yüksek gravimetrik enerji yoğunluğu, sıfır karbon ayak izi ve doğada bulunabilirliği sayesinde ideal enerji taşıyıcısı olarak en umut verici çözümlerden biridir. Yüksek saflıkta hidrojen gazı üretiminde elektrokatalitik su ayrıştırma ön plana çıkmış; bu bağlamda, dikkate değer elektrokatalitik performanslara sahip, toprakta bol, uygun maliyetli, korozyona dayanıklı ve iki işlevli malzemelere ihtiyaç oluşmuştur. Bu tez çalışmasında, geçiş metali katkılanmış ZrB_2 ve HfB_2 aileleri, karbotermal indirgeme yöntemi ile sentezlenmiş ve hem hidrojen hem de oksijen oluşum reaksiyonları (HER ve OER, sırasıyla) için 1 M KOH alkalin ortamında iki işlevli katalizör olarak kullanılmıştır. ZrB_2 bazlı katalizör malzeme seti hazırlanmış ve $Zr_{(1-x)}GM_xB_2$ (x = 0.05, 0.1, 0.2 ve 0.3) (GM = Fe, Co ve Ni) genel formülü ile performansları kaşılaştırmalı olarak incelenmiştir. OER performansında, $Zr_{0.8}Ni_{0.2}B_2$ numunesi, 10 mA cm^{-2} akım yoğunluğunda 1.58 V'luk bir başlangıç potansiyeline sahip olarak ve 350 mV'luk çok düşük bir aşırıpotansiyel ile dikkate değer bir performans göstermiştir. Ayrıca, $Zr_{0.8}Ni_{0.2}B_2$, ticari olarak kullanılan referans RuO_2'den (66.2 mV dec^{-1}) daha küçük Tafel eğimi (56.6 mV dec^{-1}) değeri göstermiştir. HER performansında, 420 mV aşırıpotansiyel ve 101.6mV dec^{-1} ile $Zr_{0.8}Co_{0.2}B_2$ en iyi performansı göstermiştir. $Hf_{(1-x)}GM_xB_2$ (x = 0.1, 0.2 ve 0.3) (GM = Co ve Ni) genel formülüne sahip HfB_2 bazlı katalizör ailesi de incelenmiştir. ZrB_2 çalışması ile paralel olarak, Ni katkılanması OER performansını arttırmıştır ve $Hf_{0.8}Ni_{0.2}B_2$ numunesi, 320 mV'luk bir aşırıpotansiyel ve 39.5 mV dec^{-1} çok düşük bir Tafel eğimi ile 10 mA cm^{-2} akım yoğunluğunda 1.55 V'luk bir başlangıç potansiyeline sahip olmuştur. HER için, 430 mV aşırı potansiyel ve 105.4mV dec^{-1} ile $Hf_{0.8}Co_{0.2}B_2$ en iyi performansı göstermiştir. Her iki katalizör malzemesi de uzun vadeli stabiliteleri açısından incelenmiştir, 12 -20 saat sonra mükemmel dayanıklılık göstermişlerdir. Bu çalışmada incelenen, sentezlenmiş katkısız ve geçiş metali katkılı diborürlerin, yeşil enerji uygulamalarında kullanılmak üzere büyük potansiyele sahip oldukları anlaşılmıştır.

ACKNOWLEDGMENTS

Foremost, I would like to express my sincere gratitude to my advisor Asst. Prof. Umut Aydemir for his unflagging support, encouragement, helpful advice and talks, always making me feel like a chemist. His careful and kind guidance helped me tremendously in improving my knowledge of chemistry during my MSc research. Even sometimes the conditions made it difficult, he always tried to provide lifetime opportunities for every member of our research group.

I would like to thank my thesis committee members, Assoc. Prof. Uğur Ünal for sharing his valuable experience with our catalysis group and helping us to move forward. I would also like to thank Asst. Prof. Ferdi Karadaş for taking time to consider this study. This work could be improved thanks to their valuable constructive feedback based on their expertise.

Being a part of such a research group and surrounded by all these kind, helpful and fun people made my years in Koç University unforgettable. A huge special thanks to our catalysis group members: Dr. Naeimeh Sadat Peighambardoust for helping me discover the exciting paths of the electrocatalysis world and carrying out all the analyses related to catalytic properties of materials, to Samet Aydın for helping me with the experiments and Ebrahim Sadeghi for helping me publishing my first paper. I would like to thank Prof. Dr. Mehmet Somer for sharing his endless knowledge of chemistry and guiding us. Many thanks to Dr. Özge Balcı, Dr. Semih Afyon, Kamil Kiraz, Dr. Sina Khoshsima, Şeyma Özdemir, İlayda Terzi, Kıvanç Sağlık, Ezgi Hatipoğlu and all the students that have spent precious time in the KUBAM family for the awesome working environment and discussions. I would like to thank members of KUYTAM, especially Dr. Barış Yağcı for SEM and XPS analyses.

As my closest friends, I would like to give a special acknowledgement to some group members for their endless support and belief in me through my journey. I will always remember the wonderful times we had and the memories we made. Countless thanks to Müjde Yahyaoğlu and Melis Özen for being like sisters to me, sharing everything together, our fun trips and replying all of my questions with patience in the lab. Many

thanks to Dr.Ferit Siyahcan and Samet Aydın for being always there for me when I needed a brother which I never had before. We have shared such remarkable memories together with laughs and tears but 99% of the time was spent laughing, honestly. I thank to Yaprak Subaşı for her sincere friendship, endless help, struggling with me at lectures and great food that we shared together.

My thanks and gratitude are never enough for a very special person, who I count as a part of my family, Mustafa Sevdaroğlu, for his countless advises and unlimited support. He was always with me through my journey as my best friend. When I had a complication, he consoled me and gave me all energy that I need to overcome. I cannot express my appreciation to his contribution and inspiration to my academic and personal life. Finally, I would like to thank beloved parents, my father Halim Mete for being such an understanding and supportive father. In the bottom of my heart, I can feel his appreciation and faith in me without hesitation in every step that I take. And, limitless thanks to the most valuable person in my life, my lovely mother Serpil Mete, literally for everything. I consider myself as the luckiest person to have such caring mother. Thanks for all the sacrifices you made, for always finding the solutions, for the time that was only two of us, for being such a strong role-model woman and for being my mom, sister, best friend from the first day of my life.

I want to thank the Turkish Academy of Sciences (TÜBA) - Outstanding Young Scientist Award Program (GEBİP) for financial support.

TABLE OF CONTENTS

List of Tables x

List of Figures xi

Abbreviations xv

Chapter 1: Introduction 1

Chapter 2: Literature Review On The Electrocatalytic Water Splitting 3

2.1 Electrocatalytic Water Splitting Systems 3

2.2 Evaluation Parameters for EWS Half Reactions 6

2.2.1 Overpotential (η) 6

2.2.2 Tafel Plot (Tafel Slope and Exchange Current Density) 7

2.3 Fundamentals of HER 8

2.4 Fundamentals of OER 10

2.5 TMB Electrocatalysts in the Literature 12

2.6 Further Adjustments of Properties 17

2.7 The Challenges of TMBs in EWS 21

Chapter 3: Material Characterization Techniques 23

3.1 X-Ray Diffraction (XRD) 23

3.2 Scanning Electron Microscopy (SEM) 23

3.3 Transmission Electron Microscopy (TEM) 24

3.4 X-Ray Photoelectron Spectroscopy (XPS) 24

3.5 Brunauer-Emmet-Teller (BET) Analyzer 25

Chapter 4: Results and Discussion 26

4.1 Synthesis Method of Electrocatalysts 26

4.2 Electrochemical Measurement Method 32

4.3 Characterization of ZrB_2 and TM-substituted ZrB_2 (TM=Fe, Co, Ni) 33
4.3.1 Chemical Characterization Results 33
4.3.2 Hydrogen Evolution Activities of ZrB_2 Samples 43
4.3.3 Oxygen Evolution Activities of ZrB_2 Samples 50
4.3.4 The Substitution Effect of Ni and Co 53
4.4 Characterization of HfB_2 and TM-Substituted HfB_2 (TM= Co, Ni) 55
4.4.1 Chemical Characterization Results 55
4.4.2 Hydrogen Evolution Activities of HfB_2 Samples 60
4.4.3 Oxygen Evolution Activities of HfB_2 Samples 63
Chapter 5: CONCLUSION 68
Bibliography 70
Appendix A: 77

LIST OF TABLES

Table 4.1 Summary of electrochemical parameters for all as-prepared samples ... 55

LIST OF FIGURES

Figure 2.1 Simplification of the system by employing bifunctional electrocatalysts [15] 4

Figure 2.2 Possible reaction pathways in alkaline and acidic electrolytes [2]..... 5

Figure 2.3 Schematic representation of pathways for HER on the cathode [6]..... 9

Figure 2.4 a) 12 transition elements that are used for synthesis of MB_2. A schematic of crystal structures of b) AlB_2 type c) ReB_2 type and d) RuB_2 type diborides with color codes [16]..... 13

Figure 2.5 a) Linear correlation between absolute value of hydrogen adsorption free energy and d-band center of diborides in comparison to Pt and Ru. b) Boron effect on the d-band center of metal. **c)** Adsorption sites for hydrogen on the RuB_2 (001) surface [16] 14

Figure 2.6 a) Experimental overpotentials at current density of 10 $mA.cm^{-2}$ in acidic electrolyte (left) and alkaline electrolyte (right). Linear correlation of d-band center and overpotentials at 0.1 $mA.cm^{-2}$ current density b) in acidic solution and **c)** in alkaline solution [16]..... 15

Figure 2.7 a) Overpotentials required to reach 10 $mA.cm^{-2}$ of layered diborides for HER b) Obtained Tafel slopes (mV/dec) of the metal diborides [3]..... 16

Figure 2.8 OER/HER activity of diverse catalysts in acid/base electrolyte [4]..... 22

Figure 4.1 Schematic representation of synthesis pathway by using graphite crucible. 28

Figure 4.2 A schematic representation of synthesis of transition metal diborides with alumina crucible..... 29

Figure 4.3 XRD data of pure ZrB_2 samples synthesized by alumina crucible. 30

Figure 4.4 XRD data of pure ZrB_2 samples synthesized by graphite crucible. 31

Figure 4.5 XRD patterns of $Zr_{(1-x)}Fe_xB_2$ (x= 0.025,0.05,0.075,0.1 and 0.2) samples with unsubstituted ZrB_2 (BM-16-9b)..... 34

Figure 4.6 XRD patterns of $Zr_{(1-x)}Ni_xB_2$ (x= 00.05,0.1 and 0.2) samples. 35

Figure 4.7 XRD patterns of $Zr_{(1-x)}Co_xB_2$ (x= 0.025,0.05,0.075,0.1 and 0.2) samples.... 35

Figure 4.8 Characterization of ZrB_2. Low magnification SEM, along with related EDS elemental mapping on the right side. Voids in SEM image can be detected as dark spots in EDS mapping. 36
Figure 4.9 Characterization of ZrB_2. a) High magnification SEM, b) TEM, along with related EDS elemental mapping on the right side. 36
Figure 4.10 SEM images of a) $Zr_{0.95}Fe_{0.05}B_2$, b) $Zr_{0.9}Fe_{0.1}B_2$, c) $Zr_{0.8}Fe_{0.2}B_2$, d) $Zr_{0.95}Co_{0.05}B_2$, e) $Zr_{0.9}Co_{0.1}B_2$, f) $Zr_{0.8}Co_{0.2}B_2$, g) $Zr_{0.95}Ni_{0.05}B_2$, h) $Zr_{0.9}Ni_{0.1}B_2$, and l) $Zr_{0.8}Ni_{0.2}B_2$; showing agglomeration reduction by increasing substitution concentration. 37
Figure 4.11 High magnification SEM image of $Zr_{0.8}Fe_{0.2}B_2$ along with EDS elemental mapping on the right side. 38
Figure 4.12 Characterization of metal-substituted ZrB_2. a) High magnification SEM image of $Zr_{0.8}Co_{0.2}B_2$, b) TEM of $Zr_{0.8}Co_{0.2}B_2$ (inset: SAED pattern), c) High magnification SEM image of $Zr_{0.8}Ni_{0.2}B_2$, and d) TEM of $Zr_{0.8}Ni_{0.2}B_2$, along with related EDS elemental mapping on the right side. 39
Figure 4.13 Characterization of metal-substituted ZrB_2. a) Low magnification SEM image of $Zr_{0.8}Co_{0.2}B_2$, b) Low magnification SEM image of $Zr_{0.8}Ni_{0.2}B_2$, and c) Low magnification SEM image of $Zr_{0.8}Fe_{0.2}B_2$, along with related EDS elemental mapping on the right side. 39
Figure 4.14 XPS spectra of a) $Zr_{0.8}Co_{0.2}B_2$, b) $Zr_{0.8}Ni_{0.2}B_2$ and c) $Zr_{0.8}Fe_{0.2}B_2$ 40
Figure 4.15 Zr 3d and dopant 2p XPS spectra for the a) Co-substituted ZrB_2, b) Ni-substituted ZrB_2, and c) Fe-substituted ZrB_2 and unsubstituted ZrB_2. 42
Figure 4.16 SEM images of the working electrode surface 43
Figure 4.17 Electrochemical performance of unsubstituted and substituted ZrB_2 towards HER recorded at a scan rate of 5 mV s^{-1} in 1 M KOH. a) Polarization curves, b) Related Tafel plots, c) Polarization curves of $Zr_{0.8}Co_{0.2}B_2$ initially and after 1000 CV scans at 100 mV s^{-1} and d) Chronopotentiometric curve of $Zr_{0.8}Co_{0.2}B_2$ recorded at a current density of 10 mA cm^{-2}. 44
Figure 4.18 a, c, and e) Cyclic voltammograms of ZrB_2, $Zr_{0.8}Ni_{0.2}B_2$, and $Zr_{0.8}Co_{0.2}B_2$, respectively along with their b, d, and f) Respective capacitive current at 0.85 V as a function of the scan rate. 46
Figure 4.19 Electrochemical performance of substituted ZrB_2 towards HER recorded at a scan rate of 5 mV s^{-1} in 1 M KOH. a) Polarization curves, b) Related Tafel plots, and

electrochemical performance of substituted ZrB_2 towards OER recorded at a scan rate of 5 mV s^{-1} in 1 M KOH, c) Polarization curves, d) Related Tafel plots. 48
Figure 4.20 a and b) Cyclic voltammograms of $Zr_{0.95}Ni_{0.05}B_2$ and $Zr_{0.9}Ni_{0.1}B_2$, respectively along with their c and d) Respective capacitive current at 0.85 V as a function of the scan rate. 48
Figure 4.21 a, c, and e) Cyclic voltammograms of $Zr_{0.95}Fe_{0.05}B_2$, $Zr_{0.9}Fe_{0.1}B_2$, and $Zr_{0.8}Fe_{0.2}B_2$, respectively along with their b, d, and f) Respective capacitive current at 0.85 V as a function of the scan rate. 49
Figure 4.22 a and b) Cyclic voltammograms of $Zr_{0.95}Co_{0.05}B_2$ and $Zr_{0.9}Co_{0.1}B_2$, respectively along with their c and d) Respective capacitive current at 0.85 V as a function of the scan rate. 50
Figure 4.23 Electrochemical performance of unsubstituted and substituted ZrB_2 towards OER recorded at a scan rate of 5 mV s^{-1} in 1 M KOH. a) Polarization curves, b) Related Tafel plots, c) Polarization curves of $Zr_{0.8}Ni_{0.2}B_2$ initially and after 1000 CV scans at 100 mV s^{-1} and d) Chronopotentiometric curve of $Zr_{0.8}Ni_{0.2}B_2$ recorded at a current density of 10 mA cm^{-2}. 51
Figure 4.24 Niquist plots of a) ZrB_2 and $Zr_{0.8}TM_{0.2}B_2$ (*TM* = Fe, Co, and Ni), b) $Zr_{1-x}TM_xB_2$ (*TM* = Fe, Co, and Ni , *x* = 0.05, 0.1, and 0.2) 52
Figure 4.25 XRD patterns of HfB_2 and $Hf_{0.8}TM_{0.2}B_2$ (*TM*= Co and Ni) 56
Figure 4.26 XRD patterns of unsubstituted HfB_2 with theoretical pattern and a) $Hf_{(1-x)}Co_xB_2$ b) $Hf_{(1-x)}Ni_xB_2$ (*x*= 0.1,0.2 and 0.3)..... 56
Figure 4.27 SEM images of a) unsubstituted-HfB_2 b) $Hf_{0.8}Ni_{0.2}B_2$ c) $Hf_{0.8}Co_{0.2}B_2$ 57
Figure 4.28 High magnification SEM image of unsubstituted HfB_2 along with EDS elemental mapping on the right side 57
Figure 4.29 Characterization of metal-substituted HfB_2. a) High magnification SEM image of $Hf_{0.8}Ni_{0.2}B_2$ b) TEM of $Hf_{0.8}Ni_{0.2}B_2$, along with related EDS mapping on the right side c) High magnification SEM image of $Hf_{0.8}Co_{0.2}B_2$ d) TEM of $Hf_{0.8}Co_{0.2}B_2$, along with related EDS mapping on the right side. 58
Figure 4.30 Characterization of metal-substituted HfB_2. High magnification SEM images of a) $Hf_{0.9}Ni_{0.1}B_2$ b) $Hf_{0.7}Ni_{0.3}B_2$ c) $Hf_{0.9}Co_{0.1}B_2$ c) $Hf_{0.7}Co_{0.3}B_2$ along with related EDS mapping on the right side..... 58
Figure 4.31 XPS spectra of a) unsunstitued-HfB_2 b) $Hf_{0.8}Ni_{0.2}B_2$ and c) $Hf_{0.8}Co_{0.2}B_2$ .. 59
Figure 4.32 Electrochemical performance of unsubstituted and substituted HfB_2 towards HER recorded at a scan rate of 5 mV s^{-1} in 1 M KOH. a) Polarization curves, b) Related

Tafel plots, c) Chronopotentiometric curve of $Hf_{0.8}Co_{0.2}B_2$ recorded at a current density of 10 mA cm^{-2}, and d) Polarization curves of $Hf_{0.8}Co_{0.2}B_2$ initially and after 20 h OER stability..... 61

Figure 4.33 a, c, and e) Cyclic voltammograms of HfB_2, $Hf_{0.8}Ni_{0.2}B_2$, and $Hf_{0.8}Co_{0.2}B_2$, respectively along with their b, d, and f) Respective capacitive current at 0.85 V as a function of the scan rate..... 62

Figure 4.34 Electrochemical performance of unsubstituted and substituted HfB_2 towards OER recorded at a scan rate of 5 mV s^{-1} in 1 M KOH. a) Polarization curves, b) Related Tafel plots, c) Chronopotentiometric curve of $Hf_{0.8}Ni_{0.2}B_2$ recorded at a current density of 10 mA cm^{-2}, and d) Polarization curves of $Hf_{0.8}Ni_{0.2}B_2$ initially and after 20 h OER stability..... 64

Figure 4.35 Electrochemical performance of substituted HfB_2 towards OER recorded at a scan rate of 5 mV s^{-1} in 1 M KOH, a) Polarization curves, b) Related Tafel plots, and electrochemical performance of substituted HfB_2 towards HER recorded at a scan rate of 5 mV s^{-1} in 1 M KOH. a) Polarization curves, b) Related Tafel plots. 65

Figure 4.36 a, c, e) and g) Cyclic voltammograms of $Hf_{0.9}Ni_{0.1}B_2$, $Hf_{0.7}Ni_{0.3}B_2$, $Hf_{0.9}Co_{0.1}B_2$, and $Hf_{0.7}Co_{0.3}B_2$ respectively along with their b, d, f and h) Respective capacitive current at 0.85 V as a function of the scan rate. 66

Figure 4.37 Niquist plots of a) $Hf_{(1-x)}TM_xB_2$ (*TM* = Co, and Ni) (*x*= 0.1 and 0.3), on the left side b) HfB_2 and $Hf_{0.8}TM_{0.2}B_2$ (*TM* = Co, and Ni) on the right-hand side..... 67

ABBREVIATIONS

EWS	Electrocatalytic Water Splitting
HER	Hydrogen Evolution Reaction
OER	Oxygen Evolution Reaction
AWE	Alkaline Water Electrolysis
RHE	Reversible Hydrogen Electrode
NHE	Normal Hydrogen Electrode
XRD	X-Ray Diffraction
SEM	Scanning Electron Microscopy
TEM	Transmission Electron Microscopy
XPS	X-Ray Photoelectron Spectroscopy
SAED	Selected Area Electron Diffraction
TMB	Transition Metal Boride
EIS	Electrochemical Impedance Spectroscopy
OCP	Open Circuit Potential
CV	Cyclic Voltammetry
SPS	Spark Plasma Sintering
SSA	Specific Surface Area
ECSA	Electrochemical Active Surface Area

Chapter 1:
INTRODUCTION

Exponentially increasing global energy demand, descending amount of fossil fuels and climate change have encouraged researchers to develop eco-friendly and efficient energy sources. Currently, hydrogen energy is one of the most promising source as the ideal energy carrier by virtue of highest gravimetric energy density of any known fuel [1], zero carbon footprint and earth abundance [2]. Hydrogen generation through electrochemical water splitting offers a sustainable and fossil-free solution for high quality hydrogen production. For the two half reactions of electrocatalytic water splitting, compounds based on precious metals (e.g., Pt/C) for HER (hydrogen evolution reaction) and their oxides (e.g., RuO_2) for OER (oxygen evolution reaction) are used as reference materials[3]. Due to high cost of precious metals, low abundance on earth and low tolerance to passivation; their large-scale production and commercialization are severely limited [2], [4], [5].

Up till today, most of the studied bifunctional electrocatalysts could not be able to perform supreme activities for both half reactions comparing to noble metals, since slow charge transfer rate and poor mechanical/chemical stability. Employing bifunctional electrocatalysts will simplify the EWS (electrocatalytic water splitting) system and accelerate commercialism for water splitting [4]. As being reference materials, noble metals are mostly efficient and stable at acidic conditions. In the alkaline systems, these electrocatalysts have high dissolution rate thus, transition metal-based materials replaced them accompanied by their low cost, high chemical stability and abundance [3], [6]. TMBs (transition metal borides), come forward as cost-friendly alternative to precious metals thanks to some unique properties for water splitting applications in comparison with the other TM-based counterparts. TMBs with 3D metallic framework with 2D borophene subunits have attracted attention for electrocatalytic applications. Diborides due to the layered structure formation, exhibit unique properties such as hardness, low electrical resistivity, high thermal conductivity and chemical stability [7]. Even though their well-defined crystal structures are highly studied, the electrocatalytic activity of most of the metal borides are remain unreported. Diborides show more abundant catalytic sites and better conductivity than other types of electrocatalysts (e.g. metal disulfides) [8].

The reverse electron transfer in TMBs (from boron to metal) provides electron rich metal sites and increases activity [9]. Modified electronic structure of TMBs, naturally decreases the kinetic barrier. Secondly, TMBs usually possess amorphous structure with chemical stability and high concentration of unsaturated sites which directly affect the catalytic performance [10]. Additionally, with surface oxidation of TMBs, boron oxide, borates, TM oxides and TM (oxy) hydroxides formation enhances OER performance [2]. Besides their unique properties for electrocatalytic applications, by applying various of strategies studied in the literature, the activity of TMBs can be altered more. These strategies in general primarily aims to increase the exposure on the surface-active areas of the materials. Especially for the OER half reaction, there are only limited number of articles can be found in the literature regardless of the pH of the electrolyte solution. Lack of reports about the performance of metal diborides for EWS can be attributed to harsh synthesis conditions and insufficient knowledge on the design principles.

For the first time, this study will investigate the effect of transition metal substitution into ZrB_2 and HfB_2 electrocatalyst materials in comparison with the unsubstituted transition metal diborides in terms of both HER and OER performances. There are only a few articles on the literature reporting the EWS activity of pure ZrB_2 and HfB_2 [2], [3], [11] proving that these electrocatalysts are promising candidates. To obtain a better performance for further efficiency on EWS systems, tailoring the properties with a series of strategies such as phase engineering, morphological engineering, doping and surface oxidation etc. will be investigated. In the second chapter, a comprehensive review on the literature about EWS theory, the mechanism of hydrogen and oxygen evolution reactions, important parameters to evaluate electrocatalytic activity and TMB electrocatalysts will be discussed. In the third chapter, the main characterization methods and the measuring techniques of the equipment will be given briefly. The experimental methods, synthesis techniques, chemical characterization results with different methods and electrochemical activity results of the samples will be discussed in detail in the fourth chapter. Lastly, conclusion section will summarize all research output for this study.

Chapter 2:

LITERATURE REVIEW ON THE ELECTROCATALYTIC WATER SPLITTING

2.1 Electrocatalytic Water Splitting Systems

Regarding the current eco-friendly energy source search of the world, hydrogen energy is one of the most promising sources as the ideal energy carrier. Hydrogen fundamentally exists in water and hydrocarbons on the planet Earth. Production of hydrogen gas in the industry, mostly relies upon catalytic steam forming, prompting the huge emission of CO_2 alongside extreme energy consumption [12]. In the current situation, other commercial production pathways of low-purity hydrogen gas are partial oxidation, coal gasification and pyrolysis, which promote the global carbon dioxide emissions [13]. Only about 4% of the total hydrogen is commercially produced by water splitting, although it has been studied for 230 years [14]. High purity (> 99.6%) hydrogen gas is produced as a by-product of chlorine and caustic soda in chlor-alkali industry [5]. By taking into account the urgent need of sustainable and fossil-free energy sources in present circumstances, high quality hydrogen gas production plays a vital role. Renewable energy can be stored by hydrogen in the chemical bond form, by using fuel cells or other appliances this stored energy can be converted back into electricity and thus, it can be transported to end-users [1].

The electrocatalytic water splitting system simply consists of two half reactions: hydrogen evolution reaction (HER) for water reduction at the cathode side and oxygen evolution reaction (OER) for water oxidation at the anode side of the cell (see Fig.2.1.) with an electrolyte solution as medium. Electrocatalysts are coated on the electrode surface with the intention of enhancing the overall splitting reaction efficiently and resulting in better energy conversion.

At 25 ˚C and 1 atm, regardless of the electrolyte pH, required energy input is ΔG= 237.1 kJ/mol [15] (corresponds to 1.23 V potential) to conduct water splitting; nevertheless, because of poor kinetics of both half reactions, higher overpotentials are encountered in general. By virtue of higher potential requirement for water splitting reaction, plenty of electrocatalyst materials have been explored comprehensively.

Bifunctional catalysts can demonstrate high activity for both OER and HER mechanisms. Thus far, bifunctional electrocatalysts could not be able to show supreme activities for both half-reactions comparing to noble metals, since slow charge transfer rate and poor stability. Employing bifunctional electrocatalysts will simplify the EWS system and accelerate commercialism for alkaline water splitting. With this materials, there will be no need to produce different electrocatalysts and use different equipment (see Fig. 2.1) for OER and HER and thus, fabrication cost will be decreased dramatically [4].

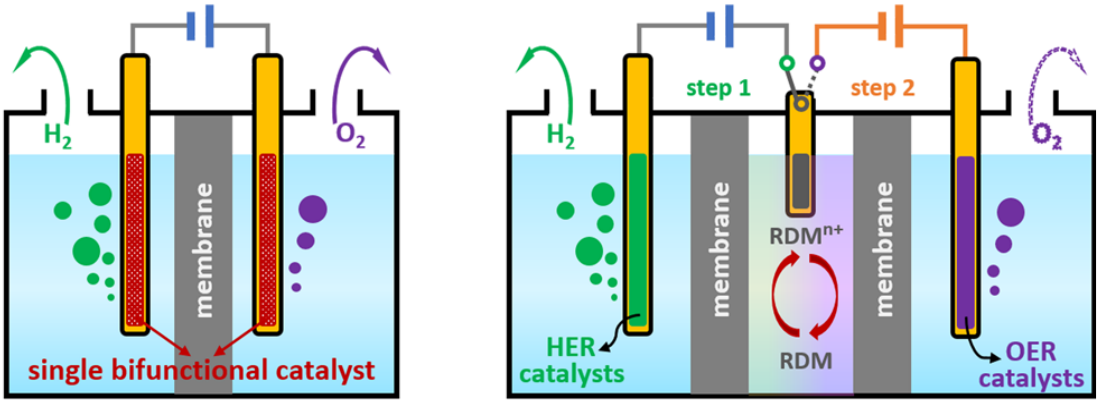

Figure 2.1 Simplification of the system by employing bifunctional electrocatalysts [15]

Noble metal electrocatalysts such as Pt-based materials for HER and Ir- and Ru-oxides for OER showed greatest activity in EWS system by means of highest exchange current density and lowest overpotential [3] in wide pH range. Unfortunately, due to high cost of precious metals, low abundance on earth and low tolerance to passivation; their large-scale production and commercialization are severely limited [2], [4], [5]. Even so, many studies dedicated to improve the catalytic activity of platinum such as chemical treatments, surface modifications, doping and completely supersede noble metals by employing sulfides, carbides, nitrides and borides [16]. Discovering the activity of electrocatalyst that can function equally through different pH range would be a big leap for EWS systems. Microbial electrolyzers works under neutral pH while PEM electrolyzers (polymer electrolyte membrane) operate under extreme acidic environment. Most of these electolyzers can operate with clean water, however, not even 1% of Earth's water sources are clean water. Desired electrolyzer should function under unclean water which can be considered as sea water that directly taken from natural sources such as oceans or rain. Targeted electrocatalyst materials can operate efficiently under mild acidic conditions (4.2-6 pH range) relevant to rain and mild alkaline conditions (8.1-9. pH range)

as sea water [9]. Many nonprecious metal electrocatalysts exhibits pH-dependent stabilities and activities because of different HER kinetics and possible electrochemical dissolution in severe pH conditions. As being reference materials, noble metals are mostly efficient and stable at acidic conditions. In the alkaline systems, these electrocatalysts have high dissolution rate thus, transition metal based materials replaced them accompanied by their low cost, high chemical stability and abundance [3], [6].

Alkaline water electrolysis (AWE) has been industrialized at 1920 [17] and thanks to easy operation, durability and non-precious metal compatibility, they are suitable to fulfil ultimate hydrogen energy demand of world. Industrial alkaline water electrolysis uses 6-10 M KOH solution at the 60-80 ˚C [5]. Nonetheless, high ohmic losses, low current densities (0.2-0.4 $A.cm^{-2}$) scale down the size of the stack system and enhance the overall cost for hydrogen production [18]. Acidic electrolyzers such as PEM operates higher current density (up to 2 $A.cm^{-2}$) yet requires noble metal based electrocatalysts towards severe acidic pH conditions. Neutral conditions, since the most abundant water source sea water can be employed, ensure better stability owing to absence of harsh corrosive media. However, the electrocatalysts suffer from ion poisoning. Usually, as electrolyte solutions, 1 M KOH, 1 M PBS and 0.5 M H_2SO_4 are used as alkaline, neutral and acidic media [5].

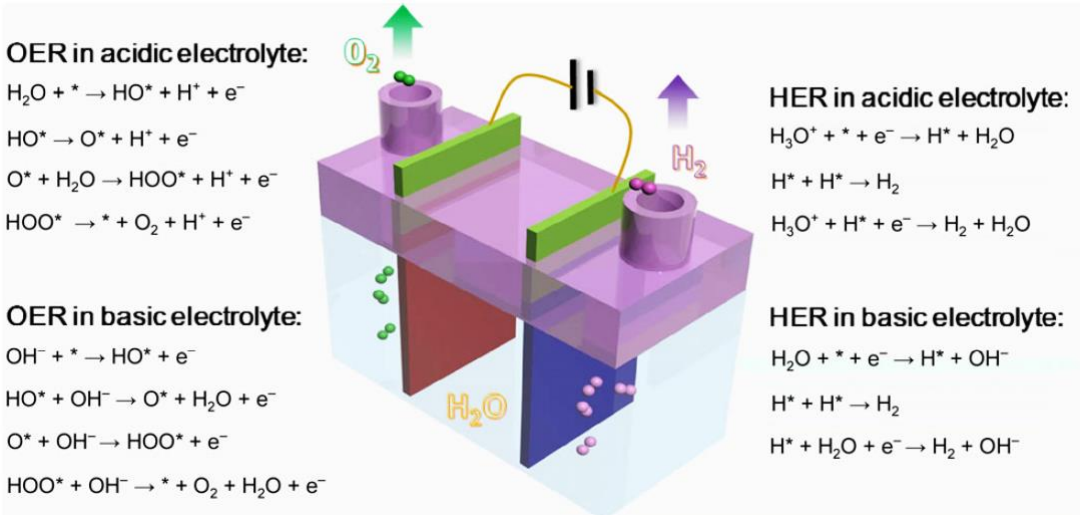

Figure 2.2 Possible reaction pathways in alkaline and acidic electrolytes [2]

2.2 Evaluation Parameters for EWS Half Reactions

2.2.1 Overpotential (η)

In theoretical calculations, the standard reduction potential is E^0_{H/H_2O}= 0 V *vs* reversible hydrogen electrode (RHE) and 1.23 V *vs* RHE for HER and OER, respectively [4]. Due to slow kinetics of half reactions, it generally requires an extra potential for initiation of reaction to overcome a certain activation energy barrier that is known as overpotential (η) in electrochemistry. Nernstian potential describes thermodynamic equilibrium potential (E_{RHE}) depending on pH which can be nonvalid by referencing to RHE.

$$E_{HER} = E^0_{(H^2/H^+)} - RT/F \times ln\,(a_{H+} / P_{H2}{}^{½}) = -0.059 \times (pH)\ V\ vs.\ NHE = 0\ V\ vs.\ RHE \quad (1)$$

As can be seen in Equation (1), for each pH increase, Nernstian potential linearly shifts 0.059 V, while being directly equals to zero on the RHE scale. In practical implications, hydrogen evolution could not initiate at equilibrium except for some cases; therefore, always requires extra cathodic potential to surpass the activation barrier. Reaction interface generally identify the magnitude of the barrier. For a specific current (*i*), applied potential (*E*) can be calculated as follows:

$$E = E_{RHE} + iR - \eta \quad (2)$$

where *i*R is the ohmic potential drop (also called *i*R compensation) related to series resistance (R) of the system. For both half reactions there are three sources of overpotential [19]. By choosing efficient materials as electrocatalysts, intrinsic activation overpotential and by constantly stirring the electrolyte, concentration overpotential can be decreased effectively. The overpotential due to uncompensated resistance can be manually extracted by resistance and current density multiplication.

Smaller value of overpotential, tendering higher activity. Desired HER catalyst should have 100 mV overpotential or even less; however, in practical applications, there are many factors that escalate activation barrier of the reaction. Establishing highly active electrocatalysts on electrode surface can lower the barrier and minimize large overpotentials for both HER and OER.

2.2.2 Tafel Plot (Tafel Slope and Exchange Current Density)

The Tafel plot is one of the key parameters to evaluate and compare electrocatalytic activity of materials. Tafel plot basically leads to two significant parameters: Tafel slope (b) and exchange current density (j_0). Tafel slope is obtained from linear part of Tafel plot at appropriate overpotential region by fitting the *i*-E plot based on Tafel equation as shown below:

$$\eta = a + b \log(j) \quad (3)$$

where η, a, b and *j* are overpotential, Tafel constant, Tafel slope and current density, respectively. By replotting the polarization curve (e.g. linear sweep voltammogram as a log(|j|) versus η) linear portion of the plot can be acquired [4] . Tafel slope is an intrinsic parameter and could identify the reaction pathway as HER rate determining step. Tafel slope expresses the overpotential required to raise the current density by one order of magnitude [16]. A smaller Tafel slope causes a steep rise of current density indicating higher charge transfer ability. Along with increased overpotential, sharp increase of catalytic current by smaller charge transfer coefficient can be obtained by smaller Tafel slope values [5].

Exchange current density can be derived from linear portion of Tafel plot and x-axis intersection under the assumption of equilibrium condition (overpotential equals to zero). Therefore, j_0 refers the rate at the thermodynamically equilibrium potential. Platinum shows highest value as 1 mA/cm^2 [1], [16]. The exchange current density is the internal reason for activation potential barrier and depends only on material, electrolyte and temperature. Smaller exchange current density reaction requires higher overpotential to perform the reaction [4].

In order to achieve higher overall activity, electrocatalyst should has small overpotential, low Tafel slope and large exchange current density. However, for HER electrocatalysts the low Tafel slope often indicate smaller current densities also. This state of connection between parameters, limits improving performance of catalysts, leading to find a middle ground in terms of intrinsic properties. For performance comparison of electrocatalysts materials for HER, the potential required to achieve a current density of 10 $mA.cm^{-2}$ [1] is referred as the figure of merit.

By measuring the quantity of collected gas experimentally, Faradaic efficiency can be obtained to measure number of electrons that transferred for the target half reactions

in EWS except for other side reactions. However, in experimental data Faradaic efficiency is obtained usually 100% and therefore, it is not a suitable parameter to compare activation of electrocatalysts effectively.

Stability measurement is another key parameter to prove applicability of the material especially for commercial purposes. Most of the electrocatalysts decomposes or reacts with electrolyte under extreme conditions such as severe pH range, temperature *etc*. Chronoamperometry and cyclic voltammetry (CV) measurements are the two most used methods to test durability of materials. The tested current density and duration should be more than 50 $mA.cm^{-2}$ and 20 h respectively, to meet industrial requirements [12]. For the second method, if before and after cyclic experiments, recorded polarization curves are not much differing from each other, stability of the electrocatalyst can be proven to some extent.

2.3 Fundamentals of HER

In EWS process, among the two half reactions, HER (hydrogen evolution reaction) is simpler one by consisting only two steps. Protons are reduced on the cathode of the cell that is also known as HER process. Yet, this reaction regularly requires a catalyst due to slow kinetics of the proton absorption on the electro surface, trailed by desorption of hydrogen molecule [3]. For one molecule of H_2 production, two-electrons are transferred in HER. These two steps include Volmer adsorption and desorption process. The first step is Volmer adsorption step covers H_2O or H^+ adsorption on the cathode where hydrogen intermediate binds to the catalysts:

$$H_3O^+ + e^- \rightarrow H_{ads} + H_2O$$

First reaction step has a Tafel slope of 120 mV/dec [3]. For the desorption of H_2 from the cathode there are two possible routes called Tafel step or Heyrovsky step depending on the coverage of H_{ads}. HER kinetics dependent on the reaction pathway that can be catalyst or potential dependent. Due to various crystalline facets on the surface of the single electrocatalyst, these two pathways may be simultaneously operated [1].

Heyrovsky process applies when the low coverage of $H_{ads,}$ as electrochemical desorption step [4]:

$$H_{ads} + H^+ + e^- \rightarrow H_2$$

Heyrovsky step has 40 mV/dec Tafel slope [16]. Second possibility is chemical desorption of H_2 known as Tafel step (recombination reaction):

$2\ H_{ads} \rightarrow H_2$

Tafel step (chemical desorption) takes place if the H_{ads} coverage of electrode surface is high [4] with a Tafel slope of 30 mV/dec [3].

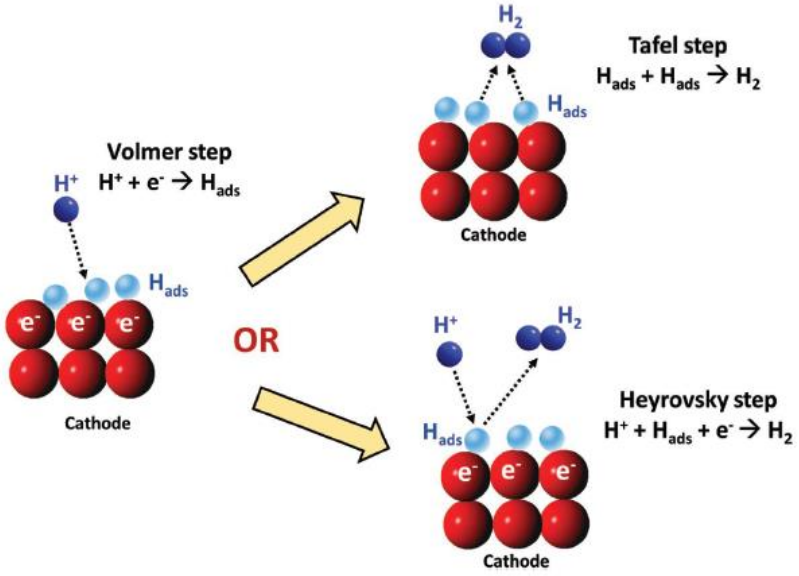

Figure 2.3 Schematic representation of pathways for HER on the cathode [6]

As can be seen from constituent chemical steps of HER mechanism, adsorbed hydrogen always takes place thus, the free energy of adsorbed hydrogen (ΔG H_{ads}) is a well-known activity descriptor in electrocatalyst. As indicated in Sabatier principle, hydrogen bonding and releasing ability should be well-balanced (intermediate bonding energy with intermediates) in ideal HER catalyst regardless of the pH of solution. ΔG H_{ads} should be near zero eV such as noble metal platinum which shows highest HER activity [1], [4], [5]. ΔG H_{ads} can be analyzed via density functional theory (DFT) calculation. Lower ΔG H_{ads} means stronger binding strength and therefore, decelerates hydrogen releasing. On the other hand, higher ΔG H_{ads} results in endothermic proton/electron transfer step [5].

In the light of Sabatier principle, an ideal HER catalyst should have large amount of active sites with optimum electron density in order to offer moderate bonding strength with adsorbed hydrogen to ensure both adsorption/desorption is not hindered. It should also have low charge transfer resistance with interface while maintaining stability for long lasting working hours [6].

HER activity for many electrocatalysts dramatically decreases in alkaline solution than acidic because of sluggish kinetics of water dissociation. For alkaline electrolytes, determining the kinetic barrier to evaluate intrinsic activity of electrocatalysts is important factor for HER [5].

H_2 molecule, depending on the pH of the solution, can be produced by hydronium (H_3O^+) or water molecule reduction. Hydrogen proton is used as hydronium replacement in acidic electrolytes. Both hydronium and water molecule reduction occur in neutral solutions, due to low concentration of hydronium it is only dominated at low current density. Water molecule reduction with low proton concentration might occur in acidic environment. Since water splitting cell operates with high current density, in alkaline media water molecule reduction takes place for HER [5]. Reaction steps for HER in different pH media as given below:

HER in acidic electrolyte:

$H^+ + e^- \rightarrow H_{ads}$ (Volmer)

$H^+ + e^- + H_{ads} \rightarrow H_2$ (Heyrovsky) or $2\ H_{ads} \rightarrow H_2$ (Tafel)

HER in alkaline electrolyte:

$H_2O + e^- \rightarrow H_{ads} + OH^-$ (Volmer)

$H_2O + e^- + H_{ads} \rightarrow H_2 + OH^-$ (Heyrovsky) or $2\ H_{ads} \rightarrow H_2$ (Tafel)

In the acidic solution, HER mechanism starts with Volmer step by the reaction between hydrogen proton with an electron and forming adsorbed hydrogen for second step. Similarly, for the alkaline solution, reaction with the electron occurs between water molecule and result in formation of adsorbed hydrogen with hydroxide in Volmer step. For alkaline HER, an extra H_2O adsorption and dissociation included in first step so, leading to slower kinetics than acidic HER. Thus, activity for HER in alkaline solution is also related to ability to decompose water aside from the free energy change [12].

2.4 Fundamentals of OER

Water oxidation reaction or oxygen evolution reaction (OER) is the core reaction to perform reversible process with oxygen reduction reaction (ORR) and HER. Molecular oxygen is produced by proton/electron-coupled procedures [20]. OER takes place at the

anode side of the cell and it is a four-electron process with one molecule of O_2 evolved. This four-step reaction mechanism can be given as follows:

1) $OH^- + * \rightarrow HO* + e^-$

2) $HO* + OH^- \rightarrow O* + H_2O + e^-$

3) $O*+ OH^- \rightarrow HOO* + e^-$

4) $HOO* + OH^- \rightarrow * + O_2 + H_2O + e^-$

where O*, OH* and OOH* are the absorbed intermediates [4].

OER is highly pH dependent, under standard conditions the equilibrium half-cell potential (E^0_a) for acidic/neutral and alkaline conditions are 1.23 V and 0.404 V, respectively. In the alkaline solution, four hydroxyl groups are oxidizing and forms water and oxygen molecules; while in acidic solution, two water molecules form four protons and oxygen molecule. In line with the Nernst equation, reaction potential shifts 0.059 V per unit pH change. With normal hydrogen electrode (NHE), external current is necessary to perform the OER at neutral pH electrolyte to create 1.23 V potential difference. Therefore, reversible hydrogen electrode (RHE) is mostly preferred to maintain the voltage as 1.23 V for OER [20].

Similar to HER, noble metal electrocatalysts perform the best OER activity such as Ir, Ru and their oxides (IrO_2, RuO_2), especially in acidic systems. For the case of alkaline solutions, some 3d transition metals (Fe, Co and Ni) showed remarkable performances and attracted interest to examine the group in more detail. Some of the reported transition metal-based compounds (chalcogenides, phosphides and borides) showed better activity than oxides [4]. However, OER continues by means of surface oxides while presence of metallic core aides in conduction of charges efficiently. OER generally accompanied by oxidation of catalyst and produce intermediates that increase oxidation wave and might leads spanning in the scale of $\mu A.cm^{-2}$ to $mA.cm^{-2}$. In such circumstances, 10 $mA.cm^{-2}$ metrics should be used cautiously to avoid overestimation of activity. This can be achieved by measuring volume and concentration of product gases during the reaction in the cell by using Hoffman apparatus. Exact validation of current from OER alone without affected by corrosion and capacitive currents is important parameter to evaluate performance of electrocatalysts [2]. Tailor the structure of metal boride catalyst as metallic core-shell, not just presents more surface active sites yet additionally charge

conduction pathways [9]. For monometal borides, unexpectedly high OER performance is due to formation of metal oxide/ (oxy)hydroxide on the reaction interface such as formed CoOOH on the CoB metal. In this stage, boron element prohibits the complete oxidation of cobalt by donating electrons [4]. Finally, the OER requires four electrons move to produce oxygen molecule and kinetically favourable process takes place with single-electron transfer at each OER step. Along this line, accumulation of energy at each step establishes sluggish OER kinetics and results in higher overpotentials [20].

2.5 TMB Electrocatalysts in the Literature

Transition metal/metalloid based electrocatalysts are appraised as the most promising non-noble materials. Transition metal carbides, nitrides, chalcogenides and phosphides are highly studied for HER while transition metal oxides, hydroxides and metalloids (generally N, P, S, Se and B *etc*.) along with transition metals for OER[4]. TMBs (transition metal borides), come forward thanks to some unique properties for water splitting applications in comparison with other TM-based counterparts. First of all, the reverse electron transfer in amorphous TMBs (from boron to metal) provides electron rich metal sites and increase activity [9]. Modified electronic structure of TMBs, naturally decreases kinetic barrier. Nevertheless the reaction pathway chases steps as usual for HER, a widely-accepted cause for such high activity is still missing [4]. Gupta et al., proposed a reason as electron transfer from boron to *d*-band of cobalt for Co-B compound [9]. Due to higher electronegativity of boron, the *d*-band orbitals of cobalt filled with more electrons. Higher electron density at Co active sites enhances donating ability of cobalt. Boron itself is not the direct active site however, by donating electrons it provides stability, increased HER activity and prevent oxidation of the metal by being sacrificial element. The electron transfer from 2p orbit of boron to 3d (or 4d) of TM, promoting adsorption and desorption of H* and OH^- intermediates [4]. Secondly, TMBs usually possess amorphous structure with long-range disorder, chemical stability, high concentration of unsaturated sites [10]. Further increase in catalytic activity of TMBs can be achieved by tailoring the structure from amorphous to crystalline by subsequent annealing [21]. Additionally, with surface oxidation of TMBs, boron oxide, borates, TM oxides and TM (oxy) hydroxides formation enhances OER performance [2].

The first TMBs research is traced back to 1974 by Kuznetsova et al. about HER activity of diborides (ZrB_2, NbB_2 and TaB_2) and W_2B_5 in 1 M H_2SO_4 acidic electrolyte

[1], [5]. In 1992, amorphous Ni_2B in alkaline environment for hydrogen evolution was reported by Los and Lasia [22]. After the lingering, in 2012, Vrubel and Hu reported, commercially available Mo_2C and MoB show high activity for HER in both acidic and basic solutions [23].

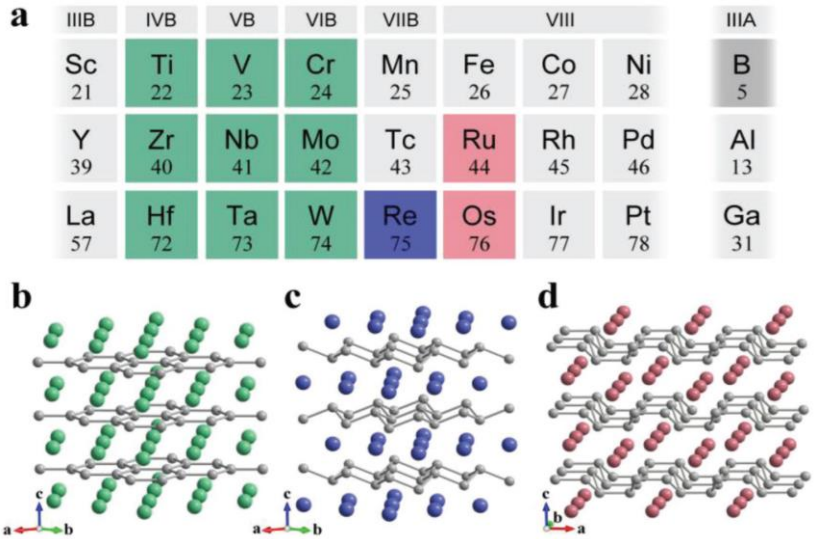

Figure 2.4 a) 12 transition elements that are used for synthesis of MB_2. A schematic of crystal structures of b) AlB_2 type c) ReB_2 type and d) RuB_2 type diborides with color codes [16]

The crystal structure of metal diborides that can be formed by 12 transition elements, is classified into three types: a) AlB_2-type, b) ReB_2 type and c) RuB_2 type diborides (see Figure 2.4) Boron atoms form graphene-like layers with covalent bonding in AlB_2 (P6/mmm) type diborides while introducing chair and boat confirmations for ReB_2 and RuB_2 types, respectively [16]. TMBs with 3D metallic framework with 2D borophene subunits have attracted attention for electrocatalytic applications. Diborides due to the layered structure formation, exhibit unique properties such as hardness, low electrical resistivity, high thermal conductivity, chemical stability [7]. Even though their well-defined crystal structures are highly studied, the electrocatalytic activity of most of the metal borides remained unreported. Diborides show more abundant catalytic sites and better conductivity than other types of electrocatalysts (e.g. metal disulfides) [16]. Especially for the OER half reaction, there are only limited number of articles can be found in the literature regardless of the pH of the electrolyte solution. Lack of reports about the performance of metal diborides for EWS can be attributed to harsh synthesis conditions and insufficient knowledge on the design principles.

ΔG H_{ads} is a widely used indicator for evaluating the HER activity of electrocatalysts theoretically as mentioned in HER fundamentals part of this thesis. Hydrogen adsorption behaviour of materials is harnessed to its intrinsic electronic structure [24]. Li et al., calculated ΔG of atomic H bonding at most energetically favoured part (001) on the metal surface of 12 transition metal diborides [16]. Since smaller value (near zero) indicates better activity, the group reported the order (see Figure 2.5a) as: group VIII diborides (RuB_2 and OsB_2), group VII B diboride as ReB_2, group VI B diborides (TiB_2, HfB_2 and TiB_2). This order shows RuB_2 has better activity for HER among diborides with a linear correlation between Gibbs free anergy and d-band center. Its also worth to mention that RuB_2 has much lower d-band center and obvious smaller ΔG H_{ads} than elemental ruthenium element indicating that boron addition improves HER activity. In comparison with noble metal platinum, RuB_2 has slightly lower d-band center and smaller absolute value of Gibbs free energy and therefore, ruthenium diboride is expected to show a better catalytic activity than Pt.

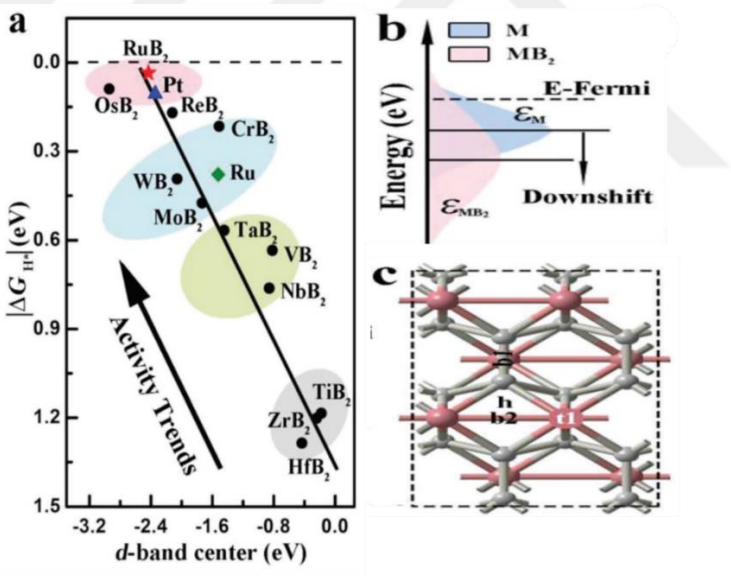

Figure 2.5 a) Linear correlation between absolute value of hydrogen adsorption free energy and d-band center of diborides in comparison to Pt and Ru. **b)** Boron effect on the d-band center of metal. **c)** Adsorption sites for hydrogen on the RuB_2 (001) surface [16]

As can be seen in Figure 2.5b, coupling interactions between boron sp- orbitals and metal d-orbitals, broaden the bandwidth of d-band of metallic Ru from 5.04 eV^2 to 7.18 eV^2 in RuB_2. With unchanged d-band filling, center of RuB_2 downshift from Fermi level, resulting in reduced hydrogen binding strength and thus, better activity [16]. To be able to compare inherent activity of different catalysts, polarization curve current density is

normalized by electrochemical active surface area (ECSA) or the surface area [12]. Overpotential value generally taken as the value to reach the 10 mA.cm^{-2} current density. As Li et al. reported, in acidic electrolyte, overpotential value of RuB_2 is 18 mV (Figure 2.6b) and highly close to commercially used Pt/C catalyst (17 mV); in alkaline electrolyte (Figure 2.6c), required overpotential is 28 mV as lower than Pt/C electrocatalyst (37 mV) [5], [16] that is normalized by the surface area from BET characterization. Apart from these, nickel, cobalt and iron based mono or diborides have been widely studied for their HER performances as well as their surprisingly high OER performances due to the formation of active species during electrolysis, especially in alkaline electrolytes owing to high corrosion resistance. However, non-precious metal alloys are not the better option in acidic environment than noble metal catalysts.

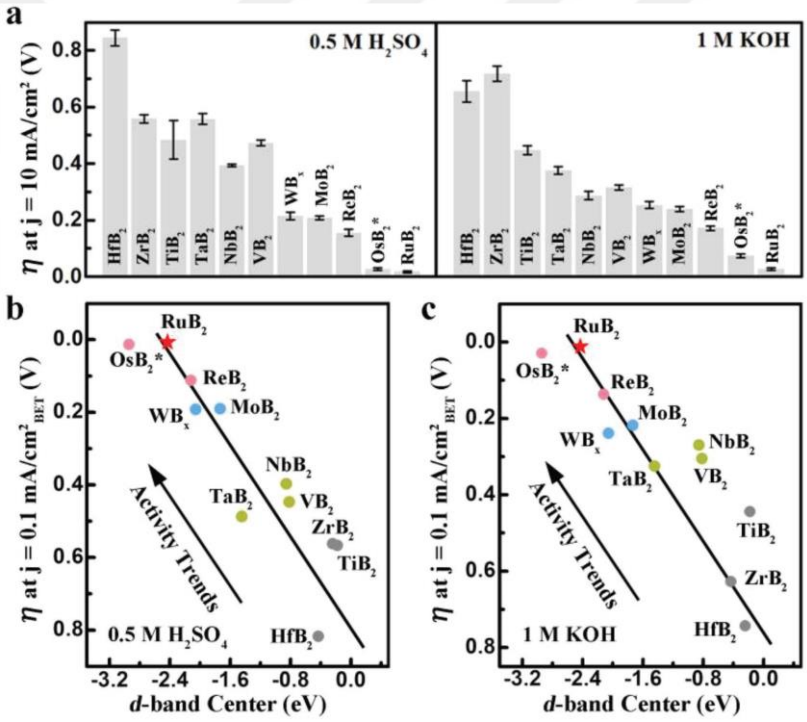

Figure 2.6 a) Experimental overpotentials at current density of 10 mA.cm^{-2} in acidic electrolyte (left) and alkaline electrolyte (right). Linear correlation of d-band center and overpotentials at 0.1 mA.cm^{-2} current density **b)** in acidic solution and **c)** in alkaline solution [16]

Even though, in d-band center and absolute Gibbs free energy of hydrogen adsorption linear fitted graph, ZrB_2, TiB_2 and HfB_2 has placed in the lower part of the line, there are increasing number of articles focusing on them in time. Various of strategies have been found to further improve in catalytic activity of materials that will be explaining in broad sense at the following part of the thesis. Mazánek et al., reported activity of commercially

available 9 different metal diborides in terms of hydrogen evolution and oxygen reduction reactions in both 0.5 M H_2SO_4 solution and phosphate buffered saline (PBS) as pH 7.2 [3]. In the morphology characterization, for the 4th group of diborides especially ZrB_2 and TiB_2, by reason of strong boron and metallic layers interaction, the group observed generally spherical characteristics with developed crystalline facets along with agglomeration of particles with sizes exceeding 10 µm. Most importantly, among these metal diborides (see Figure 2.7b), ZrB_2 with the lowest Tafel slope (173 mV/dec) and overpotential 0.97 V at 10 mA.cm^{-2} current density is the most promising HER and ORR electrocatalyst followed by HfB_2 (η= 1.05 V, 196mV/dec Tafel slope) and with very close overpotential of TiB_2 (η= 1.07 V). These three electrocatalysts have shown better activity in hydrogen peroxide production than bare GC reference material.

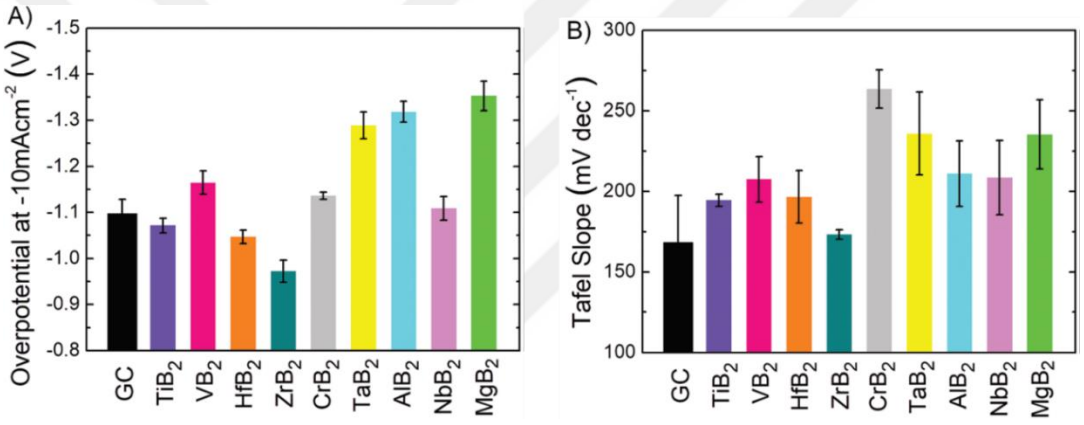

Figure 2.7 a) Overpotentials required to reach 10 mA.cm^{-2} of layered diborides for HER b) Obtained Tafel slopes (mV/dec) of the metal diborides [3]

Although the commercially purchased ZrB_2 powder used by Mazánek et al., contains impurities and relatively big particle size due to agglomeration, showed better HER performance than other layered diborides. Additionally, because of the electrode preparation technique employed, results can be considered as noncompatible and unreliable. By engineering properties of ZrB_2 and synthesizing better quality fine and pure powders, better activity can be achieved than reported performances for ZrB_2, TiB_2 and HfB_2. Solid solutions of layered diborides also resulting in enhanced activity for HER in both acidic (1M H_2SO_4) and alkaline (1 M NaOH) solutions [11]. Sitler et al., reported stable solid solutions of ZrB_2 and HfB_2 mixed in 1:4, 4:1 and 1:1 ratio denoted as $Hf_xZr_{(1-x)}B_2$ (x= 0.2-0.8). Commercially available powders first ball milled for 3 hours and then compacted at 1700 °C using spark plasma sintering (SPS). Obtained particles have grain sizes between 1.5-3µm with relatively high porosity resulting in high exchange current

density. The group reported better activity in alkaline than acidic environment even so sustainable stability for both conditions. The Tafel slope of solid solutions reported as 0.15-0.18 V/dec except for pure HfB_2 (0.38 V/dec) in acidic electrolyte (1 M H_2SO_4). For alkaline conditions, 0.12-0.27 V/dec is reported which indicates high activity range for both electrolytes used. In 1 M NaOH solution, redox reaction is not mass transfer controlled opposing to acidic case. The low density of states (DOS) at Fermi level affects activity adversely. The low activity of pure HfB_2 in acidic environment is associated with its electronic structure. As indicated, it has 100 mV/dec Tafel slope and 540 mV overpotential for HER in alkaline media indicating that the operating mechanism is Volmer step. Higher porosity level may lead higher current density. ZrB_2 has 270 and 180 mV/dec Tafel slopes and 650 mV and 690 mV overpotentials in alkaline and acidic conditions, respectively. Among various *x* values for solid solution, x= 0.5 resulted in the best activity as 120 mV/dec, 150 mV/dec Tafel slopes and 420 mV, 590 mV overpotentials at 10 $mA.cm^{-2}$ current densities, respectively. $Hf_{0.8}Zr_{0.2}B_2$ has 260 and 150 mV/dec Tafel slopes and 610 and 550 mV overpotentials in 1 M NaOH and 1 M H_2SO_4 solutions.

2.6 Further Adjustments of Properties

TMBs are promising candidates for commercial EWS systems however, tailoring the properties is inevitable to obtain a better electrocatalytic performance for further efficiency. In line for this objective, a series of strategies have been advocated eventually such as phase engineering (crystallinity, boron layer construction *etc*.), morphological engineering (nanosizing *etc*.), component regulation (doping, boron to metal ratio *etc*.), hybridization (TMB/rGO, TMB/TMX *etc*.) and surface oxidation [2], [25]. The main reasons for the enhancement are increasing the intrinsic activity, providing more exposure on active sites, increasing conductivity and stability of TMB materials [4].

Nanosizing

TMBs tend to agglomerate during synthesis and resulting in large particle sizes. Conventional production techniques such as direct reaction of elements, solid-state synthesis generally requires elevated temperatures for reaction of TMBs, such high temperatures promote grain growth. Hence, dispersion of the particles with accomplishable smallest particle size plays a key role for enlarging the specific surface area (SSA). Large SSA provides more accessible active site exposure, improving the

electrical contact, facilitates interaction between catalyst and electrolyte solution. Building nanostructures (*e.g.* nanospheres, nanochains, nanosheets) [2] or downsizing the material from micron to nano-scale are one of the most efficient strategy of superior activity. Nanostructures, besides offering more exposure on active sites, also enhances the diffusion and penetration of electrolyte solutions in the EWS process [26]. Downsizing introduces structural disorders or defects that serves as active sites in catalysis by changing the local electronic structure of the material. Amorphous structures generally provide better activity for electrocatalysis. Short-range order is harmful to photonic and electronic properties however, it creates coordinative unsaturated sites on the catalytic surface center [27].

Nanosizing especially increases the OER activity, one representative example of high SSA atomically thin (6.6 Å) sheets with 200-300 nm lateral dimensions of amorphous Ni_xB reported by Masa et al., requires 380 V at 10 $mA.cm^{-2}$ overpotential in 1M KOH electrolyte solution. Sample annealed at 300 ˚C for 2 h under Ar atmosphere, when supported by Ni foam, overpotential drops to 280 mV at 20 $mA.cm^{-2}$ for OER. Oxygen evaluation takes place when surface oxidation occurs on Ni atom (NiOOH) by core-shell structure at 1.7 V [28]. Ultra-thin layers play a crucial role for achieving one of the best reported OER activity among nonprecious materials.

Doping or alloying

Cationic doping further improves electrocatalytic activity of TMBs by providing more active sites exposure as in the case of nanosizing. Almost every strategy to enhance performance of TMBs can be obtained by hetero-metal doping. Doping can positively affect the overall activity by enlarging the SSA by hindering agglomeration of TMBs. Additionally, it modulates the electronic structure and crystal structure [2]. Metal doping also shapes the morphology by preventing agglomeration apart from increasing conductivity and intrinsic activity [9]. Anionic doping is stemming from electronegativity between anions and boron. The non-metal and metal dual-doping (incorporation of Co and P together) into Fe-B resulted in better performance for both half reactions [29]. The activity of metal-metalloid catalyst can be increased via charge transfer by incorporation of metals (Fe, Ni and W *etc.*) [10]. Composite structures, as in the case for most of the application areas, provide the best combination of properties of starting materials

individually. In the case of TMBs, hybridization with other promising nano-catalysts results in better conductivity, more active sites, better stability and electroactivity [2].

Degree of crystallinity

Amorphous TMB nanomaterials, for both half reactions, have shown great activity in the literature [4], [9], [24], [28]. In HER, high electrical conductivity leading charge transfer throughout the electrocatalyst and reduces resistance at the electrocatalyst interface [30]. For electron transport, theoretically, the Fermi energy level is the driving force. In fact, higher conductivity achieved by higher electron density near Fermi level. Since increase in number of active sites for exposure can be obtained by nanosizing, annealing temperature should be optimized for the crystallinity degree in consideration. Amorphous phases have more under-coordinative and unsaturated sites comparing to crystalline analogues [4]. For OER, while activity of amorphous Co-Ni-B-O decreases with increasing crystallinity as annealing temperature increases [31]. On the other hand, contradictory results showed the moderate increase in crystallinity can upgrade the activity of TMBs [21], [28], [32]. High annealing temperature may cause the lattice strain on metal atom and alleviates kinetic and thermodynamic barriers for the formation of intermediates (e.g., OOH*) so, improves OER activity. Nevertheless, at elevated synthesis temperatures, catalytic activity reduces due to large grain formation leading to reduced SSA [2]. Li et al., reported crystallinity dependence on catalytic activity of as prepared amorphous FeB_2 by annealing. FeB_2 annealed at 600 ˚C, converted to crystalline and resulted 61 mV and 296 mV overpotentials at 10 $mA.cm^{-2}$ for HER and OER, respectively. The partially crystalline sample (annealed at 350 ˚C) performed better activity than amorphous or crystalline (annealed at 450 ˚C) [33].

Metal to boron stoichiometric ratio

Generally, increasing boron content to some extent, may positively influence the catalytic activity of TMBs. This situation is familiar from metal phospide electrocatalysts. DFT calculations show that the boron-rich metal provides an appropriate binding energy of chemisorption and desorption of H* intermediates thus, enhanced activity especially for HER. Boron rich FeB_2 possesses better activity than Fe_2B with same morphology and SSA [33] for both OER and HER. In the case for Mo-B, in the acidic environment, the HER performance is increasing as the boron content increase in the order of Mo_2B, MoB and MoB_2 [34]. Additionally, besides assisting electron transfer, boron ratio can influence

the morphology of the metal compounds. Zhang et al., reported that the average particle size of NiB_x electrocatalyst decreased from 2.27 to 0.55 µm as boron content increases. Electrocatalytic performances of Ni-B materials are decreasing in the order of $NiB_{0.54}$, $NiB_{0.48}$, $NiB_{0.36}$ and $NiB_{0.27}$ [35]. On the other hand, contradictory results have proven that further increasing the boron content may reduce the catalytic performance of TMBs. Ma et al., synthesized Co_xB by ball milling which x= 1-3. Co_2B on a carbon paper support, showed the best activity of 287 mV and 109 mV overpotentials at 10 $mA.cm^{-2}$ current density for OER and HER, respectively and over 12 h stability [36]. Sitler et al., reported the metal-rich borides (B/M= 1.86) showed better HER performance than the stochiometric diborides [11]. DFT calculations attribute the higher activity of metal rich borides to the increased electron amount in the *d*-orbitals of metal. With the introduction of boron vacancies, electron density at the Fermi level increases and provides better activity [4]. In conclusion, tuning the optimum metal to boron ratio of TMBs could highly contribute the overall efficiency of the catalysts.

Supporting materials

Electrocatalysts with low electrical conductivity causes a voltage drop against electrode and requires an extra overpotential [4]. To avoid the unnecessary resistant presence at the catalyst interface, a highly conductive material (higher electron density around Fermi level) that can facilitate the charge transfer is needed. Loading the electrocatalyst on a porous, conductive substrates, significantly boost the conductivity and activity of the materials. Porous supports provide a binder-free loading on electrode thus corrosion resistance of binder will no longer a problem [8]. TMBs can be supported with nickel foam, copper foam and carbon-based supports [6], [25], [31]. Porous structure can disperse the catalyst particles thus, providing more active sites and larger SSA [2]. Ni foam is the most used support for metal borides. However, compared to other current collectors, Ni foam itself is intrinsically active for both half reactions and therefore, it is difficult to separate the activity of electrocatalyst material individually. To make a fair comparison, measurements have performed with inert support [4].

Surface oxidation

When TMB catalyst is exposed to water or air, surface oxidation process takes place. Tailoring the metallic core and shell structure for catalyst is often employed and have positive effect on the OER performance. The inevitable formation of boron-oxo and TM-

oxides or (oxy) hydoxides on the material is generally considered as the one of the reasons for high OER performance of the TMB electrocatalysts. Apart from structural engineering, oxide-rich surface layer can be generated during the EWS in situ process [2]. Li et al., reported the transformation of $Ni(OH)_2$ into catalytically active NiOOH on the boronized nickel plate during OER process before stabilization (J. Li et al,. 2019). Formed borates modify the electronic structure and enhance the electron density around metal atom during OER process. Reaction rate accelerated while pathway remained the same. Generally surface oxidation leads better OER activity however lower HER activity. Most of the studies indicates that oxide layer on TMBs has negative effect on HER while some articles evidenced in the alkaline electrolytes TM- hydoxides also can facilitate HER activity [2].

2.7 The Challenges of TMBs in EWS

As mentioned in further adjustments for TMBs, more exposure on active sites is crucial to obtain better activity. Designing and synthesizing nanostructured materials with high SSA, tailoring the crystal structure that active planes can be exposed, loading the material on porous and conductive support are mostly employed strategies to take advantage of activity of material [4]. Additionally, increase in the amount of electrocatalyst on the electrode also may increase the number of active sites ranging from 1 mg/cm^2 to 10mg/cm^2 that results in lower overpotential for OER (<200 mV) [38]. High amount of catalyst loading is not a cost-effective way for commercialization. Upscaled electrolyzers generally utilize 0.25 mg/cm^2 of electrocatalyst loading, hence experimental studies should be with the loading of 0.1-0.5 mg/cm^2 typically [6].

In some cases, in situ surface oxidation on the surface of amorphous metal borides, may improve the OER activity. A thin layer of oxide/hydroxide layer on the metal borides particle surface is consistent with the core-shell structure. Even though the thin oxidation might not help with the OER performance, in situ generated layer may diminish the conductivity and block the exposure on the active sites for hydrogen evolution reaction [4].

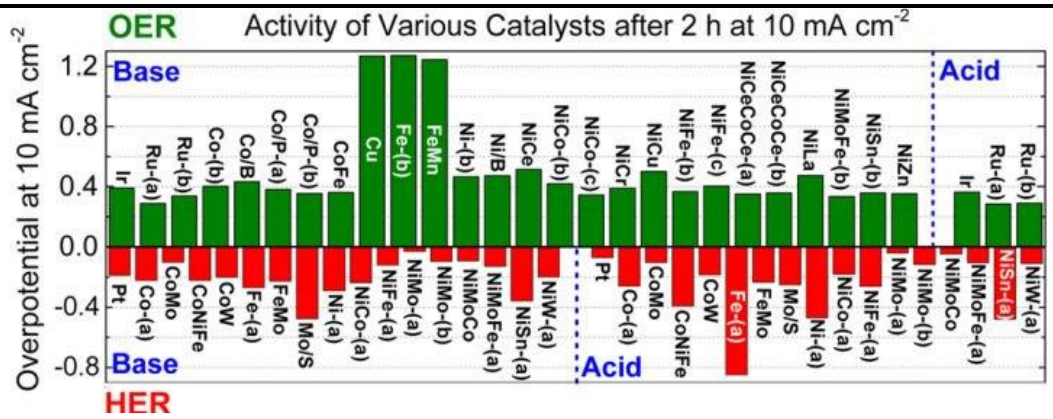

Figure 2.8 OER/HER activity of diverse catalysts in acid/base electrolyte [4]

The stability failure issue is more important for HER than OER in the process, due to exfoliation by abundant bubble evolution. Maintaining the stability for long time while conserving the high catalytic activity is one of the main issues for whole electrocatalytic materials. An ideal catalyst should remain stable for long operation hours under both acidic and alkaline environment, preferably. TMBs suffer from low resistance to acidic environment and unfortunately, the most active OER electrocatalyst are noble materials and their oxides (see Figure 2.8). Nafion binder (perfluorinated alkyl sulfonate iomer solution) is a commercially used for binding the electrocatalyst to electrode surface. For both HER and OER, in acidic electrolyte, Nafion thanks to its unique structure and stability, supports electron and hydrogen transfer [4].

Chapter 3:
MATERIAL CHARACTERIZATION TECHNIQUES

3.1 X-Ray Diffraction (XRD)

X-ray diffraction (XRD) is a non-destructive technique that is used to determine the crystallographic structure of materials. Incident X-rays irradiates the material and their intensities and scattering angles are measured to obtain diffraction pattern. The XRD patterns of the samples were obtained by X-ray diffractometer (XRD, Rigaku Mini Flex 600; Cu Kα (λ = 1.5418 Å)). X-ray diffraction spectra were recorded in the 2θ range of 20° to 90° with 40 kV voltage and 20 mA current applied.

The X-rays are produced by bombarding the target material (Cu, Fe, Mo, Cr) with electrons in a cathode ray tube. The elastic scattering through interaction of incident X-rays with electrons, mostly result in destructive interference, however, in a few specific directions for each material, they interfere constructively, as determined by Bragg's law $2d \sin\theta = n\lambda$, where d is the spacing between planes, θ is the incident angle, n is the order of diffraction and λ is the beam wavelength [39].

3.2 Scanning Electron Microscopy (SEM)

A scanning electron microscope (SEM) scans a focused high-energy electron beam over a materials surface and creates an image by using their interaction that can be used to obtain information about the surface topography, morphology of microstructure and chemical composition. The imaging process starts with generating a beam through electron gun, followed by condensing and focusing the beam onto sample by solenoid coils. Samples must be sputter coated to increase conductivity or dehydrated before analysis [40]. As the electrons interact with the sample secondary electrons, backscattered electrons, and characteristic X-rays are produced. A sample image can be taken with 20-130,000x magnifications with high resolution and intense detail by SEM. Two positively charged detectors collects the bounced secondary and backscattered electrons under vacuum and creates a black and white image [41]. In this study, to characterize the surface morphology and chemical composition, Zeiss Ultra Plus Field Emission Scanning Electron Microscopy (FESEM) was used at an accelerating voltage of 5 kV for Energy Dispersive X-ray Spectroscopy (EDS). Elemental mapping feature (EDS) with the conjunction with SEM, elemental composition and dispersion of each

element through sample can be evaluated. EDS feature of the SEM collects the information and creates an image through characteristic X-rays [41]. Energy dispersive detector analyses the X-ray emissions and assign appropriate elements, yielding the composition of atoms on sample surface [42].

3.3 Transmission Electron Microscopy (TEM)

Transmission electron microscopy (TEM) is similar to SEM however, in this case the electron beam passes through the sample and provides higher spatial resolution. High voltage highly focused beam (80- 200 keV) passes through a solid thin sample and projects an image onto fluorescent screen. Either coherent scattering or diffraction from lattice planes in the crystal of electrons, yielding the phase identification. Generated characteristic X-rays can be observed with another detector and can provide the qualitative elemental analysis information. TEM offers great resolution, interplanar spacing and lattice thickness can be measured from images [42]. The sample for imaging is usually sliced into thin section (<100 nm) and pre-treated with heavy metals (staining) [43]. In this work, the TEM images have been taken using a Hitachi HT7700 TEM instrument operating with a maximum acceleration voltage of 120 kV.

High-resolution TEM (HRTEM) uses both scattered and transmitted beams and creates an interference image [43]. HRTEM image formation relies on the phase contrast which is not interpretable intuitively. This contrast of the image arises from the interference on the image plane of the electron wave after diffracted from the specimen. The HRTEM method requires a close attention to the best understood in terms of the altered phase of electron wavefront by the specimen itself or the objective lens. The whole characteristics of the device as well as the performance of the objective and phase shift of the electron wavefront due to scattering potential of the specimen should be taken into account.

3.4 X-Ray Photoelectron Spectroscopy (XPS)

X-ray photoelectron spectroscopy (XPS) or electron spectroscopy for chemical analysis (ESCA) technique analyzes the elements constituting the sample surface, composition, chemical bonding state and overall electronic structure by irradiating X-rays on the sample surface and measuring the kinetic energy of the photoelectrons emitted from the sample surface. XPS usually operates under vacuum and detects all elements

except for helium and hydrogen. Only electrons that have escaped from the sample by travelling through the sample into the vacuum chamber can be detected. Considering this, the measured signal is mostly a surface-weighted signal. A THERMO K-ALPHA high-resolution XPS with Al Kα source was also employed to investigate the surface chemistry. Advantage software was utilized to fit the recorded patterns. Correction of the peaks was carried out with respect to the C1s peak at 284.5 eV.

In the XPS method, irradiated X-ray beam interacts with the electrons at the inner shell of atoms and transfers the photon energy to an electron. The photoelectron escapes the surface and its measured kinetic energy equals to binding energy of the electron. The number of electrons detected at specific binding energy (eV) constitutes the plot of an XPS spectrum and directly related to the ratio of the element within the detected volume of the sample. XPS peaks corresponds to the electron configuration (*e.g.*, 1*s*, 2*s*, 2*p*…) of the electrons of the atoms. XPS is not only identifies the present elements, also it shows the other elements which they are bonded to. This chemical bond shifts the bonding energy of the photoelectron and consequently that shift gives the structural information [42].

3.5 Brunauer-Emmet-Teller (BET) Analyzer

The surface area of the solid catalyst is an important factor that affects the overall activity of the material. BET theory basically explains the adsorption of gas molecules on the surface for the measurement of specific surface area (SSA) of the solid. Adsorbent gas should not react chemically with the surface of the material while having strong interaction with most solids therefore, in general nitrogen gas is utilized for probing.

Stephen Brunauer, Paul Emmett and Edward Teller were published an article about BET theory in 1938 [44]. Samples should be degassed under high vacuum and temperature before measurement. Additionally, a minimum of 500mg of the sample is required for successfully determining the SSA. Along with surface area, the amount of adsorbed gas on the surface also depends on the temperature, gas pressure and the interaction strength. After the saturation point of pressure, adsorption of the gas is finished, and adsorption layers is formed. When the sample is removed from the gas atmosphere, with highly precise pressure transducer monitoring the pressure changes, the sample is heated to release adsorbed gas. As a function of relative pressure, the amount of adsorbed gas data is collected.

Chapter 4:
RESULTS AND DISCUSSION

In this chapter, synthesis method of electrocatalysts, chemical characterization methods and their results, electrochemical measurement setup and electrocatalytic water splitting activity of as-prepared powders will be given in detail. The characterization results of unsubstituted and transition metal substituted diborides (ZrB_2 and HfB_2) will be evaluated in comparison with each other.

4.1 Synthesis Method of Electrocatalysts

Transition metal diborides can be synthesized via various types of commonly used methods by using different starting materials, reaction temperatures, post treatments etc. In the literature, countless of studies have shown the effect of several parameters on morphology, particle size of TMB electrocatalyst materials [1], [2]. Mostly, oxide or chloride of the transition metal, and a boron source such as elemental boron, boron oxide, boric acid, boron carbide, MgB_2, $NaBH_4$ etc. are employed as reactants. In the case of solid state reactions, magnesium or carbon can be used as reducing agent [10], [45]. Some of the possible synthesis reactions with TMO_2 (*TM*= Zr, Hf, Ti etc.) starting powder are given as follows:

$$2TMO_{2(s)} + B_4C_{(s)} + 3C_{(s)} \rightarrow 2TMB_{2(s)} + 4CO_{(g)} \quad (1)$$

$$7TMO_{2(s)} + 5B_4C_{(s)} \rightarrow 7TMB_{2(s)} + 3B_2O_{3(s)} + 5CO_{(g)} \quad (2)$$

$$TMO_{2(s)} + B_2O_{3(s)} + 5C_{(s)} \rightarrow TMB_{2(s)} + 5CO_{(g)} \quad (3)$$

$$TMO_{2(s)} + 2H_3BO_{3(s)} + 5Mg_{(s)} \rightarrow TMB_{2(s)} + MgO_{(s)} + 3H_2O_{(g)} \quad (4)$$

$$TMO_{2(s)} + 4B_{(s)} \rightarrow TMB_{2(s)} + B_2O_{2(g)} \quad (5)$$

$$3TMO_{2(s)} + 10B_{(s)} \rightarrow 3TMB_{2(s)} + 2B_2O_{3(s)} \quad (6)$$

$$TMO_{2(s)} + 3NaBH_{4(s)} \rightarrow TMB_{2(s)} + 2Na_{(s)} + NaBO_{2(s)} + 6H_{2(g)} \quad (7)$$

In this work, for micron-sized powders reaction (3) is employed successfully. Activated charcoal with the help of graphite crucible, reduced the transition metal oxide and boron oxide, therefore, offers an oxide-free transition metal for reaction with boron resulting in pure TMB_2 without any post treatment such as leaching, washing and drying. For reaction

(5), even though B_2O_2 leaves the system in gas form and resulting in pure product as in the third case, direct reaction requires higher temperatures and for doping studies stoichiometric control become harder. Boron oxide can be washed easily for the cases of (3) and (6), however, this situation can be considered as boron source loss. Using magnesium as reducing agent, generally results in MgO impurity. To obtain pure diboride, MgO impurity can be removed by diluted hydrochloric acid leaching followed by washing procedure. When sodium borohydride is used as boron source with metal oxide, volatile sodium and undesired Na-B-O compounds can be formed during reaction. Additionally, $TMCl_4$ source can be used for synthesis and generally resulting in finer particle sizes. Possible theoretical reactions with $TMCl_4$ (*TM* = Zr, Hf, Ti etc.) are given as follows:

$$3TMCl_{4(s)} + 10B_{(s)} \rightarrow 3TMB_{2(s)} + 4BCl_{3(g)} \quad (8)$$

$$TMCl_{4(s)} + 2NaBH_{4(s)} + Mg_{(s)} \rightarrow TMB_{2(s)} + NaCl_{(s)} + MgCl_{2(s)} + 4H_{2(g)} \quad (9)$$

$$TMCl_{4(s)} + 2NaBH_{4(s)} \rightarrow TMB_{2(s)} + 2NaCl_{(s)} + 2HCl_{(g)} + 3H_{2(g)} \quad (10)$$

$$TMCl_{4(s)} + 2B_{(s)} + 2Mg_{(s)} \rightarrow TMB_{2(s)} + 2MgCl_{2(s)} \quad (11)$$

Due to the lower boiling points of transition metal chlorides than their oxides, reactions can take place at mild temperature conditions and thus, usually resulting in finer particle sizes without permitting grain growth. For the reactions (9-11), Mg and Na salts can be washed easily with warm water and after drying under vacuum, pure nano-size TMB_2 can be obtained in powder form. In the case for both starting transition metal forms, boron source KBH_4 can be replaced with $NaBH_4$ in fact, using a borohydride source instead of boron itself, results in better reaction yield (<1 wt%) without high weight loss [46].

Additionally, for electrocatalysis purposes, most of the diborides are synthesized in the assistance of molten salt mixture. Variety of different salt mixtures have been studied for different synthesis and they directly affect the purity, formation of the side products, morphology and size of the product [47]. Highly used molten salts are as follows: NaCl/KCl eutectic point (50:50 wt%) mixture (T_m= 660 ˚C) [48], LiCl/KCl eutectic point (45: 55 wt%) point (T_m= 355 ˚C)[49], [50], KBr melt [51] and Mg/Na chlorides [47], [52]. Molten salt with low melting point is added as solvent to enhance the rate of solid-state reaction after heating above its melting point. Liquid salt, generally without reacting with main reactants, provides a media that increase diffusivity of the system leading well-

dispersed and fully reacted products. Anhydrous LiCl and KCl salts are mixed regarding to lowest melting point in binary phase diagram (eutectic point) under protected atmosphere and used as media for some nano-synthesis experiments.

For both ZrB_2 and HfB_2, first sets of experiments including pure and doped electrocatalysts were synthesized by mechanical activation followed by high temperature annealing. Since the direct reaction of elements requires elevated temperatures (~ 3500 K) as can be seen on binary phase diagrams, transition metals employed as their oxides accompanied by boron oxide for reduction synthesis with the help of activated charcoal powder. Micron sized ZrB_2 and HfB_2 syntheses were carried out regarding to equation (3). Figure 4.1 shows the main procedure steps for first trials of synthesis.

$$TMO_{2(s)} + B_2O_{3(s)} + 5C_{(s)} \rightarrow TMB_{2(s)} + 5CO_{(g)} \quad (3)$$

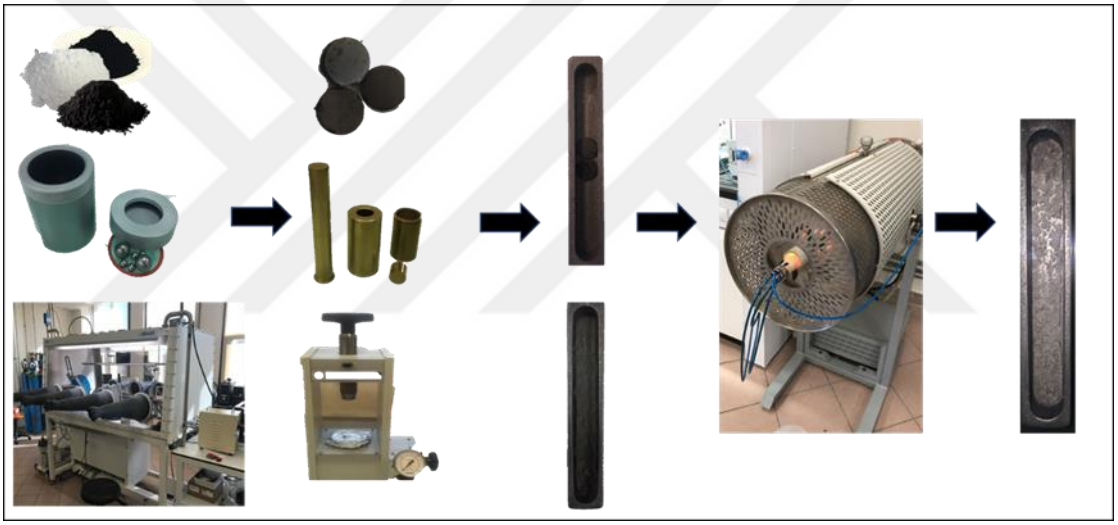

Figure 4.1 Schematic representation of synthesis pathway by using graphite crucible.

Zirconia powder (ZrO_2, Alfa Aesar, 1 µm, 99.5% metals basis), boron oxide powder (B_2O_3, Alfa Aeasar, 99%, metals basis), and activated charcoal powder (C, Sigma Aldrich, pure) were used as starting materials. To obtain pure ZrB_2, reactant powders were weighed stoichiometrically under Ar atmosphere in MBraun glovebox and placed in stainless steel vials. Glovebox operates at <0.1 ppm O_2 and H_2O levels with high purity argon gas flow. Yuan et al., [53] reported that increase in milling time to some extent decreases the crystallite size for synthesis of ZrB_2. For fine mixing and grinding of starting powders as well as to ensure a mechanical activation, 3 hours of ball milling was operated by using SPEX800D at 1450rpm. Powder-to-weight ratio often varies between 1:4- 1:10 in this work regarding to starting weight of powders to obtain desired amount of final product for characterisation techniques. Hardened steel balls with weighed

powder were put in hardened steel vial under Ar and milled continuously. For the first set of experiments, half amount milled powders were pressed into pellet form with a 10 mm diameter stainless steel die under 8 tons load. By using sandwich method (stacking a layer of pellets between powder), powder and pellets were put in alumina crucible. Finally, crucibles were placed into tubular furnace and heated to 1450 ˚C by 8 ˚C/min rate and kept for 6 hours under Ar flow (0.2L/min). The XRD patterns of the samples were obtained by X-ray diffractometer (XRD, Rigaku Mini Flex 600; Cu Kα (λ= 1.5418 Å)). X-ray diffraction spectra were recorded in the 2θ range of 20° to 90°.

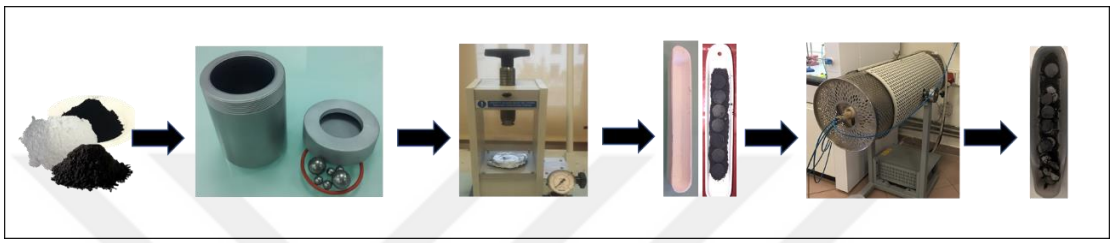

Figure 4.2 A schematic representation of synthesis of transition metal diborides with alumina crucible.

A successful synthesis has been carried out in terms of obtaining the target phase, ZrB_2. Even though the whole reaction procedure was taking place under protective environment, oxide impurity (ZrO_2) formation observed in the final product. A dark grey colour was observed for pure ZrB_2 powder, as can be seen on Figure 4.2 different colour formation refers to impurities in the product. A proper acid leaching would be a solution for disposing ZrO_2 however, some changes in the synthesis condition would provide a more efficient, sustainable method for further experiments such as doping, nanosizing etc. Therefore, changing the sandwich method (BM-16-2,3,6) parameters and increasing carbon from 5 (stoichiometric) to 7 mole to further reduce oxides (BM-16-5), decreasing the amount of pellets from 7 to 3 (BM-16-7), increasing the rate of Ar flow from 0.2 to 0.6L/min and finally, changing the alumina crucible to graphite crucible to avoid oxidation of powder from alumina (BM-16- 8,9,9b) were tried to optimize the synthesis conditions for pure ZrB_2. In Figure 4.3 increasing Ar flow to 0.6L/min decreased the ratio of intensity of oxide peaks. As can be seen on XRD Figure 4.4, graphite crucible utilization enhances the reaction yield. For 16-8 sample, pellet/powder were put together in graphite crucible, turns out making pellet was increasing oxide content by condensing powders and inhibit reduction. For the 16-9 and 9b samples, changed parameter is the amount of initial powder loaded before annealing, the optimum weight was found to be between 0.5-0.8g depending on the materials molecular weight, can be described as a thin

layer covering of the internal surface of the graphite crucible. Figure 4.4 shows the XRD data for all above-mentioned samples. The theoretical diffraction pattern of pure ZrB_2 (International Centre for Diffraction Data (ICDD), PDF -4+ 2011 RDB, Card No: 1510857). ZrO_2 is marked by • in all XRD figures (ICDD code: 9005833).

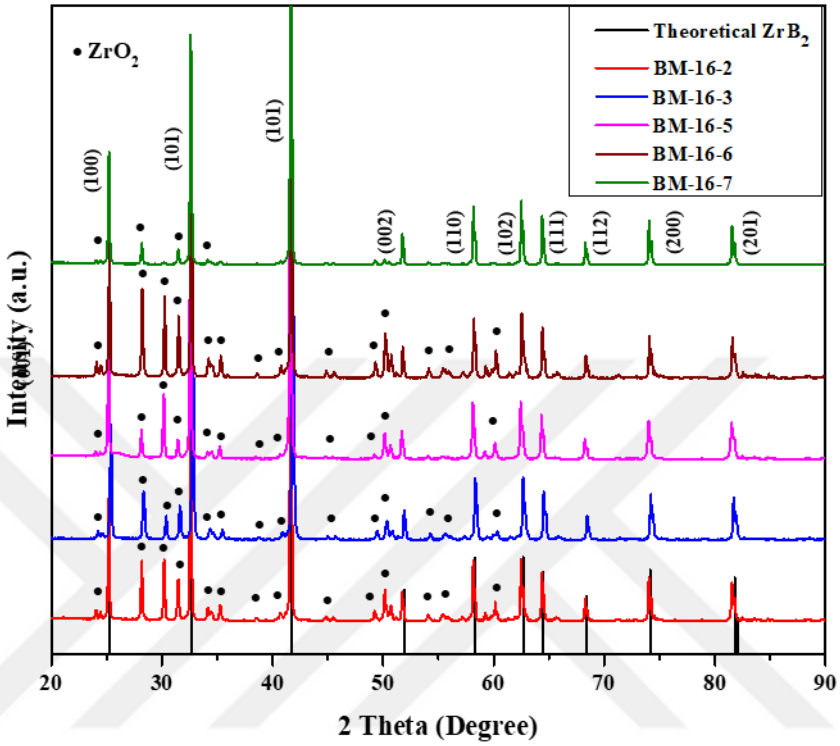

Figure 4.3 XRD data of pure ZrB_2 samples synthesized by alumina crucible.

Graphite crucible itself promotes the reduction of oxide reactants with activated charcoal powder. Since the material have shown almost zero background with highly crystalline peaks, intensity ratio between oxide and diboride may give us some insight about their overall ratio for the product. In BM 16-8 sample, XRD data (Figure 4.4) was evaluated individually for pellets and powder and clearly powder form of reactants yield higher efficiency after annealing. Therefore, for following experiments with graphite crucible (BM 16-9a,9b) only powder form of reactants was placed. Additionally, by using 5 ml, 0.5M H_2SO_4 solution, 0.295 gr of product (pellet part) was leached to eliminate oxide impurities. After DI and absolute ethanol washing, powder was kept under vacuum at 85˚C for drying. Probably, the molarity of the acid solution was not strong enough to remove ZrO_2. For the samples of 16-9a,9b since the oxides were stuck in the pellets, only powder form was placed in graphite. 1,5g of reactant(16-9a) and 0,52g (16-9b) was put

in the crucible and finally almost pure (0.76% ZrO_2 according to the RIR method) ZrB_2 was achieved.

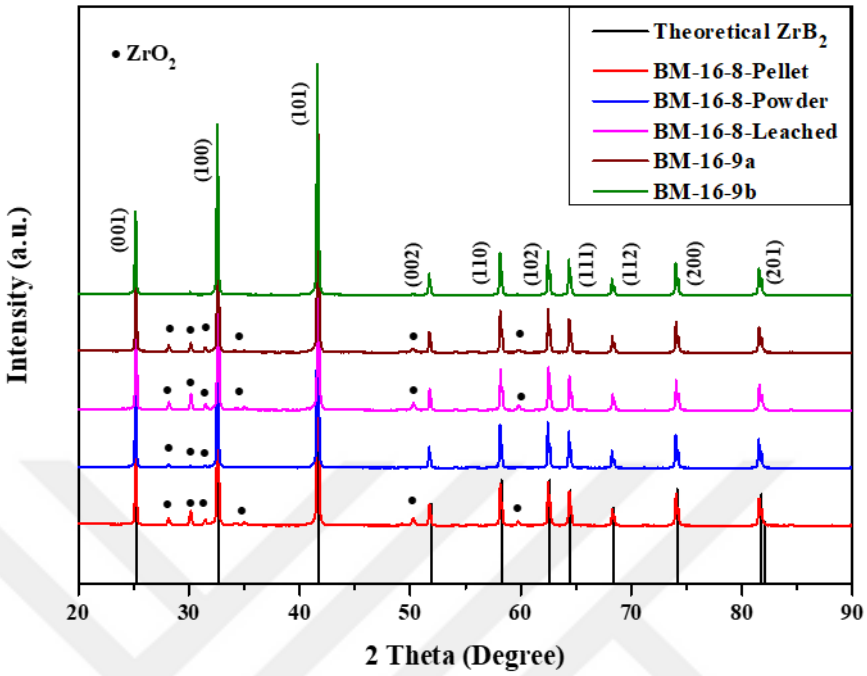

Figure 4.4 XRD data of pure ZrB_2 samples synthesized by graphite crucible.

Transition metal diborides although considered as promising cost-friendly alternatives for noble electrocatalysts, their activity should be enhanced with some strategies that were covered on Chapter 2. Apart from downsizing, priorly the chosen method to improve their intrinsic activity is alloying with other high-activity transition metals such as Ni,Co,Fe in this study. For the substitution experiments given in Equation 12 (x = 0.025- 0.3), reduced fine powder of iron (Fe, ≥ 99%, Sigma-Aldrich), cobalt powder (Co, 99.99%; Sigma Aldrich, trace metals basis), and nickel powder (Ni, 99.99%, Sigma Aldrich, trace metals basis) were used individually.

$$(1\text{-}x)\ ZrO_{2(s)} + xTM_{(s)} + B_2O_{3(s)} + (5\text{-}2x)C_{(s)} \rightarrow Zr_{(1-x)}TM_xB_{2(s)} + (5\text{-}2x)CO_{(g)} \qquad (12)$$

Hafnium oxide powder (HfO_2, Sigma Aldrich, 98%), boron oxide powder (B_2O_3, Alfa Aeasar, 99%), and activated charcoal powder (C, Sigma Aldrich, pure) were used as reactants to synthesize unsubstituted/substituted-HfB_2 by the carbothermal reduction method. Stoichiometric amounts of starting materials for the synthesis of unsubstituted HfB_2 were weighed under protective Ar environment (MBraun Labmaster Pro DP glovebox, O_2 and H_2O level < 0.1 ppm) regarding to the theoretical reduction reaction

given in Equation 15, followed by the reaction equation of transition metal (Ni and Co) substituted-HfB_2 in Equation 16.

$$HfO_{2(s)} + B_2O_{3(s)} + 5C_{(s)} \rightarrow HfB_{2(s)} + 5CO_{(g)} \quad (15)$$

$$(1\text{-}x)\ HfO_{2(s)} + x\ TM_{(s)} + B_2O_{3(s)} + (5\text{-}2x)C_{(s)} \rightarrow Hf_{(1\text{-}x)}TM_xB_{2(s)} + (5\text{-}2x)CO_{(g)} \quad (16)$$

For the substitution experiments given in Equation 2 (x = 0.1, 0.2 and 0.3), cobalt powder (Co, 99.99%; Sigma Aldrich, trace metals basis), and nickel powder (Ni, 99.99%, Sigma Aldrich, trace metals basis) were used individually. Synthesis parameters including methods, temperature profile, equipment etc. were employed completely the same as ZrB_2 study.

4.2 Electrochemical Measurement Method

Electrochemical measurements of the prepared electrocatalysts were conducted on a VersaSTAT Potentiostat Galvanostat using a three-electrode cell equipped with standard Reversible Hydrogen Electrode (RHE; HydroFlex) as reference electrode and Pt wire as a counter electrode. All electrochemical measurements were evaluated under a 1 M KOH solution at room temperature. The working electrodes were made on a glassy carbon electrode with a diameter of 3 mm. Before each experiment, the glassy carbon electrode was polished using diamond suspension (MetPrep, 1 micron) and ultrasonically cleaned by distilled water and ethanol each for 10 min.

Catalysts inks were prepared by ultrasonic dispersing of 2 mg of powder in a mixture of pure ethanol (380 µL) and deionized (DI) water (100 µL) for 30 minutes. Then, 5% Nafion solution (20 µL) was added to the mentioned mixture and ultrasonicated for another 20 minutes to form a homogeneous catalyst slurry. 10 µL of the catalyst ink was drop-cast onto the clean glassy carbon surface. Finally, the catalyst-coated surface of the glassy carbon electrode was dried under air at 80 °C for 120 minutes. The same procedure was followed to fabricate the 10% Pt/C and RuO_2 electrodes. In all electrodes, the catalyst loading was kept at ~0.5 mg/cm^2.

The linear sweep voltammetry (LSV) measurements were carried out at a sweep rate of 5 mV.s^{-1} to attain polarization curves for both OER and HER. LSV measurements were recorded from 0 to +1.8 V towards OER and 0 to -1.6 V towards HER. Determination of overpotential was performed at 10 mA cm^{-2} as the index of HER and OER performance. The cycling behavior of the catalysts was tested for both HER and OER by recording

cyclic voltammetry (CV) for 1000 cycles at a scan rate of 100 mV s^{-1}. The LSV towards HER and OER were recorded before and after 1000 cycles at a scan rate of 5 mV s^{-1}. The long-term electrode stabilities were tested by chronopotentiometry at 10 mA cm^{-2} for 12 and 20 h. The electrochemical impedance spectroscopy (EIS) was performed at the frequency range between 100 kHz and 0.1 Hz with a 10 mV rms sinusoidal modulation at 0 V.

To estimate the electroactive surface area, the double-layer capacitance parameter (C_{dl}) was determined from CV within the potential range where there is a non-Faradaic current response. This range is normally a 0.1 V potential window located on the open-circuit potential (OCP) of the system. The range of 0.8 to 0.9 V was selected based on the OCP of electrodes (0.85 V). CV experiments were performed in unstirred solution by sweeping the potential throughout the non-Faradaic region from the more positive to negative potential and back at different scan rates of 0.05, 0.1, 0.2, 0.4, and 0.8 V s^{-1}. Prior to the operation of the next sweep, the working electrode was kept at each potential vertex for 10 s.

4.3 Characterization of ZrB_2 and TM-substituted ZrB_2 (TM=Fe, Co, Ni)

4.3.1 Chemical Characterization Results

As a successful route for doping micron sized diborides, one of the above-mentioned transition metals, iron, as in elemental form and its oxide were weighed according to stoichiometry and same synthesis route was applied.

$$0.95ZrO_{2(s)} + 0.05Fe_{(s)} + B_2O_{3(s)} + 4.9C_{(s)} \rightarrow Zr_{0.95}Fe_{0.05}B_{2(s)} + 4.9CO_{(g)} \quad (17)$$

$$0.95ZrO_{2(s)} + 0.025Fe_2O_{3(s)} + B_2O_{3(s)} + 4.975C_{(s)} \rightarrow Zr_{0.95}Fe_{0.05}B_{2(s)} + 4.975CO_{(g)} \quad (18)$$

In accordance with XRD data represented on Figure 4.5, both starting materials displayed almost same diffraction data in terms of purity so, doping studies were carried with elemental form of dopants which stoichiometric tuning is more easily achievable for different amount of substitution throughout the project. Additionally, due to different morphology of particles, elemental iron doped sample showed slightly better electrocatalytic activity on water splitting. However, overall activity could be boosted with higher doping ratios therefore, doping studies were carried until drop in overpotential and potential to reach current density values saturated. Consequently, $Zr_{(1-}$

$_{x)}$ Fe_xB_2 doping with various *x* values (*x*= 0.025, 0.05, 0.75, 0.1 and 0.2) were synthesized. Figure 4.5 shows the XRD data of the Fe-doped ZrB_2 samples in comparison with theoretical diffraction peaks (ICDD PDF -4+ 2011 RDB, No: 1510857) and as-synthesized ZrB_2 (BM-16-9b sample).

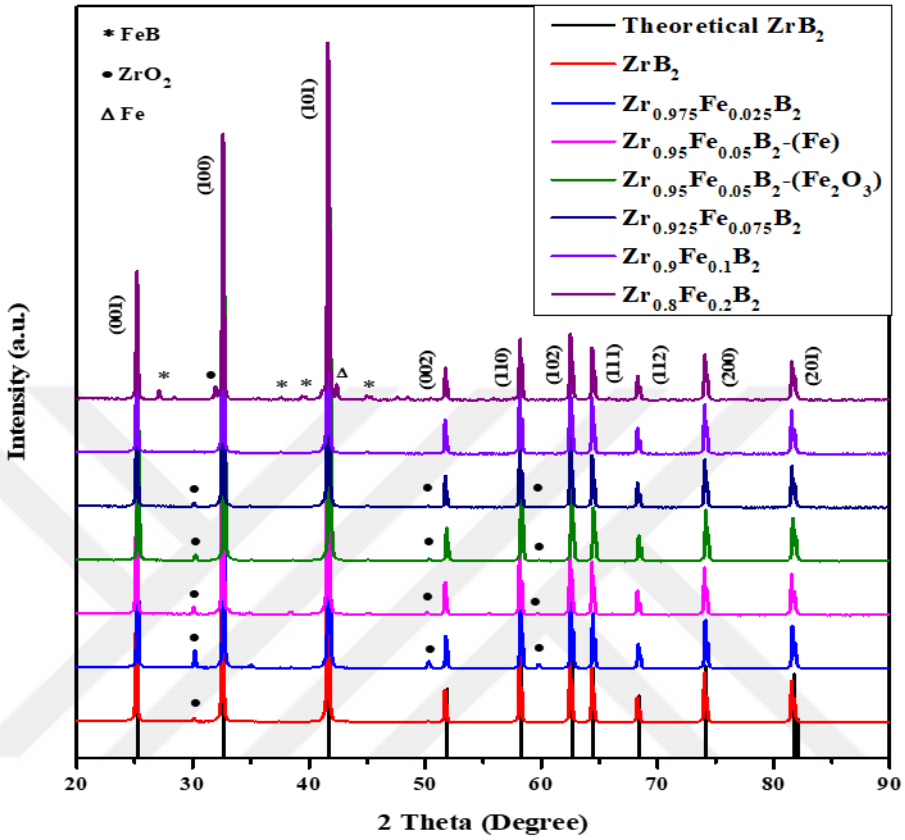

Figure 4.5 XRD patterns of $Zr_{(1-x)}Fe_xB_2$ (*x*= 0.025,0.05,0.075,0.1 and 0.2) samples with unsubstituted ZrB_2 (BM-16-9b).

XRD patterns of Fe-doped ZrB_2 samples have shown that as dopant ratio increases, formation of oxides decreases. By considering the synthesis parameters are the same for doped samples (including other dopant transition metals such as Ni, Co, Cu) same trend was observed for all experiments. In addition, for *x*=0.2, elemental Fe and Fe-B compounds were formed, indicating that substitution of Fe into Zr might have reached its saturated point.

Nickel substitution in ZrB_2 was carried successfully according to XRD data. Intrinsic amount of ZrO_2 formation was observed only for *x*= 0.05. There was no trace of secondary phase formation for higher ratios of nickel. The most successful substitution among three transition metals, was achieved with nickel into diboride. Increasing the amount to *x*=0.3, leads to the formation of secondary phases of Ni-B. Therefore, it can be assumed that when *x*=0.2 saturation limit is achieved.

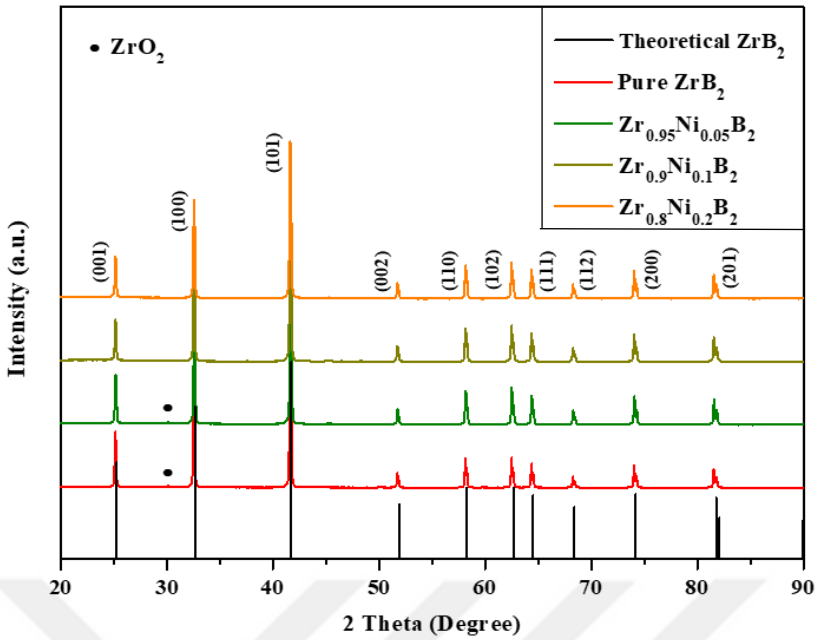

Figure 4.6 XRD patterns of $Zr_{(1-x)}Ni_xB_2$ (x= 00.05,0.1 and 0.2) samples.

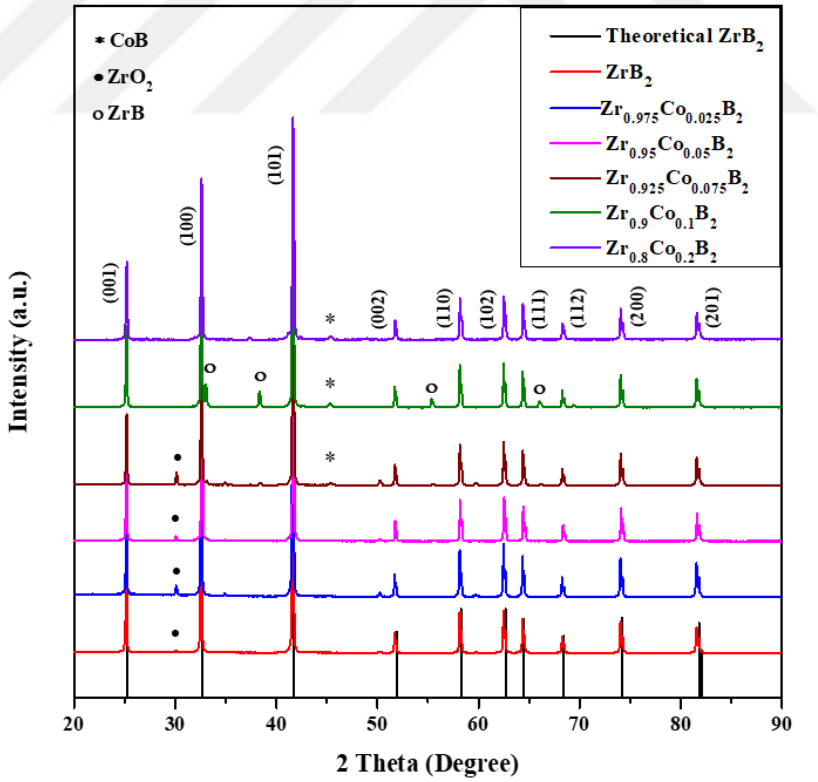

Figure 4.7 XRD patterns of $Zr_{(1-x)}Co_xB_2$ (x= 0.025,0.05,0.075,0.1 and 0.2) samples.

Addition of Co into ZrB_2 decreased the oxide content in the final powder even more than Fe substitution at the first place. As *x* value increases CoB phase (marked by *) was started to form indicating a full substitution has almost reached up to its maximum stage.

To characterize the surface morphology and chemical composition, Zeiss Ultra Plus Field Emission Scanning Electron Microscopy (FESEM) was used at an accelerating voltage of 5 kV for Energy Dispersive X-ray Spectroscopy (EDS). The transmission electron microscope (TEM) images have been taken using a Hitachi HT7700 TEM instrument operating with a maximum acceleration voltage of 120 kV.

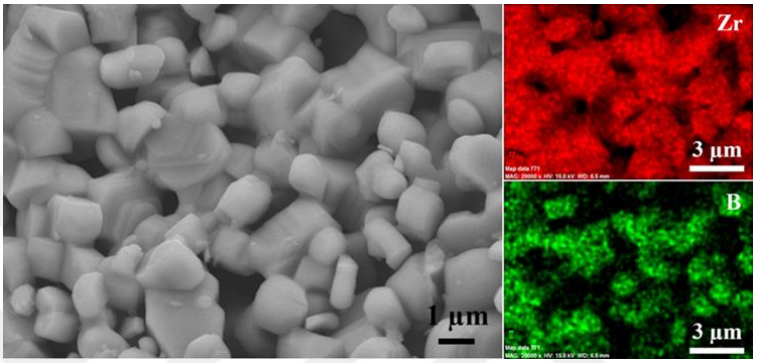

Figure 4.8 Characterization of ZrB_2. Low magnification SEM, along with related EDS elemental mapping on the right side. Voids in SEM image can be detected as dark spots in EDS mapping.

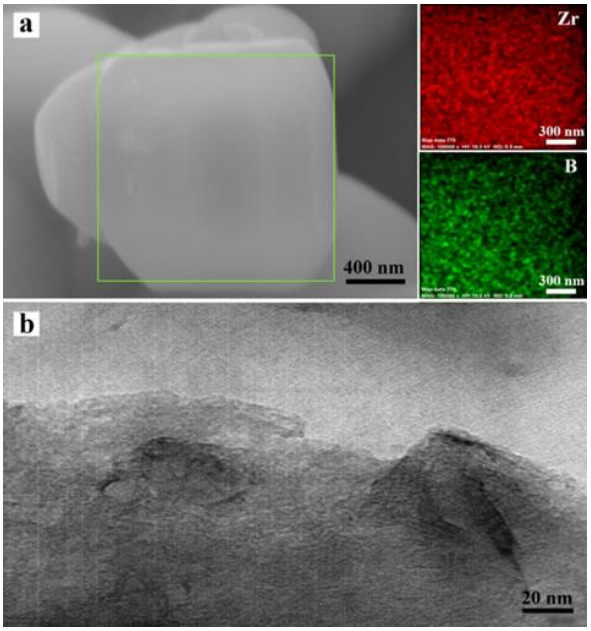

Figure 4.9 Characterization of ZrB_2. a) High magnification SEM, b) TEM, along with related EDS elemental mapping on the right side.

TEM, EDS and SEM micrographs of ZrB_2—synthesized using ZrO_2, B_2O_3, and carbon—presented in Figure 4.8-4.9. The SEM images display the nearly spherical shape of the pure powders obtained at 1450 ºC. ZrB_2 features a hexagonal crystal structure with anisotropic nature (a = 3.17 Å and c = 3.53 Å)[45]. According to these microstructure images, the size of particles for unsubstituted samples are either in the range of 1-2 micrometer or submicrometer.

To further broaden our knowledge on substituted samples, SEM was conducted on Fe-, Co-, and Ni- substituted samples. Observation of images indicates that increasing the dopant amount leads to a reduction in the agglomeration of particles (Figure 4.10). This trend maintains nearly the same for all substituted samples. It can be concluded that with an increase in the amount of transition metal incorporation into the structure, the spherical shape of particles does not undergo a considerable transformation, but it prevents agglomeration.

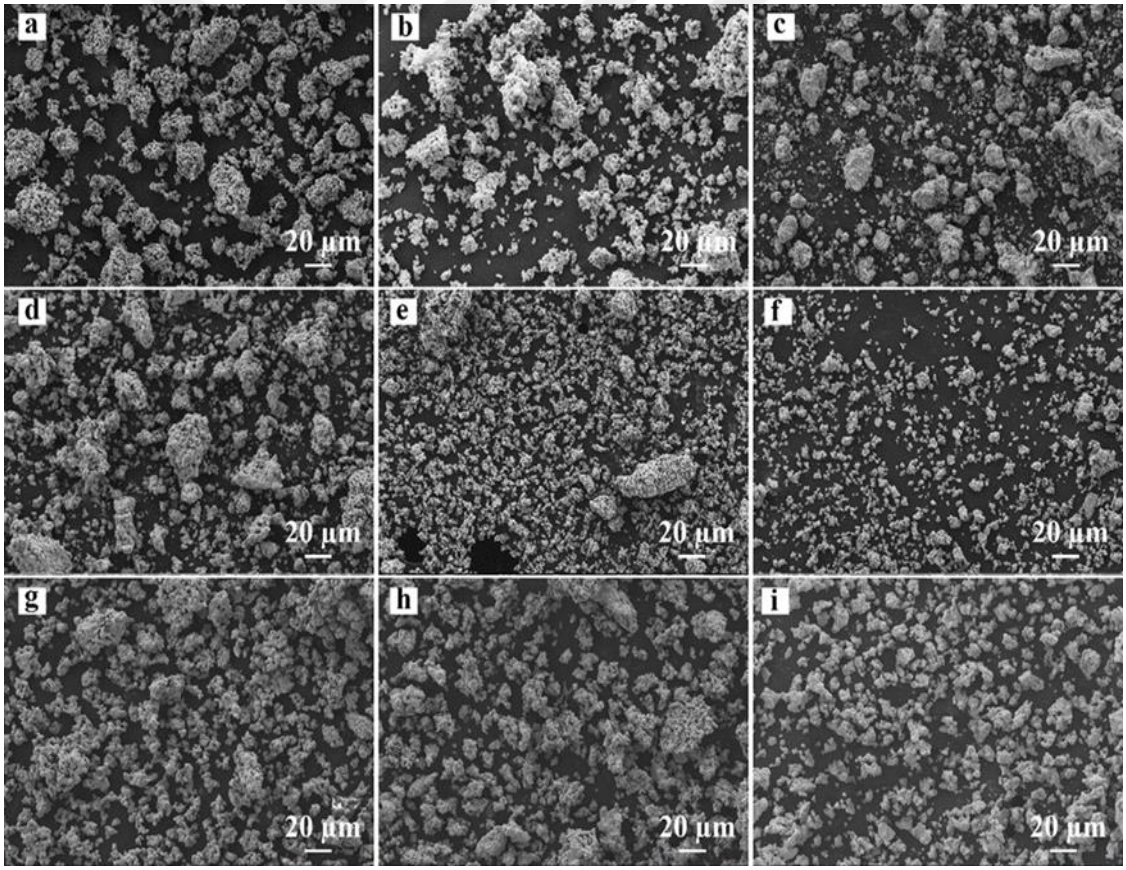

Figure 4.10 SEM images of a) $Zr_{0.95}Fe_{0.05}B_2$, b) $Zr_{0.9}Fe_{0.1}B_2$, c) $Zr_{0.8}Fe_{0.2}B_2$, d) $Zr_{0.95}Co_{0.05}B_2$, e) $Zr_{0.9}Co_{0.1}B_2$, f) $Zr_{0.8}Co_{0.2}B_2$, g) $Zr_{0.95}Ni_{0.05}B_2$, h) $Zr_{0.9}Ni_{0.1}B_2$, and l) $Zr_{0.8}Ni_{0.2}B_2$; showing agglomeration reduction by increasing substitution concentration.

Increasing the substitution concentration from *x*= 0.05 to 0.2 is the primary reason for improving catalytic performance. Increasing the portion of transition metal in the structure alters electronic configuration and intensifies available surface-active sites. It should be highlighted that heteroatom substitution dwindles agglomeration and enlarges specific surface area (SSA) [2]. It is also interesting to mention that the morphology of all samples is composed of particle chains that are uniformly distributed all over the entire sample.

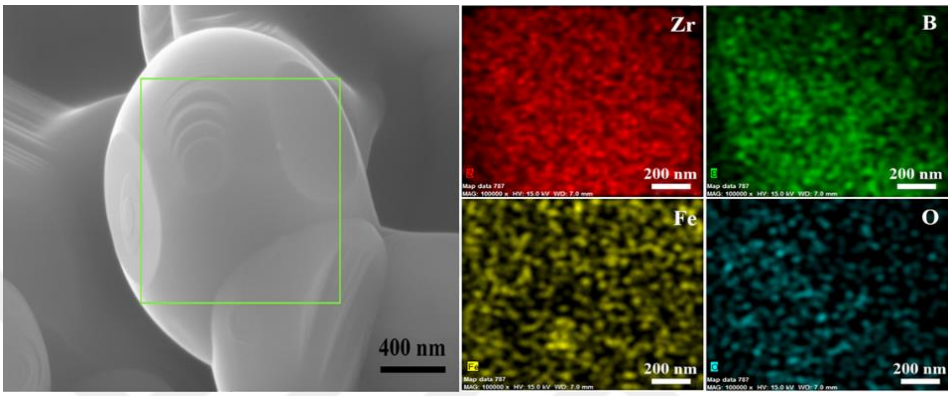

Figure 4.11 High magnification SEM image of $Zr_{0.8}Fe_{0.2}B_2$ along with EDS elemental mapping on the right side.

SEM images in high magnifications are presented in Figures 4.12a and c for both $Zr_{0.8}Co_{0.2}B_2$ and $Zr_{0.8}Ni_{0.2}B_2$ samples, showing their microstructures. Meanwhile, the TEM images have been included in Figures 4.12b and d for the mentioned samples. The EDS elemental mapping of substituted samples can be seen on the right side, clearly showing the homogeneous distribution of the elements in their grains. It is noteworthy to highlight that both catalysts contain oxygen on the surface that can be attributed to surface oxidation. TEM analysis indicates some nano-sized sub-grains (<5 nm) for $Zr_{0.8}Ni_{0.2}B_2$, whereas no special features for $Zr_{0.8}Co_{0.2}B_2$ in the measured scale. The selected area electron diffraction pattern (SAED) was recorded for $Zr_{0.8}Co_{0.2}B_2$ along the [-225] zone axis and the diffraction spots could be well indexed with the reported hexagonal crystal structure of ZrB_2. Overall, powder XRD and SAED confirm the successful growth of Co-substituted ZrB_2 crystals.

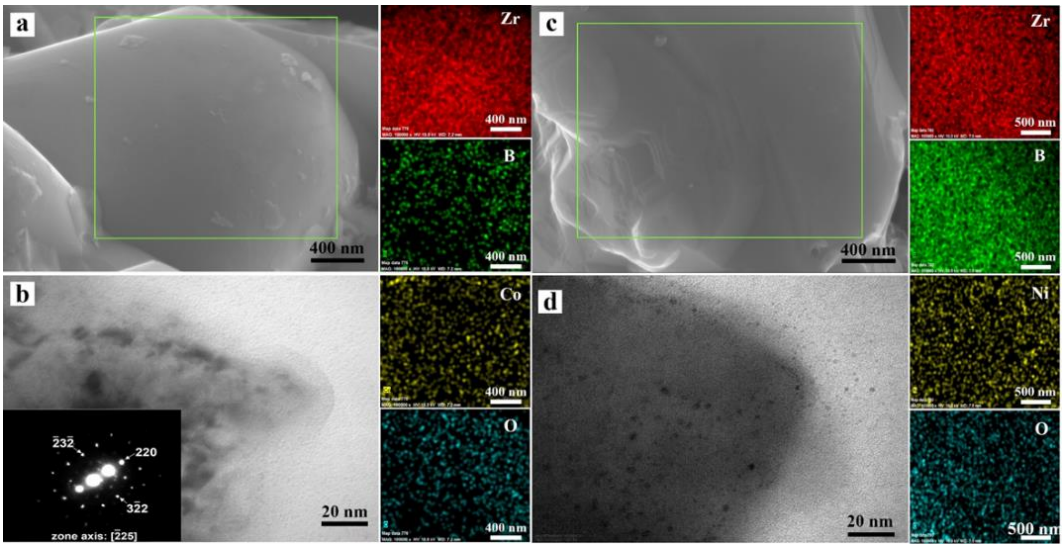

Figure 4.12 Characterization of metal-substituted ZrB_2. a) High magnification SEM image of $Zr_{0.8}Co_{0.2}B_2$, b) TEM of $Zr_{0.8}Co_{0.2}B_2$ (inset: SAED pattern), c) High magnification SEM image of $Zr_{0.8}Ni_{0.2}B_2$, and d) TEM of $Zr_{0.8}Ni_{0.2}B_2$, along with related EDS elemental mapping on the right side.

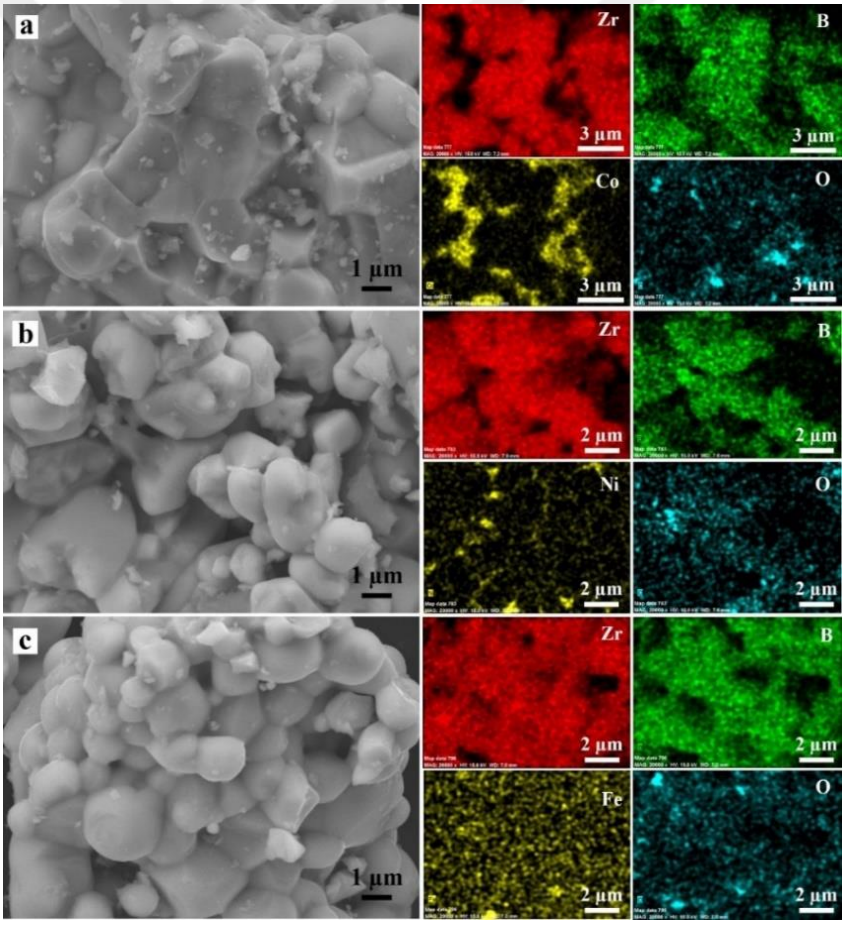

Figure 4.13 Characterization of metal-substituted ZrB_2. a) Low magnification SEM image of $Zr_{0.8}Co_{0.2}B_2$, b) Low magnification SEM image of $Zr_{0.8}Ni_{0.2}B_2$, and c) Low magnification SEM image of $Zr_{0.8}Fe_{0.2}B_2$, along with related EDS elemental mapping on the right side.

X-ray photoelectron spectroscopy (XPS) was conducted to inspect the chemical features of the metals and dopants in the as prepared electrocatalysts. Figure 4.14 shows XPS studies of ZrB_2, Co-, Ni- as well as Fe-substituted ZrB_2 powders. For this, Zr 3d, B 1s, Co 2p, Ni 2p, and Fe 2p spectra have been analyzed. Besides, O 1s spectra have also been considered, explaining the trace amount of surface oxides. The XPS Zr 3d and B 1s spectra of sample surfaces of Co-, Ni- and Fe-substituted ZrB_2 ($Zr_{0.8}Co_{0.2}B_2$, $Zr_{0.8}Ni_{0.2}B_2$, and $Zr_{0.8}Fe_{0.2}B_2$) are presented, separately.

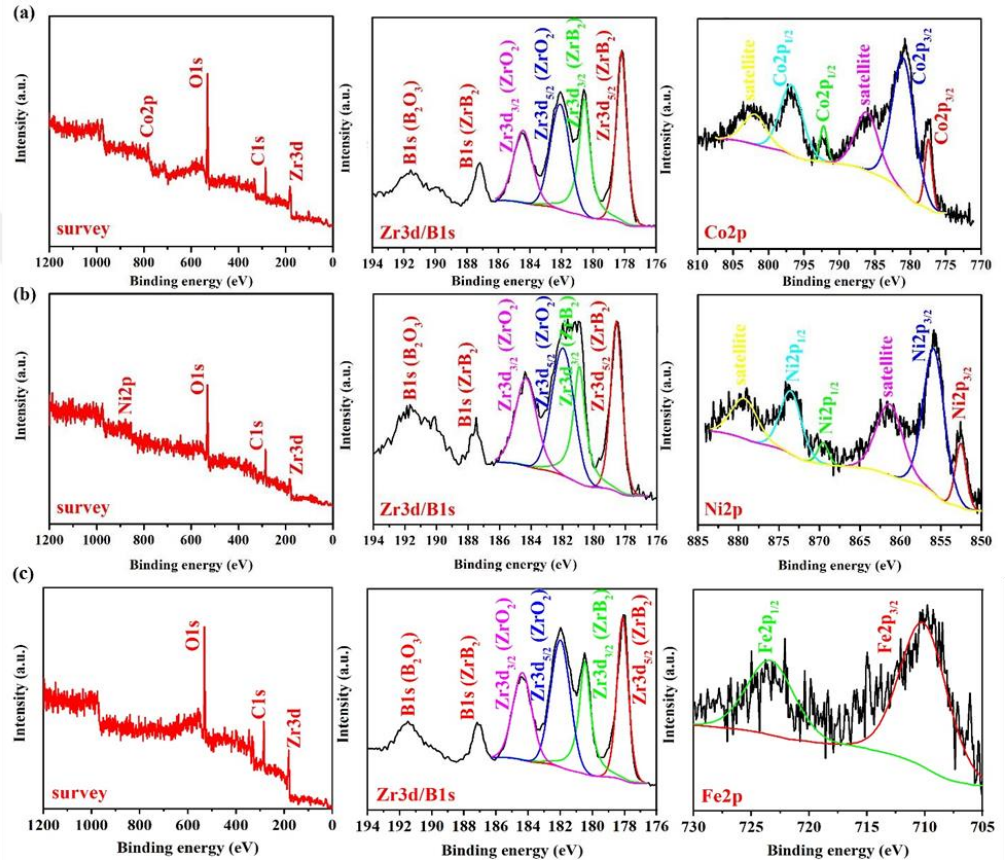

Figure 4.14 XPS spectra of a) $Zr_{0.8}Co_{0.2}B_2$, b) $Zr_{0.8}Ni_{0.2}B_2$ and c) $Zr_{0.8}Fe_{0.2}B_2$

The findings reflect the presence of two double-peak indexed to Zr $3d_{5/2}$-$3d_{3/2}$, and two single-peak related to B 1s for all samples, indicating the two distinctive chemical states for the Zr and B atoms. Here, both Co and Ni containing samples display Zr $3d_{5/2}$, Zr $3d_{3/2}$, and B 1s peaks positioned at respective binding energies of ~178.4, 180.5, and 187.2 eV, representing the chemical state related to ZrB_2 [54]. Other emerging peaks at relatively higher binding energies of ~182.2, 184.8, and 192 eV correspond to $3d_{5/2}$, Zr $3d_{3/2}$, and B 1s, respectively, representative of ZrO_2 and B_2O_3 [54]. The presence of surface oxides can also be evidenced with respect to the emergence of O 1s peaks at 531.5 eV, as shown in the survey pattern of Figure 4.14. Thus, the XPS results substantiate that

ZrO_2 and B_2O_3 can be found on the surface of both samples. Knowing that XPS is a surface analysis technique, it can be noticed that based on these findings there are partially oxidized species on the surface [54]. Not to mention that the development of OER is subject to the in-situ formation of surface oxides/ hydroxides that alleviate the kinetic barrier [6].

The deconvolution and curve-fitting were carried out for Co 2p. The spectrum shown in Figure 4.14a revealed two spin−orbit doublets: including 798 eV (Co $2p_{1/2}$) and 782 eV (Co $2p_{3/2}$) correlated with Co^{2+} (CoO) [55] as well as 793 eV (Co $2p_{1/2}$) and 778 eV (Co $2p_{3/2}$) corresponding to Co^0 [56]. Moreover, there are two extra peaks at 782 and 802 eV which are attributed to satellite peaks [57]–[60].

For the Ni 2p spectrum (Figure 4.14b), the binding energies located at 874.1 eV for Ni $2p_{1/2}$ and 856.2 eV for Ni $2p_{3/2}$ can be ascribed to NiB [61]. Also, the binding energies positioned at 869.4 eV for Ni $2p_{1/2}$ and 853.2 eV for Ni $2p_{3/2}$ can be appertained to Ni^0 [62]. Finally, the peaks observed at 862 and 879 eV pertain to the satellite peaks [59]. For the Fe 2p spectrum (Figure 4.14c), peaks detected at 723.1 eV for Fe $2p_{1/2}$ and 710.2 eV for Fe $2p_{3/2}$ belong to the oxidized Fe species [63].

XPS results of ZrB_2 with various loadings of transition metals (Co, Ni, and Fe) are also depicted in Figure 4.15. It should be noted that metal substituting shifts Zr 3d towards higher binding energies; particularly, in the higher metal portions (x = 0.2) this trend is even more noticeable. In other words, there is a difference of ~ 1 eV between the binding energies of substituted (x = 0.2) and unsubstituted ZrB_2. Finally, Co 2p, Ni 2p, and Fe 2p peaks were detected in all substituted samples, confirming the presence of Co, Ni, and Fe-containing species in the ZrB_2 structure.

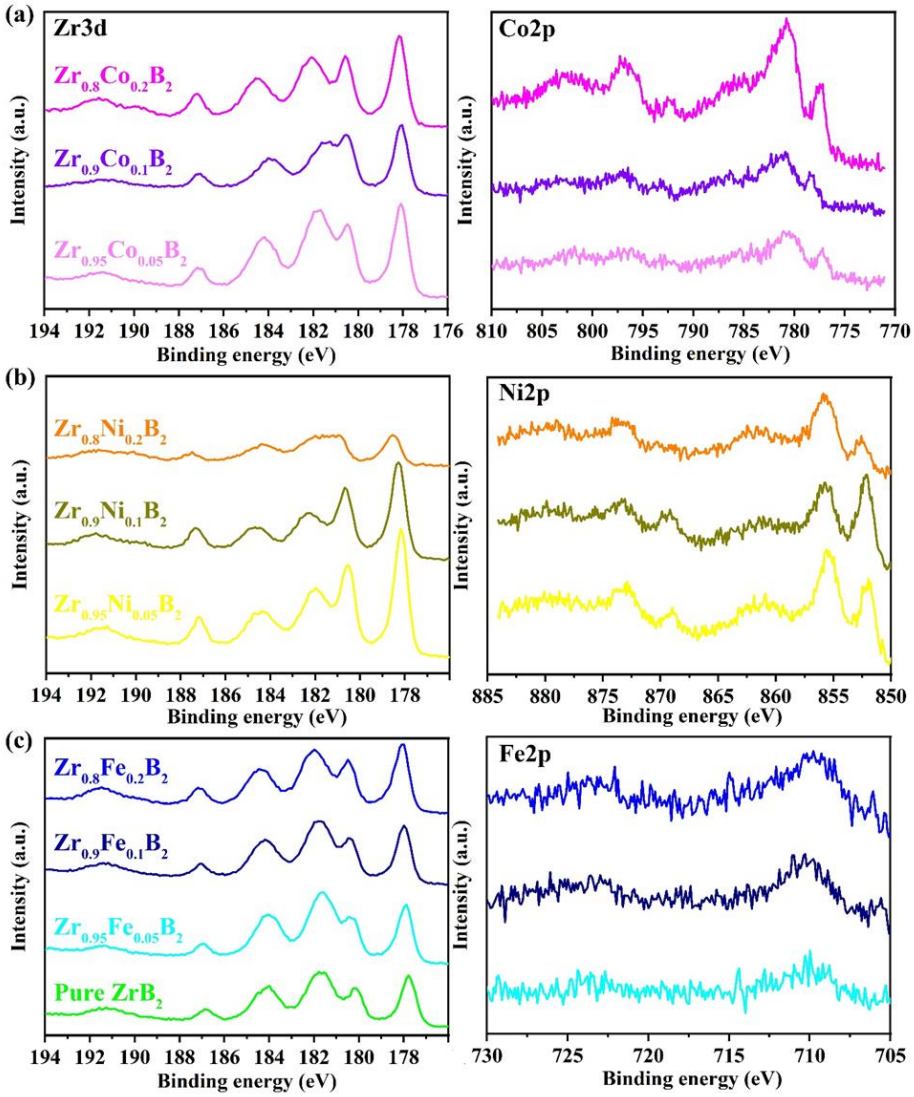

Figure 4.15 Zr 3d and dopant 2p XPS spectra for the a) Co-substituted ZrB_2, b) Ni-substituted ZrB_2, and c) Fe-substituted ZrB_2 and unsubstituted ZrB_2.

The electrical conductivity of the ZrB_2 sample was analyzed to assess its prospects in electrocatalysis. To perform electrical conductivity measurement, the as-synthesized powder was compacted into a pellet using a spark plasma sintering (SPS) device. By considering the volume calculations to obtain desired density (> 95%); filling 10 mm diameter graphite die with 0.95 g of ZrB_2 powder results in up to 2 mm height of the pellet depending on the achieved relative density. 50 MPa pressure was applied, and powder was heated from 600 to 1500 ˚C over 18 minutes under vacuum. Displacement peaks started at around 1300 ˚C. Afterwards, powder was heated to 1850 ˚C with the rate of 100 ˚C/min. The temperature and pressure were kept at the mentioned values for 10 minutes according to literature data [64]. Achieved relative density for ZrB_2 powder after SPS (spark plasma sintering) without any sintering-aid employed, was found as > %96

which is suitable for electrical conductivity characterization [65]. Subsequently, pellet was cut into rectangular prism shape by diamond wire saw. After fine polishing was applied, material was placed into ULVAC ZEM3 electrical resistivity & Seebeck coefficient measurement system. Electrical conductivity of as-synthesized ZrB_2 was found to be 7.1×10^6 S/m at 50˚C and 6.3 S/m at 100˚C signifying metallic behaviour. The Seebeck coefficients for the same temperatures were found as -0.18 and -1.06 µV/K, respectively, which are very low as expected for metallic materials.

4.3.2 Hydrogen Evolution Activities of ZrB_2 Samples

SEM analysis was also conducted on the electrode surface, the same amount used for each electrode fabrication was injected on a graphite sheet with a diameter of 3 mm. As seen in Figure 4.16a, the injected ink onto the graphite sheet seems to have a uniform distribution of catalytic material in the Nafion solution. Also, it is shown in Figure 4.16b that the spherical particles have been covered by a thin layer of Nafion solution.

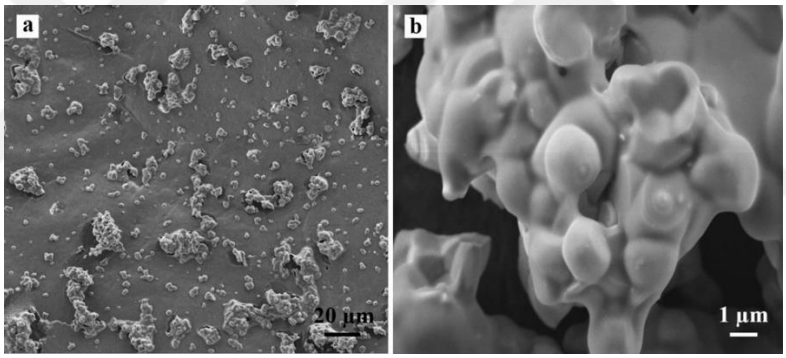

Figure 4.16 SEM images of the working electrode surface

The electrochemical performance of the ZrB_2 powders towards the HER was evaluated using glassy carbon working electrodes (with 0.5 mg cm^{-2} catalyst powder on it) under 1 M KOH medium. Figure 4.17 reveals the LSV polarization curves for unsubstituted and substituted ZrB_2 electrodes. To compare, the HER activity of commercial 10% Pt/C catalyst was also evaluated and included. Pt/C as a state-of-the-art HER catalyst shows a low overpotential of 198 mV to obtain the 10 mA cm^{-2} current density requiring for hydrogen evolution. It can be seen from the polarization curves that the glassy carbon has negligible HER activity; therefore, it can be used as an inert substrate for electrocatalytic examinations. The electrochemical measurements showed an overpotential of 700 mV for ZrB_2, which is much higher than the Pt/C. On the contrary, based on the HER polarization curves of substituted ZrB_2, it is evident that ZrB_2 substitution with divalent metals including Fe, Co, and Ni significantly enhances HER

activity. Thus, the obtained overpotentials at 10 mA cm^{-2} current density for substituted ZrB_2 are much lower than that of unsubstituted ZrB_2 (see Figure 7a). In this respect, $Zr_{0.8}Co_{0.2}B_2$ showed the lowest overpotential (420 mV), indicating the best result in terms of the HER performance compared to its counterparts; $Zr_{0.8}Ni_{0.2}B_2$ and $Zr_{0.8}Fe_{0.2}B_2$ with respective overpotentials of 480 and 510 mV. The overpotential value of $Zr_{0.8}Co_{0.2}B_2$ is relatively comparable to the previously reported transition-metal borides such as Co_2B-500 with an overpotential of 328 mV at 10 mA cm^{-2} current density [66]. Besides, the overpotential value of $Zr_{0.8}Co_{0.2}B_2$ represents a two-fold improvement over the parent sample. This finding suggests that HER reaction over $Zr_{0.8}Co_{0.2}B_2$ proceeds in an efficient manner which is in accordance with the literature—in those Co-based borides are favorable catalysts in the water reduction reactions.

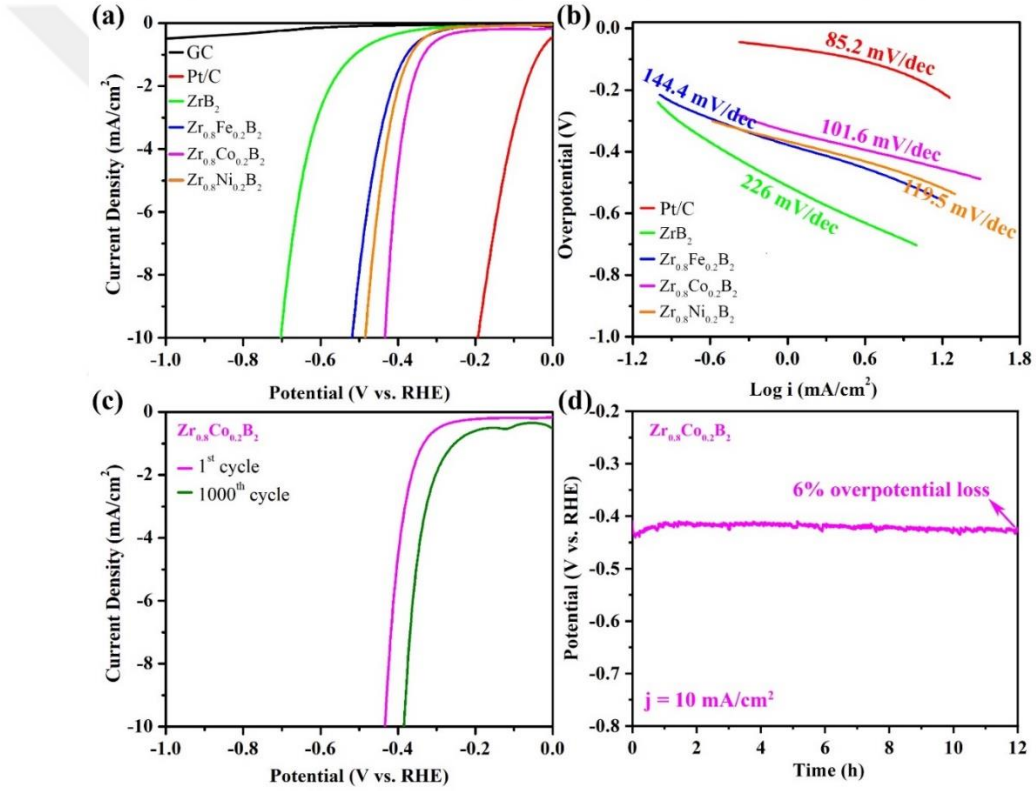

Figure 4.17 Electrochemical performance of unsubstituted and substituted ZrB_2 towards HER recorded at a scan rate of 5 mV s^{-1} in 1 M KOH. a) Polarization curves, b) Related Tafel plots, c) Polarization curves of $Zr_{0.8}Co_{0.2}B_2$ initially and after 1000 CV scans at 100 mV s^{-1} and d) Chronopotentiometric curve of $Zr_{0.8}Co_{0.2}B_2$ recorded at a current density of 10 mA cm^{-2}.

The Tafel slopes of Pt/C, unsubstituted, and substituted ZrB_2 are illustrated in Figure 4.17b. The Tafel slope presents the required overpotential to obtain an increase in the current density magnitude. Also, the Tafel slope is a key index to determine the HER kinetics, providing further insights into the HER mechanism. There are two major steps

for the HER process: the Volmer adsorption and the desorption process. First, hydrogen binds to the catalyst via the Volmer adsorption according to the following reaction:

$H_3O^+ + e^- \rightarrow H_{ads} + H_2O$

The Tafel slope for the preceding reaction is 120 mV dec^{-1}. Followed by the adsorption, the desorption process can take place either by the Heyrovsky reaction or Tafel desorption. The Heyrovsky process can occur based upon the following reaction:

$H_{ads} + e^- + H_3O^+ \rightarrow H_2 + H_2O$

A Tafel slope of 40 mV dec^{-1} corresponds to the foregoing reaction. The alternative desorption process proceeds through Tafel desorption as seen in the reaction below:

$H^{\circ}_{ads} + H^{\circ}_{ads} \rightarrow H_2$

For this reaction, a Tafel slope of 30 mV dec^{-1} was reported [3].

From Figure 4.17b, as expected, Pt/C holds the lowest Tafel slope (85.2 mV dec^{-1}) compared with all synthesized samples. Knowing that the mentioned value falls in the range of 40-120 mV dec^{-1}, we can assume that the reaction takes place through the Volmer-Heyrovsky mechanism. Co-, Ni- and Fe-substituted ZrB_2 electrodes displayed Tafel slopes of 101.6, 119.5, and 144.4 mV dec^{-1}, respectively, manifesting facile kinetics and fast electron transport compared with parent catalyst with Tafel slope of 226 mV dec^{-1}. Based upon the above-written reactions, concerning substituted ZrB_2, it seems that the HER reaction is dominated by the Volmer mechanism.

To compare with any of the known ideal Tafel slopes, smaller slopes are preferred. Based on the literature [67], high Tafel slope values originate from a lack of proton accessibility to the abundant active sites in the electrolyte. The electrochemically active surface area (EASA) was evaluated via the electrochemical double-layer capacitance of the catalytic surface. Double-layer capacitance is measured by using cyclic voltammetry, recorded at multiple scan rates in a non-Faradaic potential region. This region is determined by a potential range in a 0.1 V window centered at the open-circuit potential (OCP)[68].

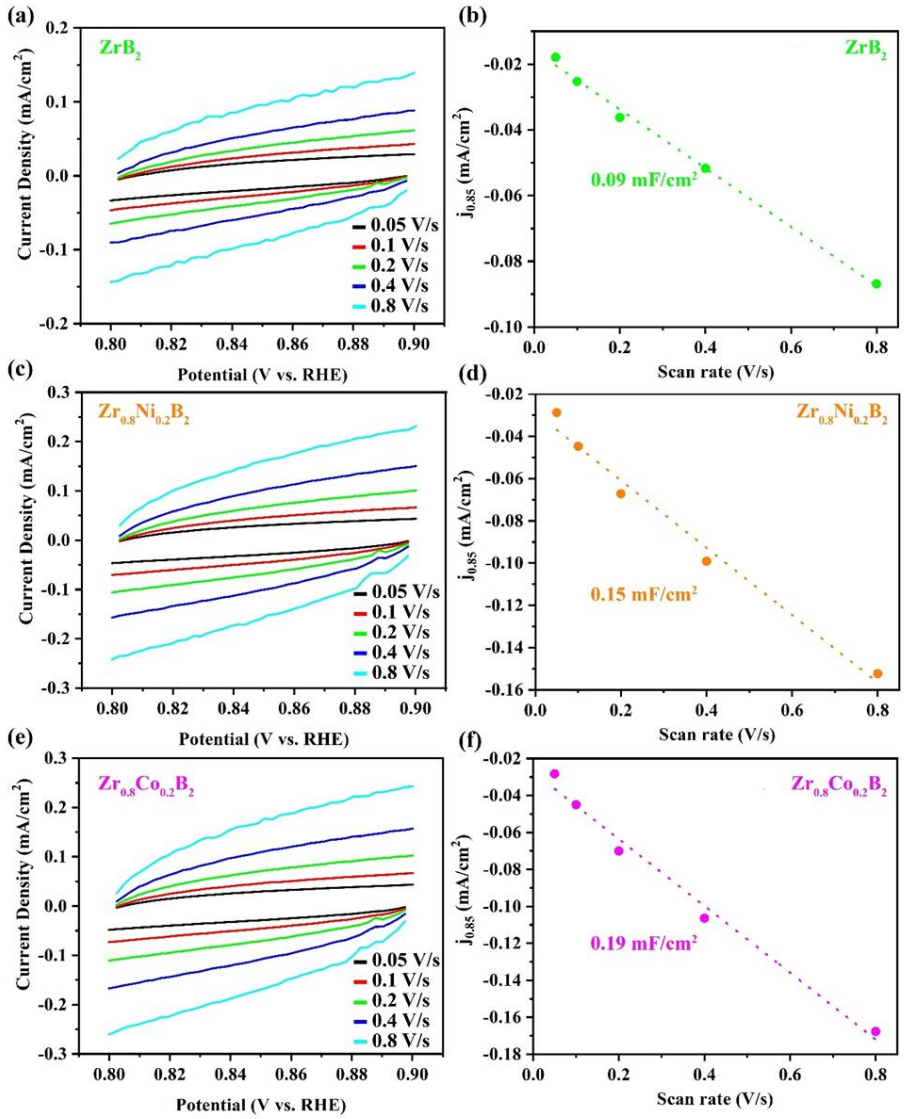

Figure 4.18 a, c, and e) Cyclic voltammograms of ZrB_2, $Zr_{0.8}Ni_{0.2}B_2$, and $Zr_{0.8}Co_{0.2}B_2$, respectively along with their b, d, and f) Respective capacitive current at 0.85 V as a function of the scan rate.

Figure 4.18 shows the CV plots recorded in non-Faradaic potential range at different scan rates. The double-layer capacitance can be calculated by:

$$i_c = \nu C_{dl}$$

where, i_c, ν, and C_{dl} are double layer charging current, scan rate, and double-layer capacitance, separately. From plotting i_c measured at OCP (center of potential window) against ν, C_{dl} can be obtained as slope of the straight line. The EASA is then estimated using the following equation:

$$EASA = C_{dl}/C_s$$

Where C_s is the specific capacitance of the sample. Based on the previous studies [68], the typical value of C_s is equal to 0.040 mF cm^{-2} under 1 M KOH solution.

From Figure 4.18, the $Zr_{0.8}Co_{0.2}B_2$ indicates a C_{dl} value of 0.19 mF cm^{-2} which is twice as high as the value obtained from parent ZrB_2 (0.09 mF cm^{-2}). It can be seen from the figure, metal incorporation could enhance active sites, and thereby improve HER activity on substituted ZrB_2 compared with unsubstituted one. According to the literature review on Chapter 2, expanding the number of active sites enables the exposure of more available catalytic sites to electrolyte ions, which in turn, improves HER activity. The preceding statements are also consistent with the BET results. The N_2-sorption studies on the samples led to BET surface areas of 0.08, 0.41. 0.49. and 0.5 m^2/g pertaining to ZrB_2, Fe-, Co-, and Ni-substituted samples, separately.

The electrocatalytic stability of $Zr_{0.8}Co_{0.2}B_2$ was studied through a CV test up to 1000 cycles within the potential range of 0 and -1 V at 100 mV s^{-1}. Figure 4.17c reveals LSV curves towards HER for $Zr_{0.8}Co_{0.2}B_2$ before and after 1000 cycles of operation. It can be observed that there is a drop from 420 to 380 mV in the overpotential values after 1000 sweeps, which implies a substantial improvement in the HER performance of $Zr_{0.8}Co_{0.2}B_2$. It can be concluded that HER performance and number of CV sweeps are in direct relation, meaning that by increasing the number of CV sweeps HER expresses an improvement thanks to continuous degradation of surface oxide layers and thereby exposure of more active sites [69].

Since catalytic sustainability plays a pivotal role in water splitting applications, the long-term stability of the best-performing catalyst in HER ($Zr_{0.8}Co_{0.2}B_2$) was also assessed at a current density of 10 mA cm^{-2} for 12 h to explore its lifetime throughout hydrogen production (see Figure 4.17d). From the figure, the catalyst maintains a certain potential of about 0.4 V for 12 h during continuous operation with a 6% loss in overpotential, demonstrating superior durability of the $Zr_{0.8}Co_{0.2}B_2$ catalyst under an alkaline solution. Note that $Zr_{0.7}Ni_{0.3}B_2$ and $Zr_{0.7}Co_{0.3}B_2$ were also characterized for HER and OER [70], but due to their inferior performances were not investigated further.

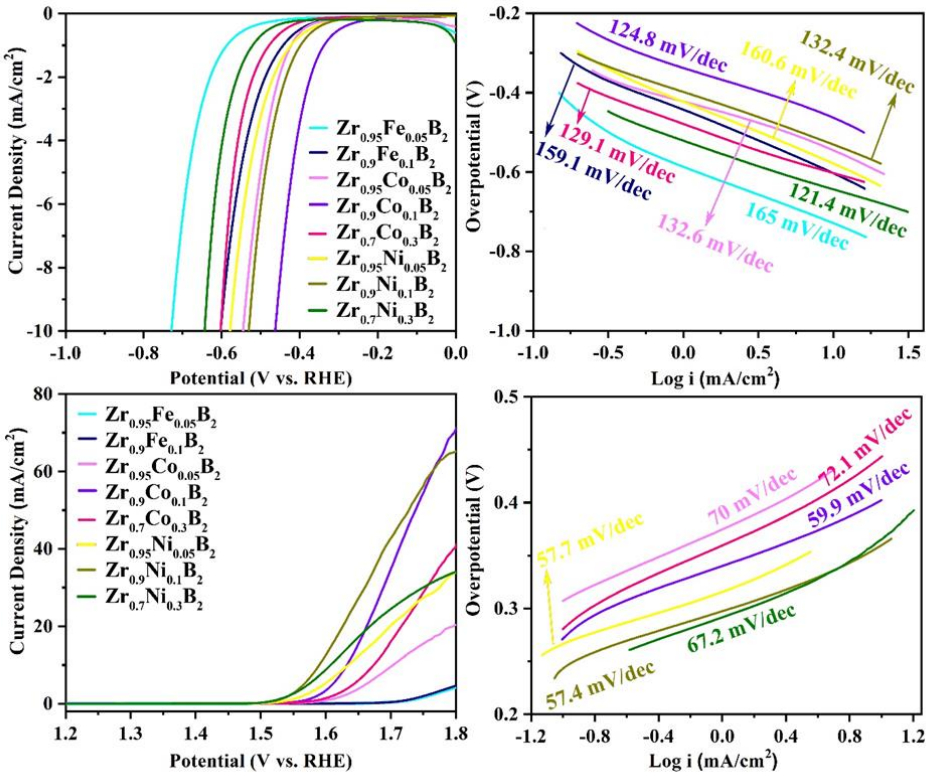

Figure 4.19 Electrochemical performance of substituted ZrB_2 towards HER recorded at a scan rate of 5 mV s^{-1} in 1 M KOH. a) Polarization curves, b) Related Tafel plots, and electrochemical performance of substituted ZrB_2 towards OER recorded at a scan rate of 5 mV s^{-1} in 1 M KOH, c) Polarization curves, d) Related Tafel plots.

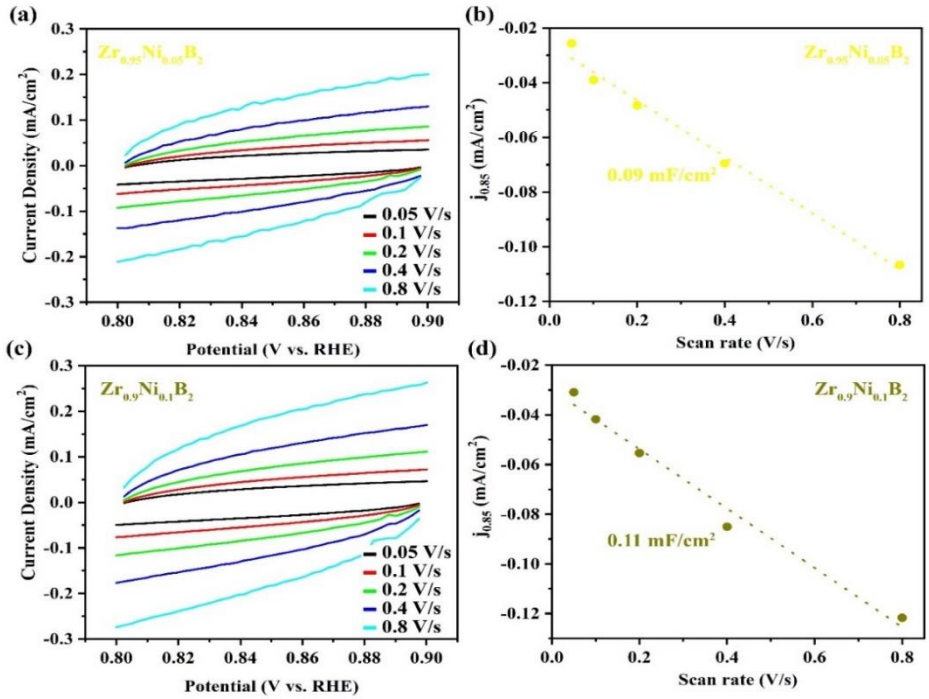

Figure 4.20 a and b) Cyclic voltammograms of $Zr_{0.95}Ni_{0.05}B_2$ and $Zr_{0.9}Ni_{0.1}B_2$, respectively along with their c and d) Respective capacitive current at 0.85 V as a function of the scan rate.

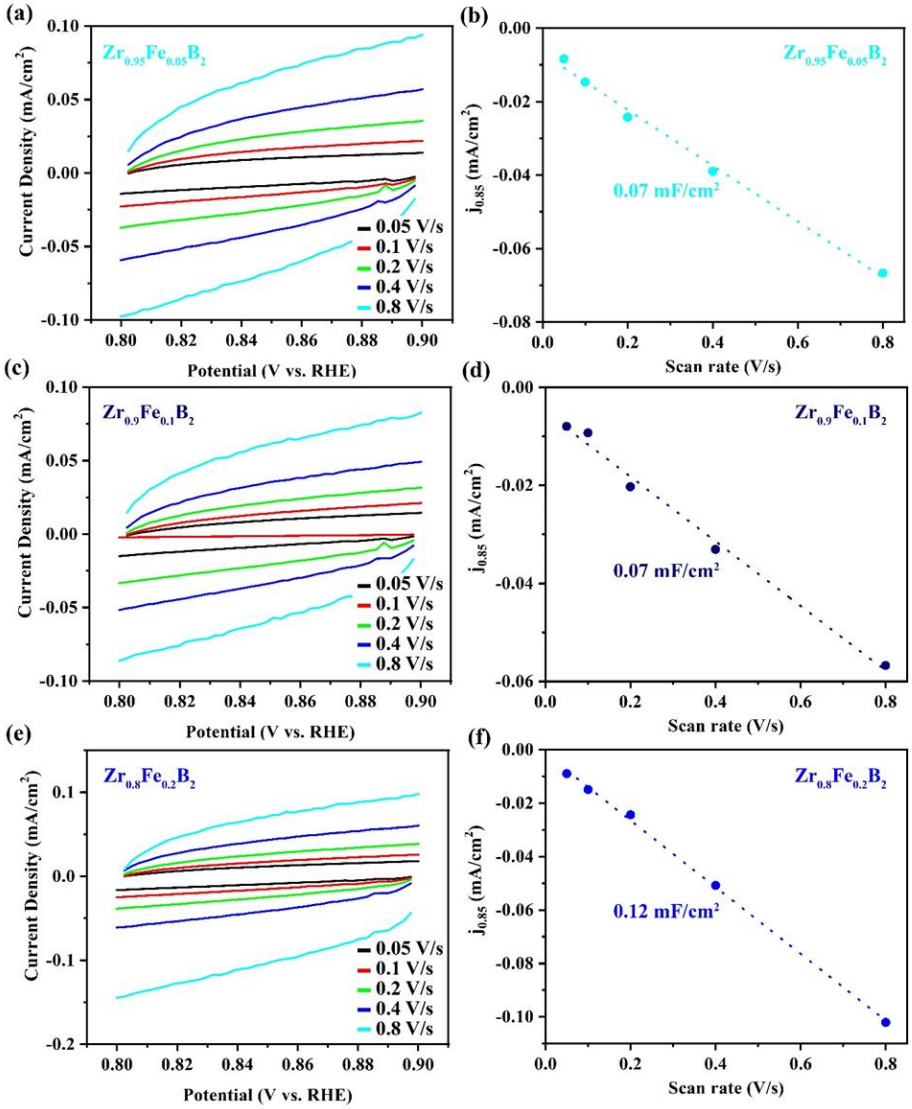

Figure 4.21 a, c, and e) Cyclic voltammograms of $Zr_{0.95}Fe_{0.05}B_2$, $Zr_{0.9}Fe_{0.1}B_2$, and $Zr_{0.8}Fe_{0.2}B_2$, respectively along with their b, d, and f) Respective capacitive current at 0.85 V as a function of the scan rate.

Substituted ZrB_2 powders with various loadings of dopants were also examined for HER and OER activity (Figure 4.19). The results indicated that raising the dopant amount of Fe, Co, and Ni in ZrB_2 structure from 0.05 to 0.2 boosted surface-active sites and consequently HER activity (Figure 4.20, 4.21 and 4.22).

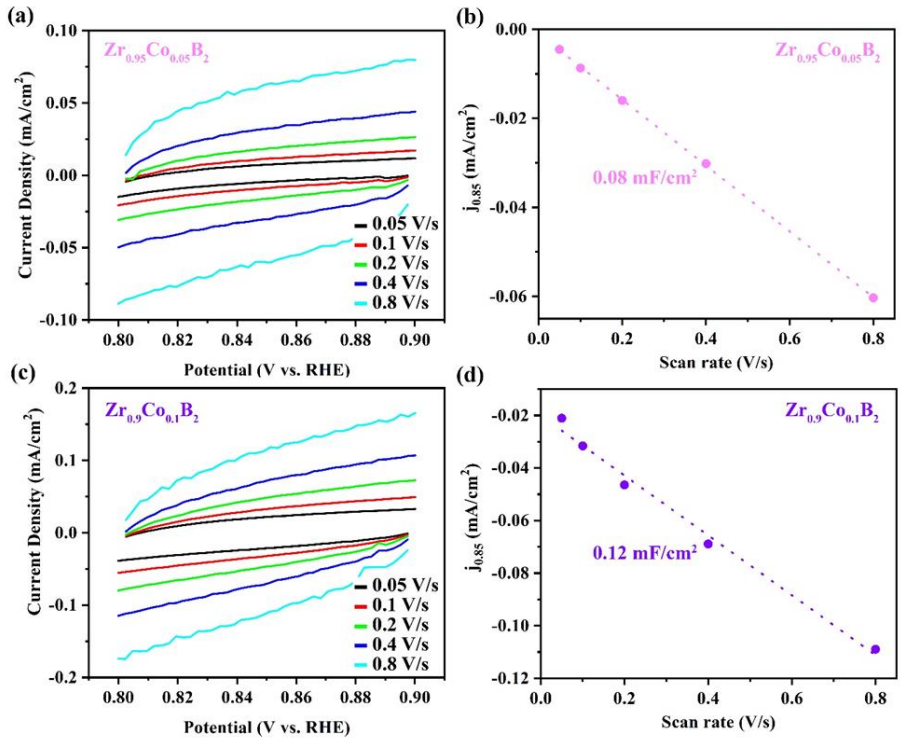

Figure 4.22 a and b) Cyclic voltammograms of $Zr_{0.95}Co_{0.05}B_2$ and $Zr_{0.9}Co_{0.1}B_2$, respectively along with their c and d) Respective capacitive current at 0.85 V as a function of the scan rate.

4.3.3 Oxygen Evolution Activities of ZrB_2 Samples

Another half-reaction of water electrolysis—OER is used as an essential indicator to appraise reaction kinetics. There is a four-electron process for the generation of a single molecule of O_2. Therefore, each kinetic barrier can increase the overall OER overpotential. Also, there are three adsorption intermediates such as OOH*, O*, and OH*, pointing out that OER suffers from slower kinetics in comparison to HER. in simple boride systems, the enhanced OER rate is initiated from the development of metal oxides/(oxy)hydroxides on the boride surface within the OER. The metal-oxygen species (MOOH) are considered active sites for oxygen evolution processes. In transition metal boride, B species prevent the complete oxidation of the metal to create stable oxides utilizing donating electrons; consequently, facilitate the production of oxyhydroxide intermediate chemicals [4].

Electrochemical performance of the ZrB_2 powders towards the OER was investigated using unsubstituted and substituted ZrB_2 electrode supported by glassy carbon (0.5 mg cm^{-2} catalyst powder) under 1 M KOH. Figure 4.23 reveals LSV polarization curves for unsubstituted and substituted ZrB_2 electrodes. For the sake of comparison, the OER activity of commercial RuO_2 as the reference material was also measured and included.

From Figure 9a, the onset potential of RuO_2 to reach a current density of 10 mA cm^{-2} is 1.52 V (overpotential of 0.29 V versus their equilibrium value of 1.23 V vs. RHE expected from thermodynamics for OER). Likewise, glassy carbon and ZrB_2 were employed as OER catalysts within the same potential window. Interestingly, they exhibited a very low current density. In contrast, investigated substituted ZrB_2 samples demonstrated enhanced current density and OER performance due partially to the incorporation of dopant in the ZrB_2 structure. In this sense, $Zr_{0.8}Ni_{0.2}B_2$ featured superior reactivity over all other substituted samples. The onset potential of $Zr_{0.8}Ni_{0.2}B_2$ to achieve the current density of 10 mA cm^{-2} is 1.58 V, an overpotential of 0.35 V, only 0.06 V higher than the obtained value for RuO_2 which is analogous to lately reported transition metal borides such as Co_2B (overpotential of 0.33 V [66]. Furthermore, this overpotential is lower than the acquired overpotentials of 0.37 and 0.5 V for Co- and Fe-substituted ZrB_2, individually.

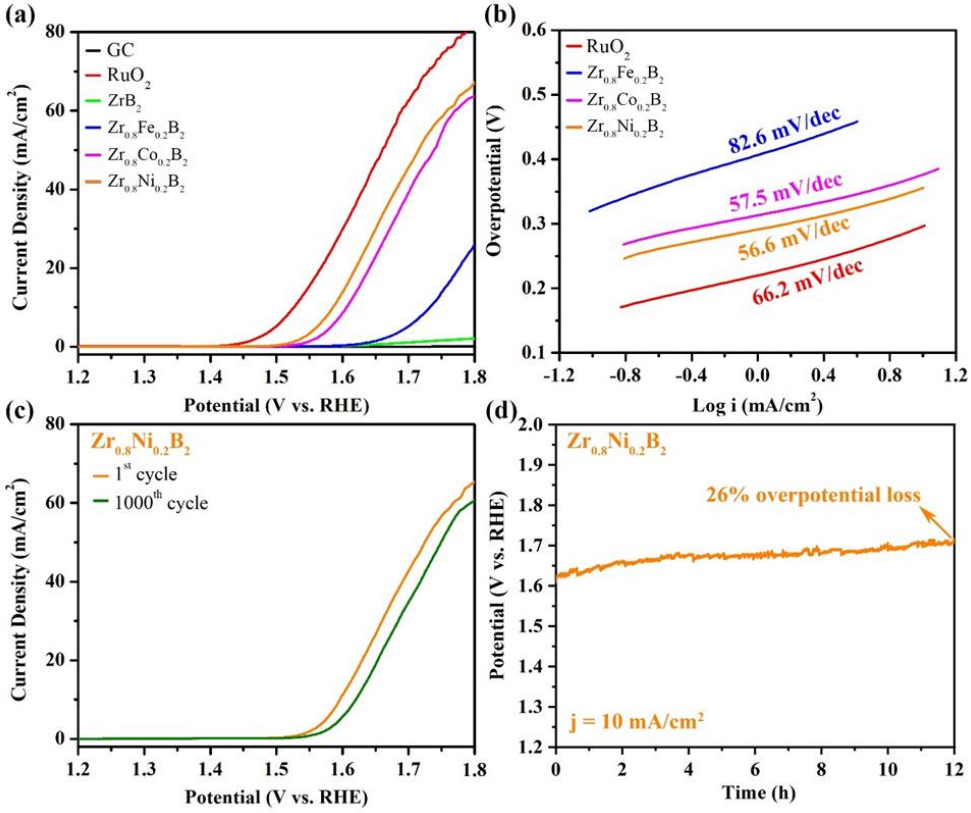

Figure 4.23 Electrochemical performance of unsubstituted and substituted ZrB_2 towards OER recorded at a scan rate of 5 mV s^{-1} in 1 M KOH. a) Polarization curves, b) Related Tafel plots, c) Polarization curves of $Zr_{0.8}Ni_{0.2}B_2$ initially and after 1000 CV scans at 100 mV s^{-1} and d) Chronopotentiometric curve of $Zr_{0.8}Ni_{0.2}B_2$ recorded at a current density of 10 mA cm^{-2}.

Figure 4.23b shows related Tafel slopes of Ni- and Co-substituted ZrB_2 (56.6 and 57.5 mV dec^{-1}, respectively) are lesser as compared to the commercial RuO_2 (66.2 mV dec^{-1}). Therefore, the outstanding performance of $Zr_{0.8}Ni_{0.2}B_2$ in OER comes as no surprise. From this perspective, it can be understood that the oxygen evolution step is the rate-determining step rather than the OH^- electrosorption. In addition, multiple electrodes were fabricated by substituted ZrB_2 powders containing different concentrations of dopants and inspected for OER activity. The findings uncovered that the concentration of Fe, Co, and Ni in ZrB_2 structure and OER activity are in direct correlation; increasing loading quantity from 0.05 to 0.2 in ZrB_2 promotes the OER activity accordingly (see Figure 4.19)

The electrocatalytic stability of the most efficient OER sample ($Zr_{0.8}Co_{0.2}B_2$) was determined through the CV experiment up to 1000 cycles across a potential range of 1.2 and 1.8 V at 100 mV s^{-1}. Figure 4.23c illustrates LSV curves towards OER for $Zr_{0.8}Ni_{0.2}B_2$ before and after 1000 cycles of operation. Interestingly, the polarization curves exhibited minor raise in onset potential from 1.58 V to 1.61 V (only a slight deviation of 0.06 V) after 1000 cycles. Furthermore, from Figure 4.23d, the long-run durability of the $Zr_{0.8}Ni_{0.2}B_2$ electrode can be observed at the current density of 10 mA cm^{-2} for 12 h showing 26% loss in overpotential within this period, indicating decent stability under alkaline conditions. It is emphasized that similar to HER, $Zr_{0.7}Ni_{0.3}B_2$ and $Zr_{0.7}Co_{0.3}B_2$ catalysts were tested towards OER. Unfortunately, their insignificant activities discouraged us to evaluate following measurements.

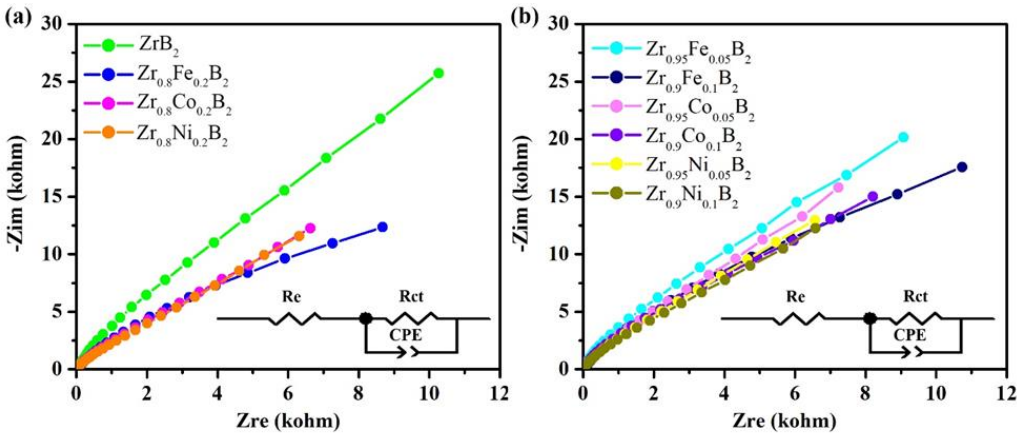

Figure 4.24 Niquist plots of a) ZrB_2 and $Zr_{0.8}TM_{0.2}B_2$ (*TM* = Fe, Co, and Ni), b) $Zr_{1-x}TM_xB_2$ (*TM* = Fe, Co, and Ni , *x* = 0.05, 0.1, and 0.2)

Figure 4.24 shows EIS data and the equivalent circuits while the electrodes were placed in contact with electrolyte. In the equivalent circuit, Re represents the resistance of the solution between the working and reference electrodes. On the surface of electrodes, the impedances of the interfacial reactions are described as capacitive component and a Faraday resistance. The capacitive element can be replaced by a constant-phase element (CPE) due to the complex nature of the interfacial reaction, and Rct as a Faraday resistance represents the charge transfer resistances of the electrodes. The outcomes have been corroborated by the EIS data as well, which confirm that $Zr_{0.8}Ni_{0.2}B_2$ enjoys the lowest charge transfer resistances amidst all samples.

4.3.4 The Substitution Effect of Ni and Co

As discussed above, the HER is H_2O reduction process by two-electron transfer path having H^* as the only key intermediate according to the following reaction in basic solution [8], [19]:

$2H_2O + 2e^- \rightarrow H_2 + 2OH^-$

On the other hand, the OER reaction proceeds via a more sluggish route— four-electron transfer, bearing several oxygen-containing intermediates such as OH, O, and OOH based upon reaction below [19], [71]:

$4OH^- \rightarrow 2H_2O + O_2 + 4e^-$

Following the Sabatier principle, a decent HER catalyst is bound to H^* with moderate energy [8], which is mainly determined by adsorption free energy of atomic hydrogen (ΔG_{H^*}). That is why Pt-based materials so far have been the most superior of all electrocatalysts with hydrogen adsorption of $\Delta G_{H^*} \approx 0$ [71]. To this end, it was found that the electronic structure of borides is a vital indicator to manipulate the surface adsorption energy and influence their catalytic properties. Therefore, multiple reports declared that the HER performance of borides is directly correlated with metal d-band properties, affecting hydrogen adsorption. Keeping these in mind, metal d-band properties of borides rely upon several parameters such as hybridization of metal–boron orbital, length of metal-metal bonding, and charge transfer between metal and boron [71]. In this regard, for the case of HER activity of transition metal-substituted ZrB_2, d-band properties as well as hydrogen adsorption energy favor Co-containing samples with the following trend Co- > Ni- > Fe-. Furthermore, electron transfer between Co and B in the structure

improves both charge conduction in the course of water reduction and catalytic resistance against deactivation [9].

Due to the fact that OER is viewed as a barrier in water splitting reaction, the catalytic performance of metal borides in OER has attracted much attention. While some declare that active species of borides during OER is metal oxide/hydroxide layer on the electrode surface; for instance FeOOH for FeB_2 [72], others believe that metaborate containing oxyhydroxide on the surface of borides is responsible for the high activity on OER [71]. Even though Ir- and Ru-based materials are identified as superb catalysts for OER, they have limited activity under alkaline media. On the contrary, compounds based on VIII group 3d metals (Ni, Co, and Fe) perform more facilitatively under basic solutions [19]. Feifan Guo et al. [73] conducted a boronization experiment on Ni, Co, Fe, NiFe alloys, and steel sheets to form M_2B layers as OER catalysts. Their results showed that the boronized Ni-containing sheet performs the highest among transition metals with a trend as follows Ni > Co > Fe. The same trend also observed in our experiments, manifesting $Zr_{0.8}Ni_{0.2}B_2$ as a newly emerged electrocatalyst for OER.

It was reported that for the case of boronized Ni sheet, the transformed surface compounds oxides into γ-NiOOH are the active phases during OER. The authors claimed that metaborate containing oxyhydroxides on the electrode surface fine-tune electronic distribution on the surface of the catalyst and intensify the electron density of Ni atoms. As a consequence, it was pointed out that the electronic characteristics of NiOOH could optimize the binding energy of oxygen intermediates, resulting in improved OER performance. According to the preceding story, Ni substitution modified electron distribution on the surface and gave rise to an outstanding OER activity compared to Co- and Fe-substituted samples. Despite these findings, there is no clear bridge between the electronic structure of borides and their OER activity [71].

Table 4.1 Summary of electrochemical parameters for all as-prepared samples

Sample	HER overpotential (V)	HER Tafel slope (mV dec^{-1})	OER overpotential (V)	OER Tafel slope (mV dec^{-1})	EASA	Rct (kohm)
Pure ZrB_2	0.7	226	-	-	2.25	203
$Zr_{0.95}Fe_{0.05}B_2$	0.72	165	-	-	1.75	133
$Zr_{0.9}Fe_{0.1}B_2$	0.6	159.1	-	-	2.5	95
$Zr_{0.8}Fe_{0.2}B_2$	0.51	144.4	0.5	82.6	3	64
$Zr_{0.95}Co_{0.05}B_2$	0.53	132.6	0.47	70	2	144
$Zr_{0.9}Co_{0.1}B_2$	0.46	124.8	0.4	59.9	3	46
$Zr_{0.8}Co_{0.2}B_2$	**0.42**	**101.6**	0.37	57.5	**4.75**	45
$Zr_{0.7}Co_{0.3}B_2$	0.60	129.1	0.44	72.1	-	-
$Zr_{0.95}Ni_{0.05}B_2$	0.58	160.6	0.4	57.7	2.25	48
$Zr_{0.9}Ni_{0.1}B_2$	0.52	132.4	0.36	57.4	2.75	47
$Zr_{0.8}Ni_{0.2}B_2$	0.48	119.5	**0.35**	**56.6**	3.75	**42**
$Zr_{0.7}Ni_{0.3}B_2$	0.64	121.4	0.37	67.2	-	-
Pt/C	0.198	85.2	-	-	-	-
RuO_2	-	-	0.29	66.2	-	-

- The bold fonts indicate the best value among the related parameters.

4.4 Characterization of HfB_2 and TM-Substituted HfB_2 (TM= Co, Ni)

4.4.1 Chemical Characterization Results

Transition metal substituted and unsubstituted HfB_2 samples were synthesized with the carbothermal reduction method as discussed in *Section 4.2*. The theoretical X-ray diffraction pattern of HfB_2 (International Centre for Diffraction Data (ICDD), PDF -4+ 2011 RDB, Card No: 1510711) in comparison with as-synthesized HfB_2, Co- and Ni-substituted HfB_2 patterns are illustrated in Figure 1 and Figure SI 1. Since the main pattern perfectly fits for all reflections, the figures show the targeted phase of $Hf_{(1-x)}TM_xB_2$ (x = 0.1, 0.2 and 0.3) was achieved successfully. The low intensity peaks representing the negligible amount of secondary phases which are HfO_2 (marked by "*") at 2θ of 28.2º, 31.3º, 34º,50.2º and 59.9º and HfB (marked by "o") at 2θ of 33.5º and 38.9º in as-synthesized HfB_2 and $Hf_{0.8}TM_{0.2}B_2$ (*TM*= Co and Ni) samples.

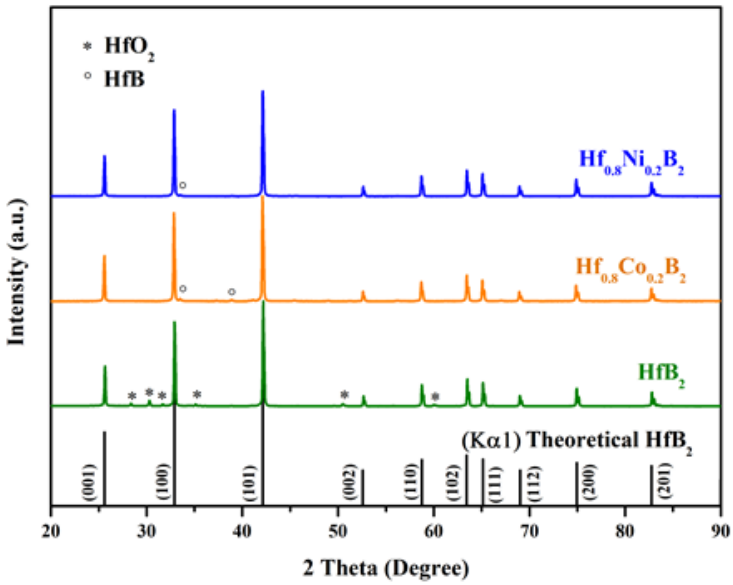

Figure 4.25 XRD patterns of HfB_2 and $Hf_{0.8}TM_{0.2}B_2$ (*TM*= Co and Ni)

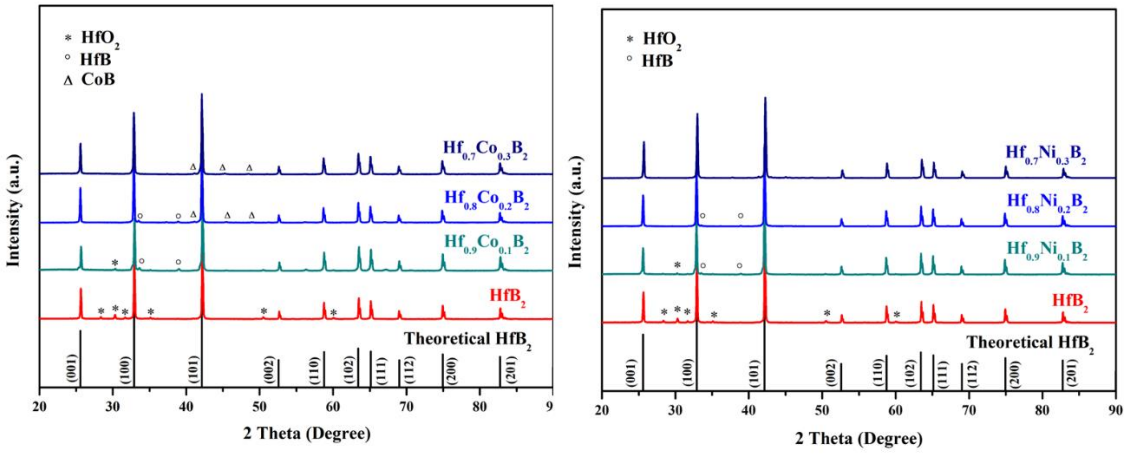

Figure 4.26 XRD patterns of unsubstituted HfB_2 with theoretical pattern and **a)** $Hf_{(1-x)}Co_xB_2$ **b)** $Hf_{(1-x)}Ni_xB_2$ (*x*= 0.1,0.2 and 0.3)

The decreasing trend of HfO_2 and HfB formation as the ratio of transition metal substitution increases (Figure 4.26), may have positively influenced the electrocatalytic activity of HfB_2. For both TM substitution experiments, at *x*=0.2 there was no clear observation on unreacted TM and TM-B phase formation therefore, it indicates the almost complete substitution was achieved without exceeding the saturation limit.

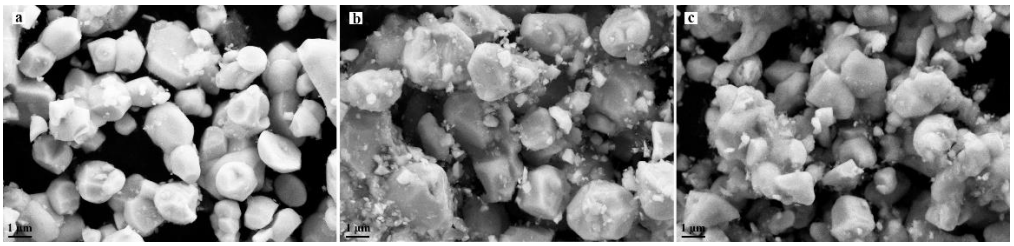

Figure 4.27 SEM images of a) unsubstituted-HfB_2 b) $Hf_{0.8}Ni_{0.2}B_2$ c) $Hf_{0.8}Co_{0.2}B_2$

Similar with ZrB_2 powders, HfB_2 possess spherical shaped particles with layered stacking ranging between submicrometer to 1-2 µm size. SEM micrographs of as-synthesized HfB_2 and $Hf_{0.8}TM_{0.2}B_2$ (*TM*= Co and Ni) are presented in Figure 4.27. The SEM images display layered spherical shape for HfB_2 sample obtained at 1723 K (Figure 4.28). HfB_2 has a hexagonal crystal structure (a = 3.14 Å and c = 3.48 Å) [74]. To observe the effect of substitution on morphology of the powder, SEM was conducted on Co- and Ni- substituted samples as well for x= 0.1, 0.2 and 0.3. It can be concluded that with the transition metal incorporation into the structure, the spherical shape of the particles is preserved.

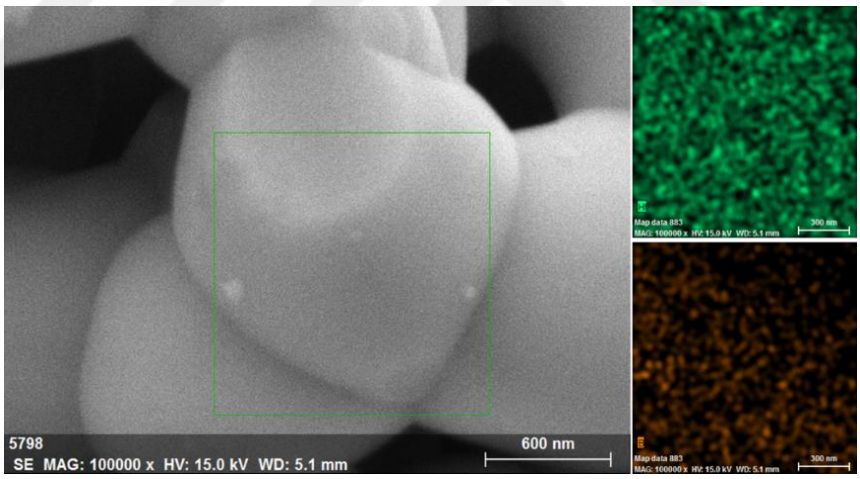

Figure 4.28 High magnification SEM image of unsubstituted HfB_2 along with EDS elemental mapping on the right side

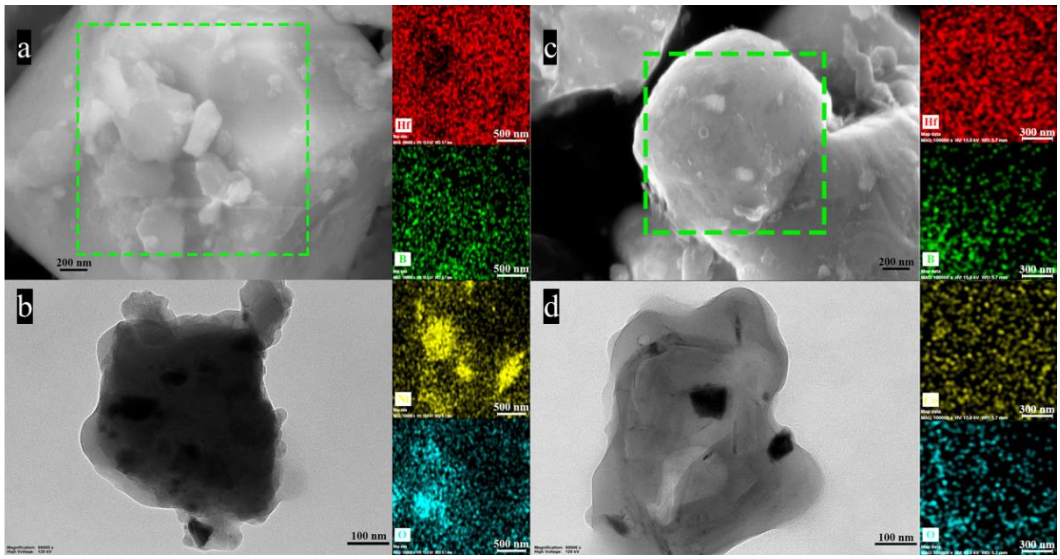

Figure 4.29 Characterization of metal-substituted HfB_2. a) High magnification SEM image of $Hf_{0.8}Ni_{0.2}B_2$ b) TEM of $Hf_{0.8}Ni_{0.2}B_2$, along with related EDS mapping on the right side c) High magnification SEM image of $Hf_{0.8}Co_{0.2}B_2$ d) TEM of $Hf_{0.8}Co_{0.2}B_2$, along with related EDS mapping on the right side.

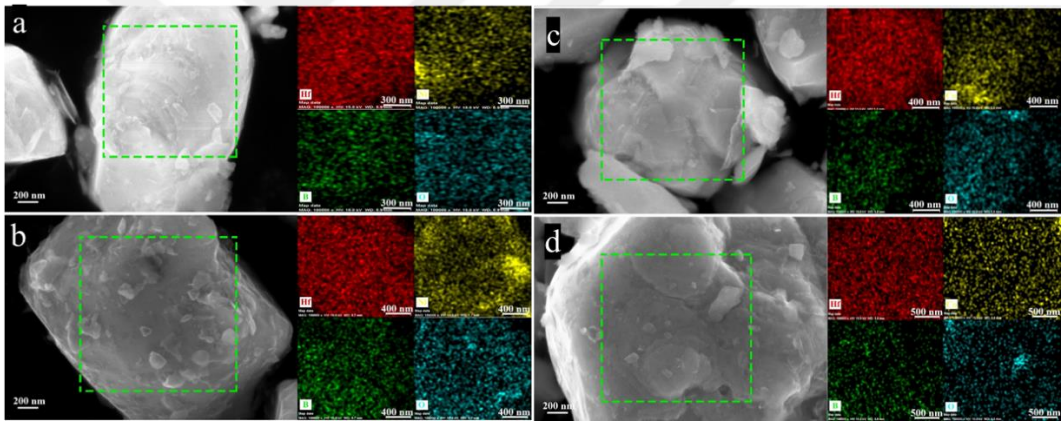

Figure 4.30 Characterization of metal-substituted HfB_2. High magnification SEM images of a) $Hf_{0.9}Ni_{0.1}B_2$ b) $Hf_{0.7}Ni_{0.3}B_2$ c) $Hf_{0.9}Co_{0.1}B_2$ c) $Hf_{0.7}Co_{0.3}B_2$ along with related EDS mapping on the right side.

High magnification SEM images are given in Figure 4.29a and 4.29c for $Hf_{0.8}Ni_{0.2}B_2$ and $Hf_{0.8}Co_{0.2}B_2$, respectively. Low magnification SEM images of these are given in Appendix figure A2, along with EDS mapping and unsubstituted HfB_2 powder. On the right-hand side, the EDS elemental mapping of samples are presented, showing the homogeneous distribution of elements through grains. High magnification SEM with EDS mapping for unsubstituted HfB_2 is given in Figure 4.28. A thin layer of surface oxidation on all samples resulted in oxygen presence in the EDS mapping. Additionally, for the $Hf_{0.9}Ni_{0.1}B_2$, $Hf_{0.7}Ni_{0.3}B_2$, $Hf_{0.9}Co_{0.1}B_2$ and $Hf_{0.7}Co_{0.3}B_2$ samples, low magnification SEM images are given in the Appendix figure A1.

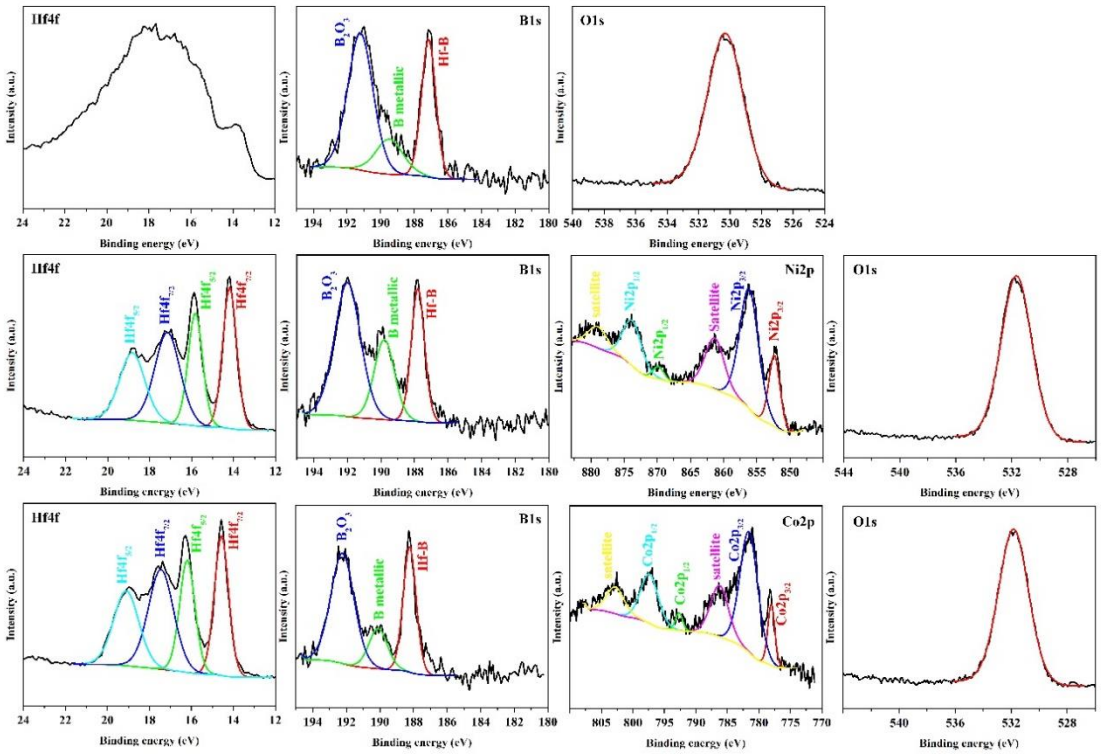

Figure 4.31 XPS spectra of a) unsunstitued-HfB_2 b) $Hf_{0.8}Ni_{0.2}B_2$ and c) $Hf_{0.8}Co_{0.2}B_2$

X-ray photoelectron spectroscopy (XPS) was conducted to inspect the chemical features of the metals and dopants in the as-prepared electrocatalysts. Figure 4.31 shows XPS studies of HfB_2, Co-, Ni- substituted HfB_2 powders. Hf 4f, B 1s, Ni 2p and Co 2p spectra have been analyzed. Besides, O 1s spectra have also been considered, explaining the trace amount of surface oxides. Double-peak indexed to Hf $4f_{5/2}$-$4f_{7/2}$ and two single peak related to B 1s with B satellite for all samples, indicating the two distinctive chemical states for Hf and B atoms. Transition metal substituted samples display Hf $4f_{5/2}$, and Hf $4f_{7/2}$ peaks positioned at respective approximate binding energies of ~ 19 and 17 eV. The presence of surface oxides can also be evidenced with respect to the emergence of O 1s peaks at 532 eV, as shown in the pattern of Figure 4.31. Thus, the XPS results substantiate that B_2O_3 can be found on the surface of all samples. Knowing that XPS is a surface analysis technique, it can be noticed that based on these findings there are partially oxidized species on the surface. This surface oxidation might be one of the reasons for such high activity as mentioned in the Chapter 2 of the thesis.

Co 2p and Ni 2p peaks were detected for substituted samples, confirming the presence of Co and Ni containing species in HfB_2 structure. For the Ni 2p spectrum (Figure 4.31b) the binding energies located at 874.1 eV for Ni $2p_{1/2}$ and 856.2 eV for Ni $2p_{3/2}$ can be ascribed to NiB [61]. Also, the binding energies positioned at 869.4 eV for

Ni $2p_{1/2}$ and 853.2 eV for Ni $2p_{3/2}$ can be appertained to Ni [62]. Finally, the peaks observed at 862 and 879 eV pertain to the satellite peaks [59]. The deconvolution and curve-fitting were carried out for Co 2p. The spectrum shown in Figure 4.31c revealed two spin−orbit doublets: including 798 eV (Co $2p_{1/2}$) and 782 eV (Co $2p_{3/2}$) correlated with Co^{2+} (CoO) [55] as well as 793 eV (Co $2p_{1/2}$) and 778 eV (Co $2p_{3/2}$) corresponding to Co^0 [56] . Moreover, there are two extra peaks at 782 and 802 eV which are attributed to satellite peaks [57]–[60].

4.4.2 Hydrogen Evolution Activities of HfB_2 Samples

The hydrogen evolution reaction (HER) catalytic activity of unsubstituted and substituted HfB_2 powders was also evaluated 1 M KOH electrolyte, by loading 0.5 mg cm^{-2} catalyst powder on glassy carbon electrode. Figure 4.32a reveals the related LSV polarization curves. The HER activity of commercial 10% Pt/C catalyst was also examined for comparison in the similar way to synthesized powders. The results showed that Pt/C as a state-of-the-art HER catalyst has an overpotential of 198 mV at 10 mA cm^{-2} current density requiring for hydrogen evolution. The glassy carbon used as an inert substrate for HER with a negligible activity. In Figure 4.32a, it can be pointed out that the HER overpotential of HfB_2 (620 mV) is much higher than the Pt/C. On the contrary, substituted HfB_2 enhances HER activity. In this sense, $Hf_{0.8}Co_{0.2}B_2$ and $Hf_{0.8}Ni_{0.2}B_2$ showed the overpotentials of 430 and 530 mV at 10 mA cm^{-2} current density, respectively, indicating an improvement over the parent sample. This result suggests that HER activity of $Hf_{0.8}Co_{0.2}B_2$ moves forward in an efficient manner. This finding is in accordance with the Co-based borides in the literature which are favorable catalysts towards HER activity. The overpotential value of $Hf_{0.8}Co_{0.2}B_2$ is relatively comparable to the previously reported transition-metal borides such as Co_2B-500 with an overpotential of 328 mV at 10 mA cm^{-2} current density [66].

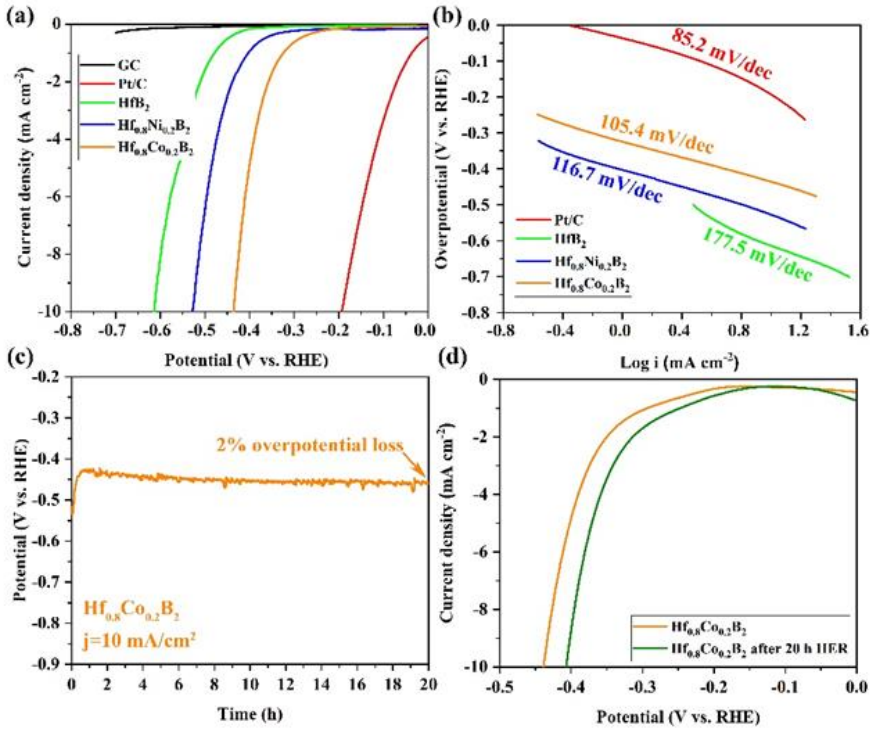

Figure 4.32 Electrochemical performance of unsubstituted and substituted HfB_2 towards HER recorded at a scan rate of 5 mV s^{-1} in 1 M KOH. a) Polarization curves, b) Related Tafel plots, c) Chronopotentiometric curve of $Hf_{0.8}Co_{0.2}B_2$ recorded at a current density of 10 mA cm^{-2}, and d) Polarization curves of $Hf_{0.8}Co_{0.2}B_2$ initially and after 20 h OER stability.

Figure 4.32b reveals the related Tafel plots calculated for unsubstituted and substituted HfB_2 catalysts, indicating a current density increase with overpotential. The Tafel slope is used as an index for determining the HER kinetics and it can be provided further insights into the HER mechanism. In alkaline media, the HER mechanism is sensitive to the catalyst surface structure and theoretical works revealed that it includes two major steps: the Volmer adsorption and the desorption process.

Volmer step: $H_2O + e^- \rightarrow OH^- + H_{ad}$

Heyrovsky step: $H_2O + e^- + H_{ad} \rightarrow OH^- + H_2$

where H_{ad} is hydrogen adsorption in alkaline media. In this media, hydrogen binds to the catalyst via the Volmer adsorption. After that, the desorption process can occur by the Heyrovsky step. The Tafel slopes reported for the Volmer and Heyrovsky steps are 120 and 40 mV dec^{-1}, respectively [3].

The measured Tafel slopes in Figure 4.32b showed the lowest Tafel slope (85.2 mV dec^{-1}) for commercial Pt/C catalyst compared with synthesized samples. As expected, the Tafel slope of $Hf_{0.8}Co_{0.2}B_2$ is lower (105.4 mV dec^{-1}) than $Hf_{0.8}Ni_{0.2}B_2$ and HfB_2 (116.7 and 177.5 mV dec^{-1}, respectively), indicating facile HER kinetics compared with parent

catalyst. Based on the Volmer and Heyrovsky steps, it can be concluded that the calculated Tafel slopes for substituted synthesized samples are in the range of 100-120 mV dec^{-1}, manifesting the HER reaction is dominated by the Volmer mechanism.

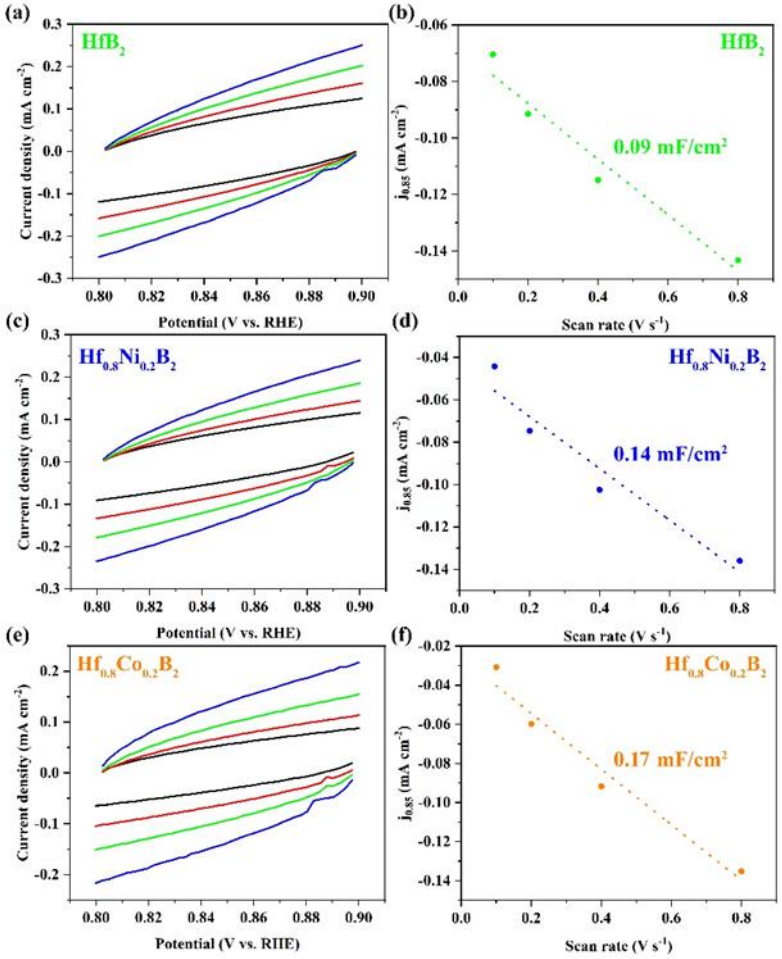

Figure 4.33 a, c, and e) Cyclic voltammograms of HfB_2, $Hf_{0.8}Ni_{0.2}B_2$, and $Hf_{0.8}Co_{0.2}B_2$, respectively along with their b, d, and f) Respective capacitive current at 0.85 V as a function of the scan rate.

Based on the literature, in the term of ideal Tafel slopes, smaller slopes are preferred [67]. Active sites play a crucial role in the alkaline HER performance. A lack of proton accessibility to the abundant active sites enhances the rate of Tafel slope. In this sense, the electrochemically active surface area was examined by using the electrochemical double-layer capacitance (C_{DL}) of the synthesized catalyst surface. EASA indicates the total surface area of the surface-active sites. C_{DL} is measured by using cyclic voltammetry, recorded at multiple scan rates in a non-Faradaic potential region which is a potential range in a 0.1 V window centered at the open-circuit potential (OCP) [68]. The CV plots and calculated EASA are shown in Figure 4.33. The C_{dl} was calculated as following:

$$i_c = \nu C_{dl}$$

where, i_c and ν are double layer charging current and scan rate, respectively. C_{dl} can be gained as a slope of i_c (measured at potential of center of window) plotted against ν. The EASA can be obtained using the following equation:

$EASA = C_{dl}/C_s$

where C_s is the specific capacitance of the sample. This capacitance is considered equal to 0.040 mF cm^{-2} in the 1 M KOH medium [68]. From Figure 4.33, the calculated C_{dl} value for $Hf_{0.8}Co_{0.2}B_2$ is 0.16 mF cm^{-2} which is higher than the calculated C_{dl} values for $Hf_{0.8}Ni_{0.2}B_2$ and HfB_2 (0.09 and 0.14 mF cm^{-2}, respectively), indicating more available catalytic sites for HER process.

4.4.3 Oxygen Evolution Activities of HfB_2 Samples

The oxygen evolution reaction (OER) serves as an essential indicator in the anodic half-reaction in water splitting. Although there are different kinds of proposed OER mechanism, the real OER process is complicated and not clear. However, the OER moves forward through a four-electron transfer pathway with the same intermediates. They involve three oxygen-containing intermediates including M-O, M-OH, and M-OOH, which M is referred to the active site. It should be mentioned that the active site plays an important role in these steps and the OER suffers from sluggish kinetics in comparison to the other cathodic half-reaction [75]. The water oxidation reaction under alkaline conditions is express by the equation that is usually assumed to proceed in four elementary steps:

$4OH^- \rightarrow O_{2\,(g)} + 2H_2O_{\,(l)} + 4e^-$

Metal borides reveal high OER catalytic activity due to their unique atomic geometry structures. The boron atoms distort native atomic geometry and expedite the oxidation of metal atoms during electron transfer process, therefore, facilitate hydroxyl groups and water molecules adsorption and oxidation. Ma and co-workers concluded that CoOOH species on the surface are the real active sites of Co_xB catalysts and boron atoms facilitate the oxidation of Co, leading to positive effect on the OER activities [36].

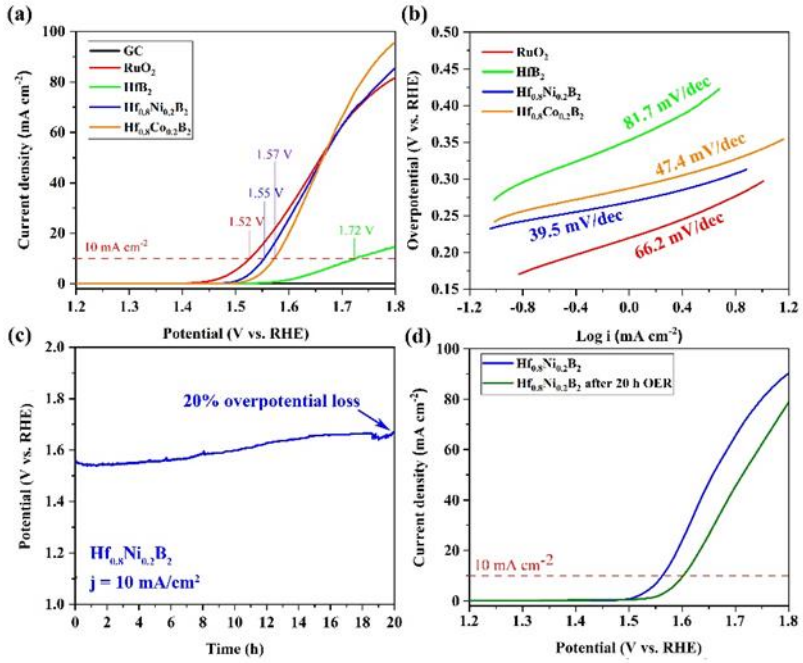

Figure 4.34 Electrochemical performance of unsubstituted and substituted HfB_2 towards OER recorded at a scan rate of 5 mV s^{-1} in 1 M KOH. a) Polarization curves, b) Related Tafel plots, c) Chronopotentiometric curve of $Hf_{0.8}Ni_{0.2}B_2$ recorded at a current density of 10 mA cm^{-2}, and d) Polarization curves of $Hf_{0.8}Ni_{0.2}B_2$ initially and after 20 h OER stability.

The OER catalytic activity of unsubstituted and substituted HfB_2 powders was evaluated 1 M KOH electrolyte, by loading 0.5 mg cm^{-2} catalyst powder on glassy carbon electrode. Figure 4.34a presents the related LSV polarization curves. The OER activity of commercial RuO_2 powder as the reference material was also measured for comparison in the similar way to hafnium diboride powders. Likewise, glassy carbon was used as a neutral substrate due to it exhibited a negligible current density within the same potential window. From Figure 4.34a, HfB_2 reveals the potential of 1.72 V in a density of 10 mA cm^{-2} and overpotential of 490 mV versus their equilibrium value of 1.23 V vs. RHE expected from thermodynamics for OER, a sort of high overpotential for OER process. In contrast, Ni and Co substituted HfB_2 catalysts demonstrated enhanced OER performance with lower overpotentials. Based on the results, $Hf_{0.8}Ni_{0.2}B_2$ featured superior reactivity over all other samples with the overpotential of 320 mV close to RuO_2, only 30 mV higher than the obtained value for RuO_2 (overpotential of 290 mV). It is comparable to previous reported transition metal borides such as Co–Mo–B (overpotential of 320 mV) [76] and Co_2B (overpotential of 330 mV) [66]. Furthermore, this overpotential is lower than the overpotential of for $Hf_{0.8}Co_{0.2}B_2$ (340 mV). From the results, it could be concluded that the enhanced current density and diminished

overpotentials of substituted HfB_2 is as the result of the incorporation of Co and Ni elements in the HfB_2 structure.

The related Tafel slopes of unsubstituted and substituted HfB_2 are shown in Figure 4.34b. The Tafel slope of $Hf_{0.8}Ni_{0.2}B_2$ and $Hf_{0.8}Co_{0.2}B_2$ samples (39.5 and 47.4 mV dec^{-1}, respectively) are lesser as compared to the commercial RuO_2 (66.2 mV dec^{-1}) indicating a faster current density increase with overpotential, therefore more facile electrode kinetics of substituted HfB_2 compared to the RuO_2. Thus, the notable OER activity of $Hf_{0.8}Ni_{0.2}B_2$ comes as no surprise.

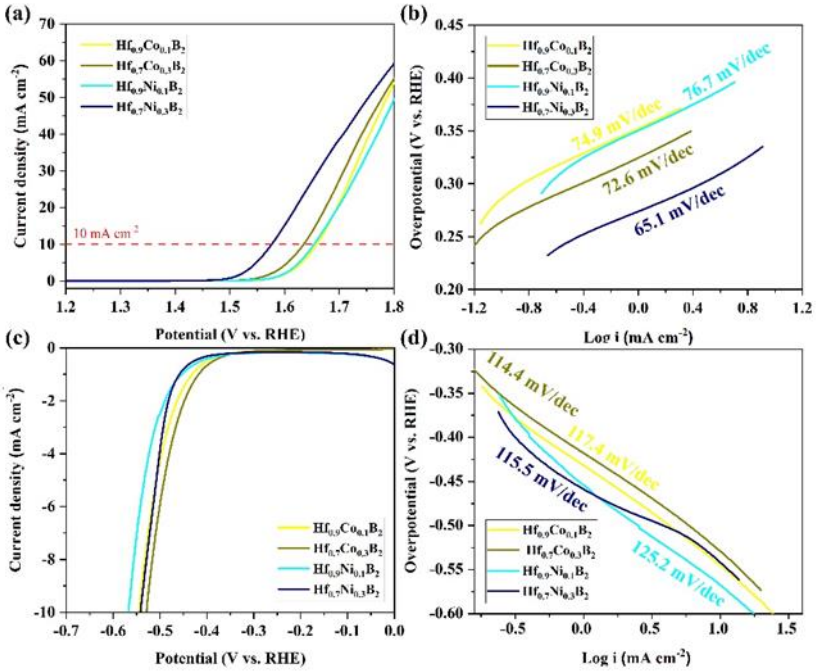

Figure 4.35 Electrochemical performance of substituted HfB_2 towards OER recorded at a scan rate of 5 mV s^{-1} in 1 M KOH, a) Polarization curves, b) Related Tafel plots, and electrochemical performance of substituted HfB_2 towards HER recorded at a scan rate of 5 mV s^{-1} in 1 M KOH. a) Polarization curves, b) Related Tafel plots.

For evaluating the effect of substitution element content on OER activity, substituted HfB_2 powders containing different concentrations of Ni and Co ($Hf_{0.9}TM_{0.1}B_2$ and $Hf_{0.7}TM_{0.3}B_2$, *TM*: Ni and Co) were synthesized and inspected for OER activity. The results showed that although increasing content of the substitution element from 0.1 to 0.2 could enhance catalytic activity significantly, further increasing of substitution content from 0.2 to 0.3 diminished the OER activity. Thus, based on the results, there is a substitution limit for the activity improvement (Figure 4.35a and b).

The long-term stability of the most efficient OER catalyst ($Hf_{0.8}Ni_{0.2}B_2$) was evaluated by using chronopotentiometry method at a current density of 10 mA cm^{-2} for 20 h. Based on the result shown in Figure 4.34c, there is only 20% loss in overpotential

after 20 h indicating decent stability of $Hf_{0.8}Ni_{0.2}B_2$ catalyst under alkaline conditions. Figure 4.34d also illustrates LSV curves of OER activity for $Hf_{0.8}Ni_{0.2}B_2$ before and after stability test. Interestingly, the LSV curves showed minor raise in potential at 10 mA cm^{-2} from 1.55 V to 1.60 V (only a slight deviation of 0.05 V) after 20 h long-run durability.

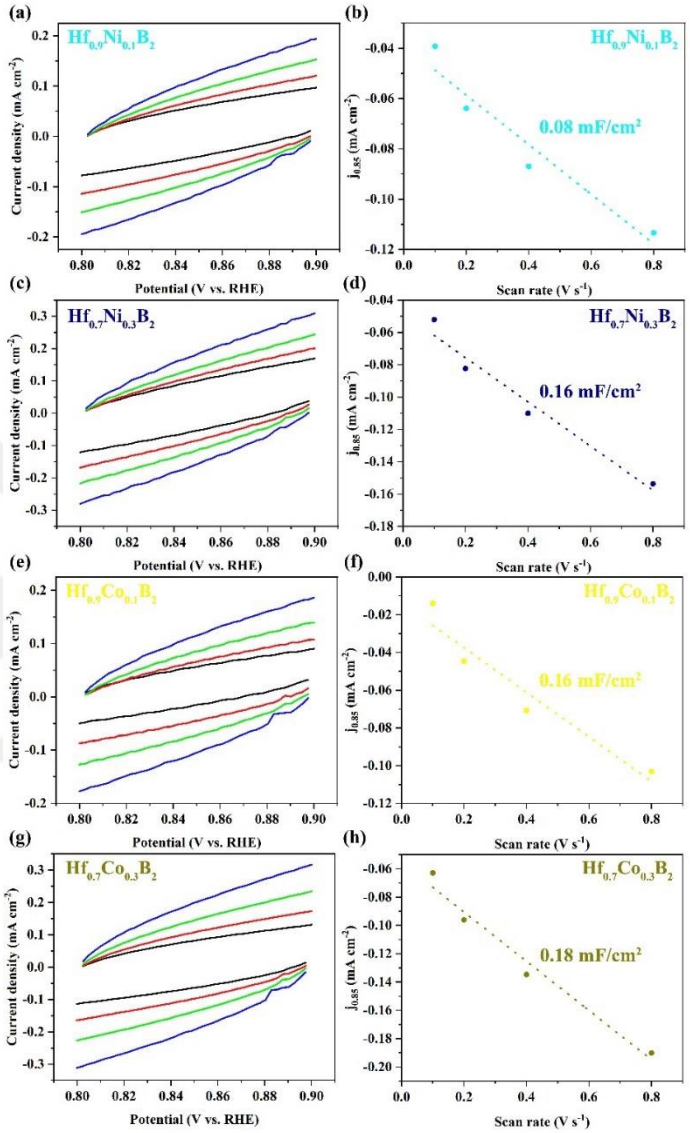

Figure 4.36 a, c, e) and g) Cyclic voltammograms of $Hf_{0.9}Ni_{0.1}B_2$, $Hf_{0.7}Ni_{0.3}B_2$, $Hf_{0.9}Co_{0.1}B_2$, and $Hf_{0.7}Co_{0.3}B_2$ respectively along with their b, d, f and h) Respective capacitive current at 0.85 V as a function of the scan rate.

Similar to the OER, the effect of substitution element content on HER activity were also evaluated. For this reason, substituted HfB_2 powders containing different concentrations of Ni and Co ($Hf_{0.9}TM_{0.1}B_2$ and $Hf_{0.7}TM_{0.3}B_2$, *TM*: Ni and Co) were inspected for HER activity (Figure 4.35). Based on the results, increasing content of the substitution element from 0.1 to 0.2 enhanced HER catalytic activity. On the other hand, increasing of substitution content from 0.2 to 0.3 increased the overpotential and

consequently diminished the HER activity. The EASA results for different content of Ni and Co substitutions also indicated that increasing the substitution amounts boosted surface-active (see Figure 4.36).

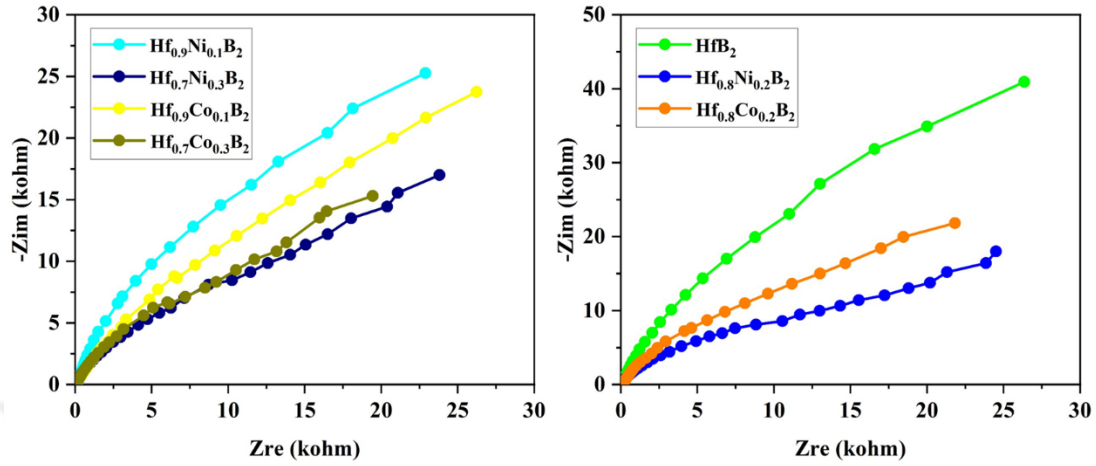

Figure 4.37 Niquist plots of a) $Hf_{(1-x)}TM_xB_2$ (*TM* = Co, and Ni) (*x*= 0.1 and 0.3), on the left side b) HfB_2 and $Hf_{0.8}TM_{0.2}B_2$ (*TM* = Co, and Ni) on the right-hand side

To explore the lifetime during hydrogen production, the long-term stability of the best-performing HER catalyst ($Hf_{0.8}Co_{0.2}B_2$) was assessed by using chronopotentiometry method at a current density of 10 mA cm^{-2} for 20 h (see Figure 4.32c). From the figure, after 20 h continuous operation, the overpotential exhibited only 2% loss, demonstrating superior durability of the $Hf_{0.8}Co_{0.2}B_2$ catalyst for HER. Figure 4.34d also illustrates LSV curves of HER activity for $Hf_{0.8}Co_{0.2}B_2$ before and after stability test. It can be observed that there is a drop from 480 to 410 mV after 20 h continuous operation, which implies superior durability of $Hf_{0.8}Co_{0.2}B_2$ catalyst towards HER activity. This output is consistent with the literature that continuous degradation of surface oxide layers exposes more active sites, therefore an improvement in activity can be observed [69].

Chapter 5:
CONCLUSION

In this thesis, the transition metal substitution effect (Fe, Ni and Co) into *TM*B_2 (*TM*= Zr, Hf) with various substitution rates (x=0.05,0.1,0.2 and 0.3) were studied. A set of samples were prepared by the carbothermal reduction method with the help of mechanical activation to decrease elevated reaction temperatures. XRD patterns of the samples were successfully matched with theoretical diffraction peak points along with small peaks of secondary phases when substitution reached to the saturation limit. SEM with EDS analysis confirmed the successful and homogeneous substitution of transition metals into spherical-shaped diborides. In the XPS analysis, Co 2p, Ni 2p and Fe 2p peaks were detected, proving the presence of Co, Ni and Fe-containing species in the structure. Electrochemical performances of the samples were investigated using unsubstituted and substituted submicron-sized powder supported by glassy carbon electrode with 0.5 mg cm^{-2} catalyst loadings in 1 M KOH electrolyte solution. To compare the activity of samples, the reference noble metal electrocatalysts were also examined under the same conditions.

All ZrB_2-based electrocatalysts showed superior stability after 12 h. $Zr_{0.8}Co_{0.2}B_2$ and $Zr_{0.8}Ni_{0.2}B_2$ were found to be the best-performing electrocatalysts in HER and OER under 1 M KOH, respectively. In the case of HER, Co-, Ni- and Fe-substituted ZrB_2 electrodes displayed Tafel slopes of 101.6, 119.5, and 144.4 mV dec^{-1}, respectively, manifesting facile kinetics and fast electron transport compared with parent catalyst with Tafel slope of 226 mV dec^{-1} indicating the Volmer mechanism. The electrochemical measurements showed an overpotential of 700 mV for ZrB_2, which is much higher than the Pt/C reference electrode. $Zr_{0.8}Co_{0.2}B_2$ showed the lowest overpotential (420 mV), indicating the best result in terms of the HER performance compared to its counterparts; $Zr_{0.8}Ni_{0.2}B_2$ and $Zr_{0.8}Fe_{0.2}B_2$ with overpotentials of 480 and 510 mV, respectively. In the case of OER, the onset potential of $Zr_{0.8}Ni_{0.2}B_2$ at the current density of 10 mA cm^{-2} is 1.58 V, an overpotential of 0.35 V, only 0.06 V higher than the obtained value for RuO_2 reference electrode. The Tafel slopes of Ni- and Co-substituted ZrB_2 (56.6 and 57.5 mV dec^{-1}, respectively) are smaller than the commercial RuO_2 (66.2 mV dec^{-1}). The findings uncovered that increasing the concentration of transition metal substitution from 0.05 to 0.2 in ZrB_2 promotes the activity accordingly while reaching its saturation limit.

All HfB_2-based samples showed high stability after 20 h of continuous operation. The HER overpotential of HfB_2 (620 mV) is much higher than the Pt/C (198 mV). However, with the substitution of transition metals, $Hf_{0.8}Co_{0.2}B_2$ and $Hf_{0.8}Ni_{0.2}B_2$ showed the overpotentials of 430 and 530 mV at 10 mA cm^{-2} current density, respectively. As expected, the Tafel slope of $Hf_{0.8}Co_{0.2}B_2$ is lower (105.4 mV dec^{-1}) than $Hf_{0.8}Ni_{0.2}B_2$ and HfB_2 (116.7 and 177.5 mV dec^{-1}, respectively), indicating facile HER kinetics compared with parent catalyst. The calculated C_{dl} value for $Hf_{0.8}Co_{0.2}B_2$ is 0.16 mF cm^{-2} which is higher than the calculated C_{dl} values for $Hf_{0.8}Ni_{0.2}B_2$ and HfB_2 (0.09 and 0.14 mF cm^{-2}, respectively), proving more available catalytic sites for HER process. In the case of OER activity of the samples, unsubstituted-HfB_2 reveals the potential of 1.72 V at current density of 10 mA cm^{-2} and overpotential of 490 mV. Based on the results, $Hf_{0.8}Ni_{0.2}B_2$ featured superior activity over all other samples with the overpotential of 320 mV close to RuO_2, only 30 mV higher than the value obtained for RuO_2 (overpotential of 290 mV) and smaller than its counterpart $Hf_{0.8}Co_{0.2}B_2$ (340 mV). The Tafel slope of $Hf_{0.8}Ni_{0.2}B_2$ and $Hf_{0.8}Co_{0.2}B_2$ samples (39.5 and 47.4 mV dec^{-1}, respectively) are lesser as compared to the commercial RuO_2 (66.2 mV dec^{-1}) indicating a faster current density increase with overpotential, therefore more facile electrode kinetics of substituted HfB_2 compared to the RuO_2. Similarly, increasing the substitution concentration from 0.1 to 0.2 enhances the activity of diboride while further increase in concentration to 0.3 diminishes the activity.

Further studies revealed that electron transfer between the transition metal and B has a positive impact on both charge conduction during water reduction and catalytic resistance, favoring Co-containing samples more than others. On the contrary, for the case of OER, the presence of Ni-containing species on the catalyst surface modulates the binding energy of oxygen intermediates, leading to enhanced OER activity.

Consequently, as being cost-effective alternative for noble metal electrocatalyst, transition metal diborides have proven their high activities for water splitting applications. A series of strategies can be implemented to further enhance the electrocatalytic performances of TMBs and as a result, their overall bifunctional activity can surpass the reference materials. Investigating the effect of other mentioned strategies on TMBs may open a new avenue for green energy applications.

BIBLIOGRAPHY

[1] M. Zeng and Y. Li, “Recent advances in heterogeneous electrocatalysts for the hydrogen evolution reaction,” *J. Mater. Chem. A*, vol. 3, no. 29, pp. 14942–14962, 2015.

[2] Z. Chen, X. Duan, W. Wei, S. Wang, Z. Zhang, and B. J. Ni, “Boride-based electrocatalysts: Emerging candidates for water splitting,” *Nano Res.*, vol. 13, no. 2, pp. 293–314, 2020.

[3] V. Mazánek, H. Nahdi, J. Luxa, Z. Sofer, and M. Pumera, “Electrochemistry of layered metal diborides,” *Nanoscale*, vol. 10, no. 24, pp. 11544–11552, 2018.

[4] Y. Jiang and Y. Lu, “Designing transition-metal-boride-based electrocatalysts for applications in electrochemical water splitting,” *Nanoscale*, vol. 12, no. 17, pp. 9327–9351, 2020.

[5] S. Zhang, R. Wang, and X. Li, “Recent advances in non-precious metal electrocatalysts for pH-universal hydrogen evolution reaction,” *Green Energy Environ.*, 2020.

[6] S. Gupta, M. K. Patel, A. Miotello, and N. Patel, “Metal Boride-Based Catalysts for Electrochemical Water-Splitting: A Review,” *Adv. Funct. Mater.*, vol. 30, no. 1, 2020.

[7] H. Y. Chung, M. B. Weinberger, J. M. Yang, S. H. Tolbert, and R. B. Kaner, “Correlation between hardness and elastic moduli of the ultraincompressible transition metal diborides RuB#!2, OsB2, and ReB2,” *Appl. Phys. Lett.*, vol. 92, no. 26, pp. 2006–2009, 2008.

[8] Q. Li, X. Zou, X. Ai, H. Chen, L. Sun, and X. Zou, “Revealing Activity Trends of Metal Diborides Toward pH-Universal Hydrogen Evolution Electrocatalysts with Pt-Like Activity,” *Adv. Energy Mater.*, vol. 9, no. 5, pp. 1–8, 2019.

[9] S. Gupta *et al.*, “Co-Ni-B nanocatalyst for efficient hydrogen evolution reaction in wide pH range,” *Appl. Catal. B Environ.*, vol. 192, pp. 126–133, 2016.

[10] S. Carenco, D. Portehault, N. Mezailles, and C. Sanchez, “Nanoscaled Metal Borides and Phosphides: Recent Developments and Perspectives,” *Chem. Rev. TA - TT -*, 2013.

[11] S. J. Sitler, K. S. Raja, and I. Charit, “ZrB2-HfB2 solid solutions as electrode materials for hydrogen reaction in acidic and basic solutions,” *Mater. Lett.*, vol.

188, pp. 239–243, 2017.

[12] Q. Hu *et al.*, “Nonmetal Doping as a Robust Route for Boosting the Hydrogen Evolution of Metal-Based Electrocatalysts,” *Chem. - A Eur. J.*, 2019.

[13] V. R. Stamenkovic, D. Strmcnik, P. P. Lopes, and N. M. Markovic, “Energy and fuels from electrochemical interfaces,” *Nat. Mater.*, vol. 16, no. 1, pp. 57–69, 2016.

[14] K. Zeng and D. Zhang, “Recent progress in alkaline water electrolysis for hydrogen production and applications,” *Prog. Energy Combust. Sci.*, vol. 36, no. 3, pp. 307–326, 2010.

[15] B. You and Y. Sun, “Innovative Strategies for Electrocatalytic Water Splitting,” *Acc. Chem. Res.*, vol. 51, no. 7, pp. 1571–1580, 2018.

[16] Q. Li, X. Zou, X. Ai, H. Chen, L. Sun, and X. Zou, “Revealing Activity Trends of Metal Diborides Toward pH-Universal Hydrogen Evolution Electrocatalysts with Pt-Like Activity,” *Adv. Energy Mater.*, vol. 9, no. 5, 2019.

[17] O. Schmidt, A. Gambhir, I. Staffell, A. Hawkes, J. Nelson, and S. Few, “Future cost and performance of water electrolysis: An expert elicitation study,” *Int. J. Hydrogen Energy*, vol. 42, no. 52, pp. 30470–30492, 2017.

[18] A. Manabe *et al.*, “Basic study of alkaline water electrolysis,” *Electrochim. Acta*, vol. 100, pp. 249–256, 2013.

[19] S. Anantharaj, S. R. Ede, K. Sakthikumar, K. Karthick, S. Mishra, and S. Kundu, “Recent Trends and Perspectives in Electrochemical Water Splitting with an Emphasis on Sulfide, Selenide, and Phosphide Catalysts of Fe, Co, and Ni: A Review,” *ACS Catal.*, vol. 6, no. 12, pp. 8069–8097, 2016.

[20] M. Tahir *et al.*, “Electrocatalytic oxygen evolution reaction for energy conversion and storage: A comprehensive review,” *Nano Energy*, vol. 37, no. February, pp. 136–157, 2017.

[21] W. J. Jiang *et al.*, “Crystallinity-Modulated Electrocatalytic Activity of a Nickel(II) Borate Thin Layer on Ni3B for Efficient Water Oxidation,” *Angew. Chemie - Int. Ed.*, vol. 56, no. 23, pp. 6572–6577, 2017.

[22] P. Los and A. Lasia, “Electrocatalytic properties of amorphous nickel boride electrodes for hydrogen evolution reaction in alkaline solution,” *J. Electroanal. Chem.*, vol. 333, no. 1–2, pp. 115–125, 1992.

[23] H. Vrubel and X. Hu, “Molybdenum boride and carbide catalyze hydrogen evolution in both acidic and basic solutions,” *Angew. Chemie - Int. Ed.*, vol. 51, no. 51, pp. 12703–12706, 2012.

[24] N. Du, C. Wang, X. Wang, Y. Lin, J. Jiang, and Y. Xiong, “Trimetallic TriStar Nanostructures: Tuning Electronic and Surface Structures for Enhanced Electrocatalytic Hydrogen Evolution,” *Adv. Mater.*, vol. 28, no. 10, pp. 2077–2084, 2016.

[25] X. Chen *et al.*, “Ultrathin nickel boride nanosheets anchored on functionalized carbon nanotubes as bifunctional electrocatalysts for overall water splitting,” *J. Mater. Chem. A*, vol. 7, no. 2, pp. 764–774, 2019.

[26] N. K. Chaudhari, H. Jin, B. Kim, and K. Lee, “Nanostructured materials on 3D nickel foam as electrocatalysts for water splitting,” *Nanoscale*, vol. 9, no. 34, pp. 12231–12247, 2017.

[27] D. Merki, S. Fierro, H. Vrubel, and X. Hu, “Amorphous molybdenum sulfide films as catalysts for electrochemical hydrogen production in water,” *Chem. Sci.*, vol. 2, no. 7, pp. 1262–1267, 2011.

[28] J. Masa *et al.*, “Ultrathin High Surface Area Nickel Boride (NixB) Nanosheets as Highly Efficient Electrocatalyst for Oxygen Evolution,” *Adv. Energy Mater.*, vol. 7, no. 17, pp. 1–8, 2017.

[29] Z. Wu, D. Nie, M. Song, T. Jiao, G. Fu, and X. Liu, “Facile synthesis of Co-Fe-B-P nanochains as an efficient bifunctional electrocatalyst for overall water-splitting,” *Nanoscale*, vol. 11, no. 15, pp. 7506–7512, 2019.

[30] F. Hu *et al.*, “Designing Highly Efficient and Long-Term Durable Electrocatalyst for Oxygen Evolution by Coupling B and P into Amorphous Porous NiFe-Based Material,” *Small*, vol. 15, no. 28, pp. 1–10, 2019.

[31] H. Sun *et al.*, “Superhydrophilic amorphous Co-B-P nanosheet electrocatalysts with Pt-like activity and durability for the hydrogen evolution reaction,” *J. Mater. Chem. A*, vol. 6, no. 44, pp. 22062–22069, 2018.

[32] G. X. Cao, N. Xu, Z. J. Chen, Q. Kang, H. Bin Dai, and P. Wang, “Cobalt-Tungsten-Boron as an Active Electrocatalyst for Water Electrolysis,” *ChemistrySelect*, vol. 2, no. 21, pp. 6187–6193, 2017.

[33] H. Li *et al.*, “Earth-Abundant Iron Diboride (FeB2) Nanoparticles as Highly Active Bifunctional Electrocatalysts for Overall Water Splitting,” *Adv. Energy Mater.*, vol. 7, no. 17, pp. 1–12, 2017.

[34] H. Park, A. Encinas, J. P. Scheifers, Y. Zhang, and B. P. T. Fokwa, “Boron-Dependency of Molybdenum Boride Electrocatalysts for the Hydrogen Evolution Reaction,” *Angew. Chemie - Int. Ed.*, vol. 56, no. 20, pp. 5575–5578, 2017.

[35] P. Zhang, M. Wang, Y. Yang, T. Yao, H. Han, and L. Sun, "Electroless plated Ni-Bx films as highly active electrocatalysts for hydrogen production from water over a wide pH range," *Nano Energy*, vol. 19, pp. 98–107, 2016.

[36] X. Ma *et al.*, "Crystal CoxB (x = 1-3) Synthesized by a Ball-Milling Method as High-Performance Electrocatalysts for the Oxygen Evolution Reaction," *ACS Sustain. Chem. Eng.*, vol. 5, no. 11, pp. 10266–10274, 2017.

[37] J. Li, H. Chen, Y. Liu, R. Gao, and X. Zou, "In situ structural evolution of a nickel boride catalyst: synergistic geometric and electronic optimization for the oxygen evolution reaction," *J. Mater. Chem. A*, vol. 7, no. 10, pp. 5288–5294, 2019.

[38] Y. Liang, X. Sun, A. M. Asiri, and Y. He, "Amorphous Ni-B alloy nanoparticle film on Ni foam: Rapid alternately dipping deposition for efficient overall water splitting," *Nanotechnology*, vol. 27, no. 12, p. 0, 2016.

[39] D. D. Le Pevelen, "X-ray crystallography of small molecules: Theory and workflow," *Encycl. Spectrosc. Spectrom.*, pp. 624–639, 2016.

[40] O. P. Choudhary and P. ka, "Scanning Electron Microscope: Advantages and Disadvantages in Imaging Components," *Int. J. Curr. Microbiol. Appl. Sci.*, vol. 6, no. 5, pp. 1877–1882, 2017.

[41] J. N. T. Nguyen and A. M. Harbison, "Scanning electron microscopy sample preparation and imaging," *Methods Mol. Biol.*, vol. 1606, pp. 71–84, 2017.

[42] S. Ebnesajjad, *Surface and Material Characterization Techniques*. 2014.

[43] T. Kerdcharoen and C. Wongchoosuk, *Carbon nanotube and metal oxide hybrid materials for gas sensing*. Woodhead Publishing Limited, 2013.

[44] S. Brunauer, P. H. Emmett, and E. Teller, "Adsorption of Gases in Multimolecular Layers," *J. Am. Chem. Soc.*, vol. 60, no. 2, pp. 309–319, 1938.

[45] W. G. Fahrenholtz, J. Binner, and J. Zou, "Synthesis of ultra-refractory transition metal diboride compounds," *J. Mater. Res.*, vol. 31, no. 18, pp. 2757–2772, 2016.

[46] L. Zoli, P. Galizia, L. Silvestroni, and D. Sciti, "Synthesis of group IV and V metal diboride nanocrystals via borothermal reduction with sodium borohydride," *J. Am. Ceram. Soc.*, vol. 101, no. 6, pp. 2627–2637, 2018.

[47] K. Bao, "Low Temperature Synthesis of Boron-Based Materials in Molten Salts," no. June, pp. 1–2, 2017.

[48] D. Liu, Q. Fu, and Y. Chu, "Molten salt synthesis, formation mechanism, and oxidation behavior of nanocrystalline HfB2 powders," *J. Adv. Ceram.*, vol. 9, no. 1, pp. 35–44, 2020.

[49] J. L. Innocent, D. Portehault, G. Gouget, S. Maruyama, I. Ohkubo, and T. Mori, "Thermoelectric properties of boron carbide/HfB2 composites," *Mater. Renew. Sustain. Energy*, vol. 6, no. 2, pp. 1–7, 2017.

[50] D. Portehault *et al.*, "A general solution route toward metal boride nanocrystals," *Angew. Chemie - Int. Ed.*, vol. 50, no. 14, pp. 3262–3265, 2011.

[51] S. E. Kravchenko *et al.*, "Synthesis of Zirconium Diboride Nanoparticles by the Reaction of ZrCl4 with NaBH4 in an Ionic Potassium Bromide Melt," *Russ. J. Gen. Chem.*, vol. 88, no. 8, pp. 1757–1758, Aug. 2018.

[52] M. Emamalizadeh, M. Mahdavi, and A. Shokrolahi, "Synthesis and characterization of ZrB2 nanopowders via metallothermic reduction of ZrCl4 using Na, Mg and Al in mild temperature: a morphology/reductant correlation," *J. Mater. Res. Technol.*, vol. 9, no. 4, pp. 7686–7700, 2020.

[53] L. Yuan, C. Wang, M. Bi, S. Ma, and X. Weng, "Effect of processing parameters on the formation process of nano-sized ZrB2 powders by the high energy ball milling," *Adv. Appl. Ceram.*, vol. 118, no. 7, pp. 395–402, 2019.

[54] A. L. Ortiz, V. Zamora, and F. Rodríguez-Rojas, "A study of the oxidation of ZrB 2 powders during high-energy ball-milling in air," *Ceram. Int.*, vol. 38, no. 4, pp. 2857–2863, 2012.

[55] A. Jena, T. R. Penki, N. Munichandraiah, and S. A. Shivashankar, "Flower-like porous cobalt(II) monoxide nanostructures as anode material for Li-ion batteries," *J. Electroanal. Chem.*, vol. 761, no. December 2018, pp. 21–27, 2016.

[56] X. Shen, M. Dai, M. Gao, B. Zhao, and W. Ding, "Solvent effects in the synthesis of CoB catalysts on hydrogen generation from hydrolysis of sodium borohydride," *Cuihua Xuebao/Chinese J. Catal.*, vol. 34, no. 5, pp. 979–985, 2013.

[57] A. Sivanantham, P. Ganesan, and S. Shanmugam, "Hierarchical NiCo2S4 Nanowire Arrays Supported on Ni Foam: An Efficient and Durable Bifunctional Electrocatalyst for Oxygen and Hydrogen Evolution Reactions," *Adv. Funct. Mater.*, vol. 26, no. 26, pp. 4661–4672, 2016.

[58] M. Cabán-Acevedo *et al.*, "Efficient hydrogen evolution catalysis using ternary pyrite-type cobalt phosphosulphide," *Nat. Mater.*, vol. 14, no. 12, pp. 1245–1251, 2015.

[59] Y. Ge, J. Wu, X. Xu, M. Ye, and J. Shen, "Facile synthesis of CoNi2S4 and CuCo2S4 with different morphologies as prominent catalysts for hydrogen evolution reaction," *Int. J. Hydrogen Energy*, vol. 41, no. 44, pp. 19847–19854,

2016.

[60] W. Liu *et al.*, “A highly active and stable hydrogen evolution catalyst based on pyrite-structured cobalt phosphosulfide,” *Nat. Commun.*, vol. 7, pp. 1–9, 2016.

[61] L. Li, Z. Deng, L. Yu, Z. Lin, W. Wang, and G. Yang, “Amorphous transitional metal borides as substitutes for Pt cocatalysts for photocatalytic water splitting,” *Nano Energy*, vol. 27, pp. 103–113, 2016.

[62] H. W. Nesbitt and D. Legrand, “Interpretation of Ni2p XPS spectra.pdf,” pp. 357–366, 2000.

[63] L. Lin, Q. Zhu, and A. W. Xu, “Noble-metal-free Fe-N/C catalyst for highly efficient oxygen reduction reaction under both alkaline and acidic conditions,” *J. Am. Chem. Soc.*, vol. 136, no. 31, pp. 11027–11033, 2014.

[64] L. Zhang, D. A. Pejaković, J. Marschall, and M. Gasch, “Thermal and electrical transport properties of spark plasma-sintered HfB2 and ZrB2 ceramics,” *J. Am. Ceram. Soc.*, vol. 94, no. 8, pp. 2562–2570, 2011.

[65] S. Q. Guo, T. Nishimura, Y. Kagawa, and J. M. Yang, “Spark plasma sintering of zirconium diborides,” *J. Am. Ceram. Soc.*, vol. 91, no. 9, pp. 2848–2855, 2008.

[66] J. Masa *et al.*, “Amorphous Cobalt Boride (Co 2 B) as a Highly Efficient Nonprecious Catalyst for Electrochemical Water Splitting: Oxygen and Hydrogen Evolution,” *Adv. Energy Mater.*, vol. 6, no. 6, pp. 1–10, 2016.

[67] P. R. Jothi, Y. Zhang, K. Yubuta, D. B. Culver, M. Conley, and B. P. T. Fokwa, “Abundant vanadium diboride with graphene-like boron layers for hydrogen evolution,” *ACS Appl. Energy Mater.*, vol. 2, no. 1, pp. 176–181, 2019.

[68] C. C. L. McCrory, S. Jung, I. M. Ferrer, S. M. Chatman, J. C. Peters, and T. F. Jaramillo, “Benchmarking Hydrogen Evolving Reaction and Oxygen Evolving Reaction Electrocatalysts for Solar Water Splitting Devices,” *J. Am. Chem. Soc.*, vol. 137, no. 13, pp. 4347–4357, 2015.

[69] R. Fernandes *et al.*, “Exploring the hydrogen evolution capabilities of earth-abundant ternary metal borides for neutral and alkaline water-splitting,” *Electrochim. Acta*, vol. 354, p. 136738, 2020.

[70] B. Mete, N. S. Peighambardoust, S. Aydin, E. Sadeghi, and U. Aydemir, “Metal-substituted zirconium diboride (Zr1-xTMxB2; TM = Ni, Co, and Fe) as low-cost and high-performance bifunctional electrocatalyst for water splitting,” *Electrochim. Acta*, vol. 389, p. 138789, 2021.

[71] H. Chen and X. Zou, “Intermetallic borides: Structures, synthesis and applications

in electrocatalysis," *Inorg. Chem. Front.*, vol. 7, no. 11, pp. 2248–2264, 2020.

[72] L. Wang *et al.*, "Surface-Activated Amorphous Iron Borides (Fe x B) as Efficient Electrocatalysts for Oxygen Evolution Reaction," *Adv. Mater. Interfaces*, vol. 6, no. 6, pp. 1–6, 2019.

[73] F. Guo *et al.*, "High-performance oxygen evolution electrocatalysis by boronized metal sheets with self-functionalized surfaces," *Energy Environ. Sci.*, vol. 12, no. 2, pp. 684–692, 2019.

[74] J. W. Lawson, C. W. Bauschlicher, and M. S. Daw, "Ab initio computations of electronic, mechanical, and thermal properties of ZrB2 and HfB2," *J. Am. Ceram. Soc.*, vol. 94, no. 10, pp. 3494–3499, 2011.

[75] X. Zou, L. Wang, X. Ai, H. Chen, and X. Zou, "Crystal phase-dependent electrocatalytic hydrogen evolution performance of ruthenium-boron intermetallics," *Chem. Commun.*, vol. 56, no. 20, pp. 3061–3064, 2020.

[76] S. Gupta, N. Patel, R. Fernandes, S. Hanchate, A. Miotello, and D. C. Kothari, "Co-Mo-B Nanoparticles as a non-precious and efficient Bifunctional Electrocatalyst for Hydrogen and Oxygen Evolution," *Electrochim. Acta*, vol. 232, pp. 64–71, 2017.

Appendix A:

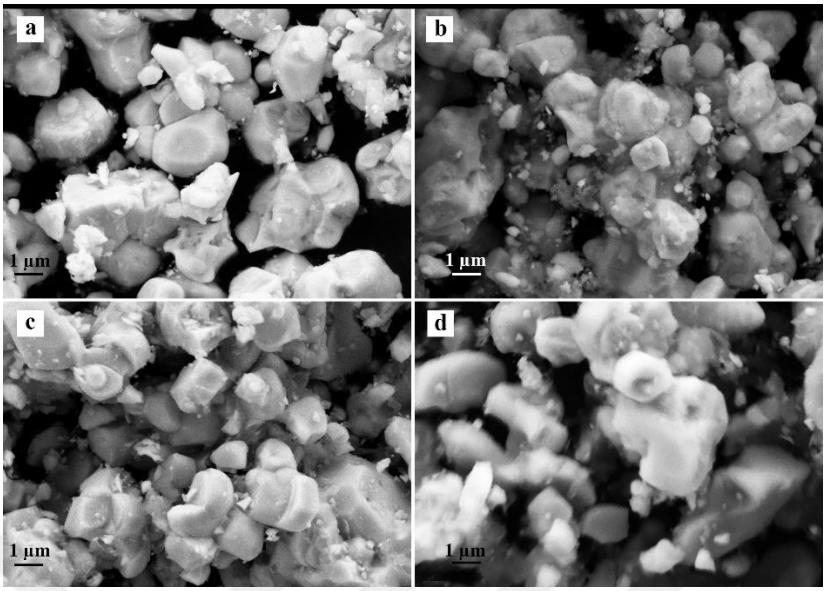

Figure A1: Low magnification SEM images of a) $Hf_{0.9}Ni_{0.1}B_2$ b) $Hf_{0.7}Ni_{0.3}B_2$ c) $Hf_{0.9}Co_{0.1}B_2$ and d) $Hf_{0.7}Co_{0.3}B_2$.

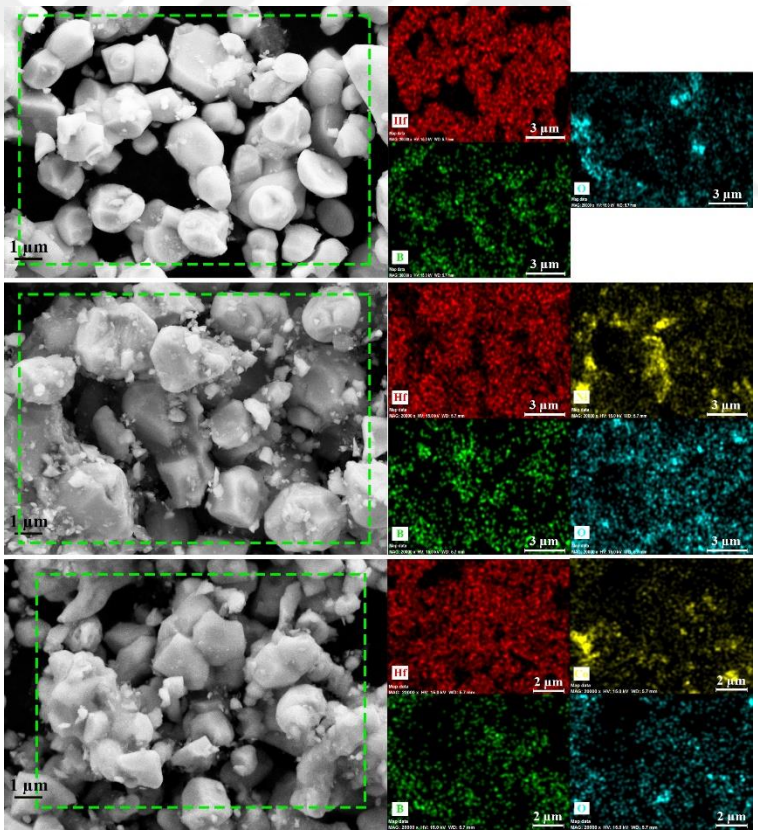

Figure A2: Low magnification SEM images of a) HfB_2 b) $Hf_{0.8}Ni_{0.2}B_2$ c) $Hf_{0.8}Co_{0.2}B_2$.